# CONVERSION OF POLYETHYLENE INTO HIGH VALUE CARBON NANOMATERIALS

FRASER NORRIS

Thesis submitted to the University of Strathclyde

for the degree of Doctor of Philosophy

Department of Chemical and Process Engineering

University of Strathclyde

2025

# Declaration of Authenticity and Author's Rights

‘This thesis is the result of the author’s original research. It has been composed by the author and has not been previously submitted for examination which has led to the award of a degree.’



Signed: FRASER NORRIS

Date: 07/10/2025

# Acknowledgments

The completion of this thesis would not have been possible without contributions from a number of people.

I would like to express gratitude to my supervisor, Dr Xiaolei Zhang for sharing her expertise and giving me invaluable guidance throughout.

The academic staff in the department for their advice and feedback. The Lab staff for making it possible to run my experiments, in particular Mara Knapp, Andy Monaghan and Jim Gallagher, who went above and beyond what was required of them to assit me.

I would like to thank all my fellow students, particularly Shuya Jia and Stuart Conroy, who were always available to talk through issues and assist in order to find a solution.

Shout out to all my friends, who provided some academic respite whenever it was required.

Madeline, thank you for your love and the moral support you provide me.

Finally, I am forever grateful to my parents and family for their love and belief in me. I wouldn’t have made it this far without them.

## Abstract

Plastic waste accumulation poses a major environmental challenge, with conventional recycling strategies insufficient to address its scale. Chemical upcycling of polyolefins into carbon nanomaterials (CNMs) offers a promising valorisation route, with one-stage direct pyrolysis offering a simplified reactor configuration. However, direct exposure of catalysts to complex plastic-derived intermediates under these conditions increases susceptibility to deactivation and uncontrolled carbon deposition. The performance and mechanistic behaviour of transition metal catalysts under these conditions remain insufficiently understood. This thesis aims to elucidate how catalyst composition and structure affect CNM growth in direct LDPE pyrolysis. Bimetallic and microporous aluminosilicates supported formulations were predicted to outperform conventional monometallic alumina-supported catalysts, due to enhanced nanoparticle stability, carbon-metal interactions, metal-support anchoring and precursor cracking.

Catalyst performance was evaluated by CNM conversion, morphology and graphitic quality, along with metal nanoparticle dispersion and support structure. Iron-based exhibited limited activity due to sintering and formation of deactivated phases. Cobalt displayed highest nanoparticle dispersion, forming both carbon nano-onions and carbon nanotubes, while Nickel catalysts displayed a higher selectivity for nanotubes. Contrary to initial expectations, bimetallic formulations did not consistently improve performance relative to monometallic systems. In contrast, secondary metal promoters were effective, with molybdenum optimal for conversion and manganese for graphitic quality.

Zeolites outperformed traditional alumina or clay supporting materials, with performance influenced by synergistic effects between metal and support. Ni stabilised the zeolite frameworks, preserving the open three-dimensional pore structures, and thus bulk precursor diffusion and metal nanoparticle dispersion. Whereas, Co induced controlled framework collapse, allowing active metal sites to be exsolved from the restrictive one-dimensional channels, producing small pore-templated accessible surface metal nanoparticles. These results show how catalyst behaviour in single-stage systems differs from multi-stage, and how catalyst performance is governed by metal-support interactions and structural evolution, providing mechanistically informed guidance for future catalyst design.

Table of Contents

# Table of Figures

# Chapter 1
# Introduction

Plastic waste presents a critical environmental and societal challenge, driven by the global dependence on fossil fuel-derived polymers. While plastics have become indispensable in modern life due to their versatility, durability and low cost, their resistance to degradation has led to widespread accumulation in natural habitats around the world. This contributes to vast environmental damage, significantly harming wildlife and entire ecosystems. Furthermore, the prevalence of microplastic pollution and the harmful chemical additives in plastic are causing a detrimental effect to human health. Currently, only a small fraction of plastic waste is recycled, with conventional recycling approaches hindered by limitations in feedstock sensitivity, product quality and process economic viability. Chemical upcycling offers a promising alternative, enabling the transformation of plastic waste into higher-value products. This section explores the current state of plastic waste management, assessing the suitability of different conversion routes to form products from waste plastic feedstocks.

## 1.1 The Current Plastic Waste Landscape

### *1.1.1 The Plastic Waste Problem*

Plastics are a large and diverse family of polymer materials traditionally derived from fossil fuel-based feedstocks. The numerous desirable properties of plastics including strength, flexibility, moldability, light weight and low production cost has led to the widespread adoption of plastic material. Indeed, the world produced approximately 450 million metric tonnes (MMT) of plastic in 2023, over 90% of which is fossil fuel derived [1] [2]. The productions and conversion of this plastic causes the release of a range of harmful pollutants including 1430 MMT $CO_2$, 150 MMT $CH_4$ and 13 MMT $N_2O$ in 2023 [3]. The ubiquity of plastics coupled with its slow degradation rate has resulted in around 300 MMT of plastic waste going to landfill in 2015 [4]. Mismanagement of these landfills, with 32 MMT estimated to be in coastal-mismanaged landfill sites, leads to approximately 8 MMT of plastic waste entering oceans each year, according to estimates in 2015 [4]. These key figures of the global plastic waste problem are summarised in Figure 1.1.

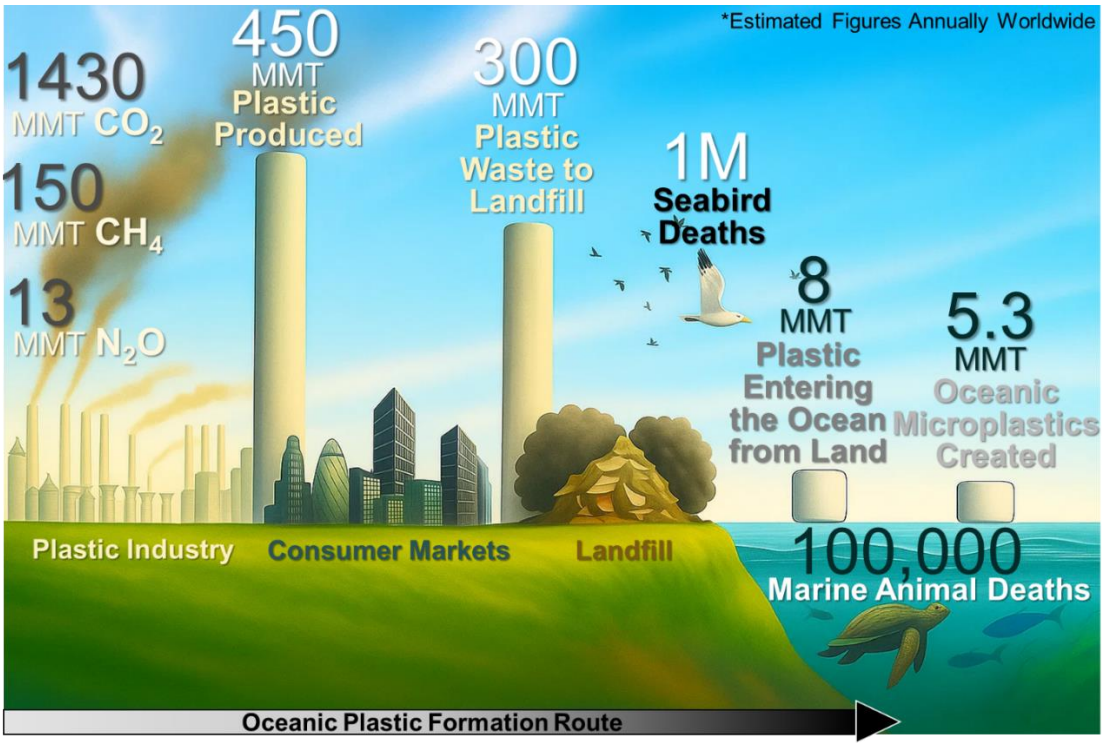


**Figure 1.1.** *Global plastic waste problem, with key annual figures from various recent years, adapted from Jambeck et. al. [4].*

These waste plastics are becoming increasingly widespread in both oceanic and freshwater environments. Over 700 species of marine animals, including seabirds,

fish and mammals, have been reported to ingest or become entangled in plastic debris, often with fatal consequences [5]. For instance, sea turtles and marine mammals can mistake plastic for food sources, causing 100,000 deaths annually [6] [7]. Similarly, seabirds are known to ingest large quantities of plastic, which accumulates in their stomachs, reducing their ability to consume real food and leading to the death of a million seabird annually [7] [8].

The non-biodegradable properties of plastics mean they remain in marine ecosystems and only break down into smaller particles known as microplastics, with around 5.3 MMT created annually [9]. These microplastics, defined as less than 5mm in diameter, are now ubiquitous in marine environments and have even been found in remote areas, such as in Arctic ice [10]. Microplastics can be ingested by marine organisms, causing them to enter and then accumulate up the food chain, eventually reaching humans through the consumption of seafood [11]. Additionally, microplastics are present in various freshwater and drinking water sources [11].

Microplastic have been linked to various health issues, including inflammation and disruption of endocrine functions [12]. Furthermore, microplastic particles can serve as carriers for persistent organic pollutants, which are highly toxic and can readily adsorb onto the microplastics. The bioaccumulation of these toxic chemicals in the human body can lead to long-term health consequences, such as immune system suppression, developmental disorders and a heightened susceptibility to chronic illnesses, including various forms of cancer [13].

Terrestrial ecosystems are also increasingly affected by plastic pollution. Harmful chemicals leach into the soil and groundwater, posing risks to wildlife and human populations. Additionally, the plastics itself can disrupt the natural processes of decomposition and soil structure, which can negatively impact plant growth and soil fertility [14]. This can reduce the availability of nutrients to crops and increase the risk of flooding by clogging drainage systems in agricultural fields [15]. Plastic production is a resource-intensive process that demands significant amounts of fossil fuels, particularly petroleum and natural gas. Indeed, plastic production is responsible for 6% of global oil consumption [16]. Plastic waste also has a substantial economic impact due to the cost of cleaning up plastic pollution, along with the economic losses in industries such as tourism and fisheries, with the annual economic damage of marine plastic estimated at $13 billion each year [17].

The issue of plastic waste is directly linked to multiple United Nations Sustainable Development Goals (SDGs), particularly SDG 3: Good Health and Well-being, SDG 12: Responsible Consumption and Production, SDG 13: Climate Action and SDG 14: Life Below Water, which are shown in Figure 1.2. This further demonstrates the scale and severity of the global plastic waste problem [18].


**Figure 1.2.** *The UNSG goals which are most closely linked to the issue of plastic waste [18].*

### *1.1.2 Plastic Waste Types and Streams*

There are seven main types of plastic categories, low-density polyethylene (LDPE), high-density polyethylene (HDPE), polypropylene (PP), polystyrene (PS), polyethylene terephthalate (PET), and polyvinyl chloride (PVC). A seventh category encompasses miscellaneous or other plastics which include polyurethane (PU) and bioplastics. These are shown in Figure 1.3, along with their molecular structure and contribution to waste streams.

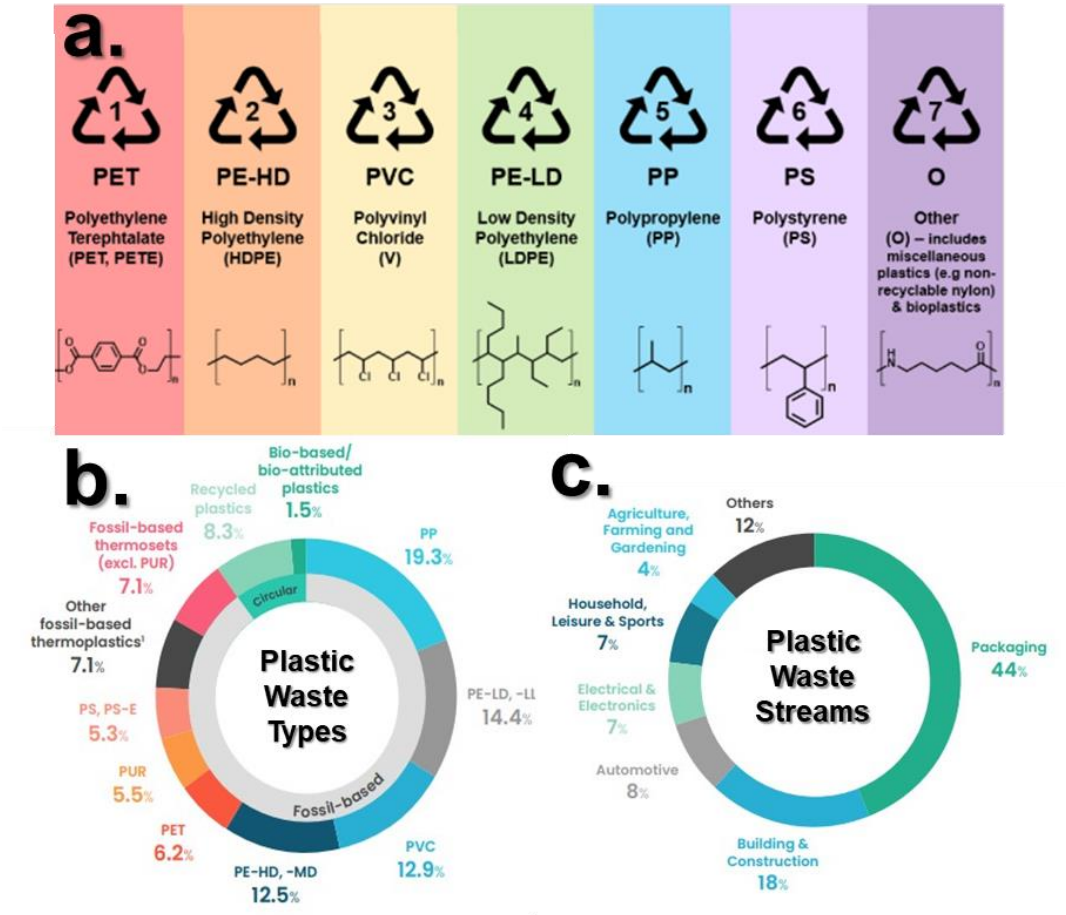


**Figure 1.3.** *The types of different plastics showing (a) the monomer chemical structure and the associated waste streams broken down by (b) plastic type and (c) plastic waste stream [2].*

Polyethylene (PE) has the simplest molecular structure among plastics, consisting of a straight chain of carbon atoms. This structure can have varying degrees of branching with neighbouring carbon chain. The molecular arrangement with HDPE has a more linear and tightly packed structure, whereas LDPE has a more branched and less densely packed structure [18]. This gives HDPE high strength and durability, making it suitable for products like containers, toys, and packaging that require protection from light exposure, such as milk bottles. Whereas, LDPE is more flexible making it suited for plastic bags, films, and squeezable containers. PP has a molecular structure similar to PE, but with a methyl group attached to every second carbon atom [18]. The rigidity and heat resistance of PP make it ideal for applications in the textile and automotive industries, including ropes, carpets, and car parts. PS consists of a carbon chain backbone with an aromatic group replacing the methyl group found in PP. This structure allows for the formation of numerous small air pocket

within the PS matrix, making it lightweight and ideal for protective packaging and insulation materials.

PET is composed of two monomers, ethylene glycol and terephthalic acid, therefore introduction oxygen groups to the polymer structure [19]. The resulting polymer chain has excellent tensile strength and clarity, making PET the preferred material for clear plastic bottles and other packaging applications. PVC has a structure where every second carbon atom in the backbone is bonded to a chlorine atom [20]. This gives PVC its high strength and excellent electrical insulating properties, making it suited for plumbing and electrical wire coverings. PU is a versatile polymer composed of alternating diisocyanate and polyol segments, forming either flexible or rigid structures depending on the specific monomers used [21]. It is widely applied across industries due to its robustness, abrasion resistance and flexibility. Bioplastics, derived from renewable biomass sources such as starch or polylactic acid (PLA), are designed to reduce the ecological footprint of plastic use, although their biodegradability varies depending on environmental conditions and formulation [22].

Plastic waste can be classified into several distinct streams based on its source and composition. The major waste streams include packaging waste, building and construction, automotive, electronical and household. Among these, packaging waste is the most significant contributor, accounting for approximately 44% of global plastic waste [2]. This category includes single-use plastics such as bottles, bags, and food containers, which are predominantly made from PET, HDPE and LDPE plastics. Construction and demolition waste accounts for roughly 18% of plastic waste, primarily consisting of PVC used in pipes, flooring and insulation, and PU, found in insulation foam and coatings [2]. Automotive and electronical plastic wastes each contribute 8% of the total plastic use, which is primarily pp [2]. Despite global efforts to manage plastic waste, only about 8% of all plastic is currently recycled, while 12% is incinerated and the remaining 80% accumulates in landfills or the natural environment [23]. Improving the technologies end of life management is vital to increase recycling and reuse, and ultimately reduce the harmful effects of plastic waste.

## 1.2 Plastic Valorisation Technologies

The approaches used to recycle and repurpose waste plastics can be broadly classified into four categories: primary mechanical, secondary mechanical, quaternary and chemical. Each approach has unique strengths and limitations, and

the suitability depends on the plastic type, contamination level and intended end use. These approaches with intermediates and outputs are shown in Figure 1.4.

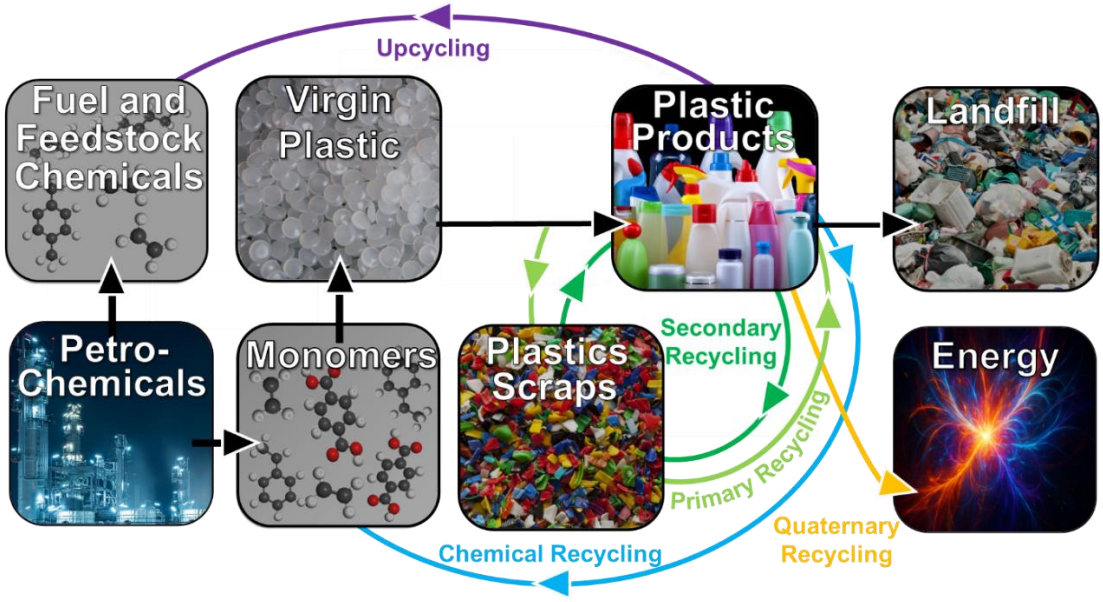


**Figure 1.4.** *Pathways for plastic recycling, showing how feedstock, intermediates and outputs.*

### *1.2.1 Primary Mechanical Recycling*

Primary mechanical recycling involves the reprocessing of waste plastic into a product of the same type, quality and specification. This is suited to recycling within a production line as waste scraps and offcuts as can be directly converted to the desired final product plastic. The straightforward nature of the process also makes it cost-effective and energy-efficient as it requires minimal processing compared to other recycling methods. Since the process deals with clean and homogeneous waste, the recycled plastic maintains a high standard, often comparable to virgin plastic. Although, primary mechanical recycling lacks feedstock adaptability, making it only an effective method in these specific situations, and unsuitable for the majority of post-consumer plastic or landfill waste [24]. Additionally, the material's properties degrade over multiple cycles, reducing the effectiveness, particularly in high-quality applications [24].

### *1.2.2 Secondary Recycling*

Secondary mechanical recycling takes a mixture of post-consumer plastics as the feedstock. After collection and transport to a recycling facility, the waste plastics are sorted into types, and can also be sorted into plastics with the similar additives and colourants. The separation process can either be performed manually or automatically making use of technologies such as near infrared or x-rays [25]. The

process results in lower-quality recycled plastic due to the degradation of mechanical properties during processing, particularly due to the presence of different additivities, other plastic types and contaminates [26]. Moreover, mechanical recycling is more energy and labour intensive than primary recycling, especially due to the need for extensive cleaning and sorting of the waste before processing [27]. To attempt to mitigate this, the recycled plastic is often mixed with virgin plastic, although this reduces the overall effectiveness of this method.

### *1.2.3 Quaternary Recycling*

Quaternary recycling, or incineration, is a commonly used method for disposing of plastic waste while recovering energy. Many plastics have a higher calorific value than coal, making them valuable for energy generation [28]. Modern incinerators can achieve high efficiency heat or electricity recovery, with advanced air pollution controls reducing emissions [29]. However, the release of greenhouse gases and other pollutants is inevitable, making quaternary recycling the option with the highest environmental impact [30].

### *1.2.4 Chemical Plastic Recycling*

Chemical recycling involves breaking down waste plastics for monomer recovery, enabling repolymerisation into new, virgin-quality plastics. This process is particularly suitable for polymers like PET and PLA, which contain cleavable functional groups and can be depolymerised using solvents [31] [32]. Unlike mechanical recycling, chemical recycling allows for the removal of additives and contaminants, resulting in higher-quality outputs. However, it comes with higher costs due to the need for complex infrastructure, chemical reagents and energy intensive processing [33]. Additionally, monomer recovery requires clean, homogeneous plastic streams and is unsuitable to certain plastic types such as polyolefins, which produces a complex mixture of hydrocarbons rather than discrete monomers upon decomposition [34], [35].

### *1.2.5 Chemical Upcycling*

Chemical upcycling aims to convert plastics into higher-value products rather than recycling them back into the original polymer [36]. This removes waste plastics from the lifecycle, while typically also replacing petrochemical feedstocks. Various technologies having been developed to achieve this, each with their own associated advantages and disadvantages. Hydrothermal liquefaction uses supercritical water to break down wet, mixed plastic streams but requires high-pressure equipment and

substantial capital investment [37]. Electrolysis methods using an electric current to decompose plastics can operate at ambient conditions, and product a range of higher value chemicals [38]. However, it is underdeveloped for practical implementation and less suited for non-polar feedstocks such as polyolefins [38]. Solvolysis decomposes plastic with the use of a solvent, although while applicable to certain plastics, often relies on solvents that are toxic or difficult to recover [39].

### *1.2.6 Pyrolysis*

Pyrolysis uses elevated temperature to thermally decomposes plastics in the absence of oxygen, offering a relatively simple, well-established and cost-effective plastic conversion method [40]. Although, the process requires an inert atmosphere adding to required inputs and the high temperatures required are energy intensive. Catalysts can address some of these issues by enhancing conversion efficiency and increasing product selectivity [41].

Generally, pyrolysis is suitable for a range of plastic feedstock, and also other materials including biomass and resins, indicating its versatility. However, some polymers remain unsuitable for upcycling, PVC with a chlorine content of around 57%, releases toxic hydrogen chloride gas during thermal decomposition [20]. This not only causes equipment corrosion and catalyst deactivation but also presents environmental risks [42] [36]. Pyrolysis of PET is also less desirable as its thermal decomposition yields a high proportion of benzoic acid, which can contaminate the other products and corrode processing equipment [43]. However, PET remains well suited for monomer recovery, and PVC suited to mechanical recycling [31]. This highlights the need for a multifaceted technological approach to manage plastic waste effectively, with the optimal technology option influenced by the feedstock and desired target products.

Pyrolysis is particularly effective for plastics that are not compatible with monomer recovery, especially polyolefins (HDPE, LDPE and PP). This makes pyrolysis especially promising due to the abundance of polyolefins, with them contributing around half of all plastic waste [2]. Additionally, the range of high value products which can be achieved from the pyrolysis of polyolefins shows significant promise, which is fully covered in the next section.

## 1.3 Products from Polyolefin Pyrolysis

The pyrolysis of polyolefins yields a diverse range of products, including liquid fuels, waxes, gases, hydrogen, and solid carbon char [44], which are shown in Figure 1.5.

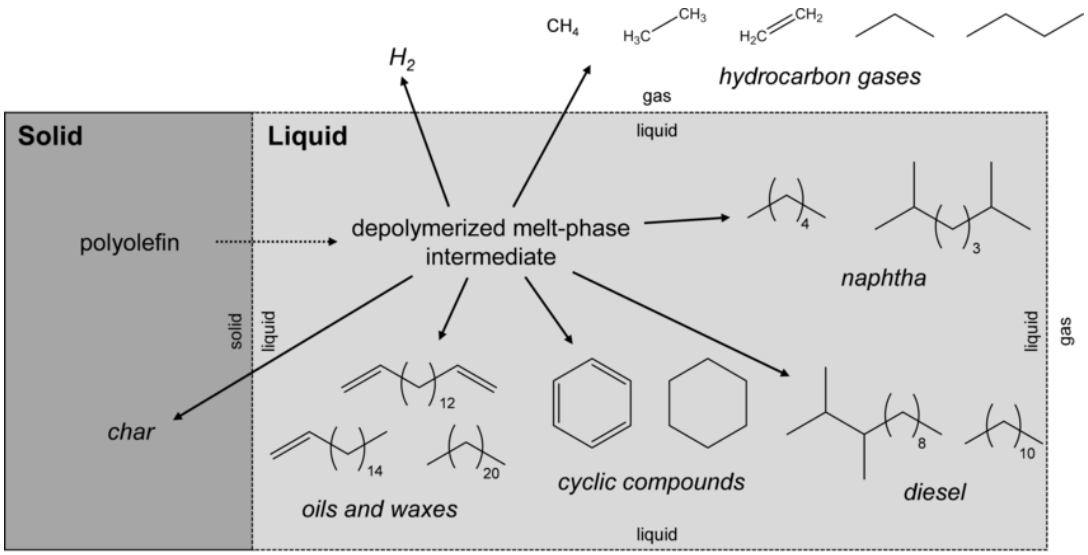


**Figure 1.5.** *The range of traditional products derived from polyolefin pyrolysis [44].*

### *1.3.1 Oil and Waxes*

Polyolefin pyrolysis oils are complex mixtures of alkanes, alkenes, and aromatics. Oils derived from polyolefins typically have low sulphur content than fossil fuel derived oil, thereby reducing pollutant emissions during combustion. These can be directly used as fuels, blended with diesel, or refined into gasoline, kerosene, and other petrochemical products [45]. Aromatic-rich pyrolysis oils particularly those high in BTX compounds (benzene, toluene, xylene) are valued in industrial applications such as resins, solvents, and pharmaceutical intermediates [46]. Long-chain paraffin components of the polyolefin pyrolysis product form waxes which have applications such as lubricant and mould release agent. After further refining, these can be used in cosmetics and paraffin-based products like candles and polishes [47]. Although, the cost of polyolefin derived hydrocarbon products is typically higher than the more established petrochemical alternatives.

### *1.3.2 Gaseous Phase Products*

The hydrocarbon gas phase are typically light alkanes and alkenes. These gases are often reused within the process to provide thermal energy, improving energy efficiency. Externally, they have value in industrial heating, electricity generation and chemical synthesis of compound such as methanol or ammonia [48]. The market value for hydrocarbon products is typically moderate an around $0.5-$1.50.

Additionally, these are mature markets highly linked to established petrochemical supply chains, therefore adding further difficulties in switching to plastic derived options.

Hydrogen gas a serve as input for fuel cells and industrial processes like ammonia production and oil refining. Similarly, to gaseous hydrocarbon products, hydrogen can be used directly as a combustion product to provide energy for the recycling process, with water as the only by-product.

### *1.3.3 Carbonaceous Products*

Solid carbon is the primary solid by-product of plastic pyrolysis, which is typically in the form of amorphous char. Char often contains impurities and can cause operational issues such as catalyst fouling, coking, and reactor blockages, making it a generally undesirable output with limited applications, such as filler material or low-grade fuel.

Amorphous carbon can exhibit forms, such as activated carbon or carbon aerogels, which offer higher value due to their high surface area and regular porosity, making them effective in applications such as filtration, adsorption and energy storage. Although, synthesising these from polyolefins is generally unfavourable due to difficulties in achieving a well-defined porous bulk structure. In contrast, the intrinsic lignocellulosic structure of biomass ideal for activated carbon (AC) synthesis, and organic templating molecules generally required for carbon aerogels.

A high value target product which is well suited to a plastic feedstock is carbon nanomaterials (CNMs), which have a range of high-value and advanced application spanning electronics, energy storage, aerospace and biomedical fields. Their market value is significantly higher than other polyolefin pyrolysis products, commonly reaching over $1,000 per kg**,** and with higher values possible depending on structure and purity [49].

Therefore, CNMs present the most valuable and promising target products for polyolefin valorisation. The simple hydrocarbon structure of polyolefins, allows for a theoretical system to separate plastic into solely carbon material and hydrogen, producing both a clean energy and a valuable material resource. CNM can take many different forms, with each type displaying a range of unique properties and thus a range of different potential applications. Filamentous and spherical CNMs are generally the most promising for direct plastic conversion, which is fully reviewed and justified in Chapter 2, and thus these are considered target products.

## 1.4 Catalyst and Process Set Up Selection

### *1.4.1 Catalyst Selection*

Catalysts targeting filamentous or spherical CNMs typically employ metal nanoparticles dispersed on solid supports, which facilitate hydrocarbon decomposition and carbon diffusion [102]. While a wide range of metals have been investigated for CCVD applications, their effectiveness varies significantly depending on physicochemical properties such as carbon solubility and thermal stability, as well as factors like cost and availability. Noble metals such as platinum and palladium offer high thermal stability and catalytic activity towards hydrocarbon decomposition, however their low carbon solubility inhibits carbon saturation and precipitation, leading to irregular CNM structures and low overall conversions. Furthermore, the high cost and scarcity of these metals make them unsuitable for scalable CNM production, especially when paired with low-cost plastic waste as the carbon source [103] [104].

In contrast, Fe, Co and Ni are consistently reported as highly effective catalysts for CVD-based CNM growth. These first-row transition metals offer a balanced combination of catalytic activity for precursor decomposition, moderate to high carbon solubility, and sufficient carbon diffusion rates, all of which are essential for supporting filamentous CNM growth mechanisms [105]. Their catalytic performance has been validated across a broad range of feedstocks, and are particularly effective for hydrocarbon precursors, making them suited for the pyrolysis products of polyolefins [106][107][108]. In addition to performance, Fe, Ni, and Co are relatively abundant, cost-effective and reasonably environmentally manageable, enhancing their feasibility for industrial-scale deployment. Therefore, Fe, Ni, and Co are the metals investigated further in this thesis. The comparative differences between these metals, including alloyed systems and support interactions, are further discussed in the literature review section.

### *1.4.2 One and Two Stage Comparation*

CCVD and pyrolysis can be effectively integrated using either a one-stage or two-stage process, each offering distinct operational advantages. In a two-stage configuration, pyrolysis and catalytic conversion occur in separate reactors. The pyrolysis reactor first thermally degrades plastics into hydrocarbon gases, which are then transferred to a second reactor containing the metal catalyst. This delivers a partially decomposed hydrocarbon mixture as the precursor, with a reduction in impurities, some of which can remain in the first stage as solids or can be filtered out

during intermediate steps [109]. Additionally, this separation allows for independent temperature control, ensuring that the optimal conditions for CNM growth can be established before the introduction of the carbon feedstock [109]. Whereas, the one-stage process involves loading both the plastic and the catalyst into a single reactor. As temperature increases, pyrolysis occurs in situ, generating volatile hydrocarbons that immediately interact with the catalyst, although often at suboptimal temperatures for high-quality CNM formation [109]. In both cases, the used catalyst is cooled and removed in order to separate out the CNM product, and thus CNM product typical occurs in a batch or semi-batch mode [109].

One-stage systems typically have lower capital costs and require less complex infrastructure, making them particularly suitable for mid-sized and pilot-scale applications [110]. Moreover, retrofitting existing incineration plants to operate as pyrolysis units is more feasible with one-stage systems, due to similarities in reactor design, thermal ramping behaviour, gas flow paths and containment systems [110]. Therefore, a there is a reduction in the complexity and capital expenditure required to adapt current incineration infrastructure. While one-stage systems offer practical benefits in terms of simplicity and cost, they also come with performance trade-offs. They are generally more susceptible to catalyst deactivation due to the presence of contaminants and elevated carbon fluxes at lower temperatures, which can lead to catalyst oversaturation and reduced conversions [109] [111]. Product quality is also affected, as these systems provide less control over the carbon deposition process, often resulting in CNMs with lower structural uniformity. However, some efficiency gains can be achieved through synergistic interactions between the catalyst and pyrolysis-active support materials, which aid in precursor breakdown and regulate the carbon supply rate to active catalytic sites [112] [113]. Overall, while two-stage systems require greater investment and operational complexity, they offer improved conversion efficiency and higher-value CNM products, making them advantageous for large-scale and high-purity applications. Whereas, one-stage offers a more basic but reliable design, making it suited to less expensive small to medium sized operations. The differences between one and two stage experimental set-ups are summarised in Figure 1.6.

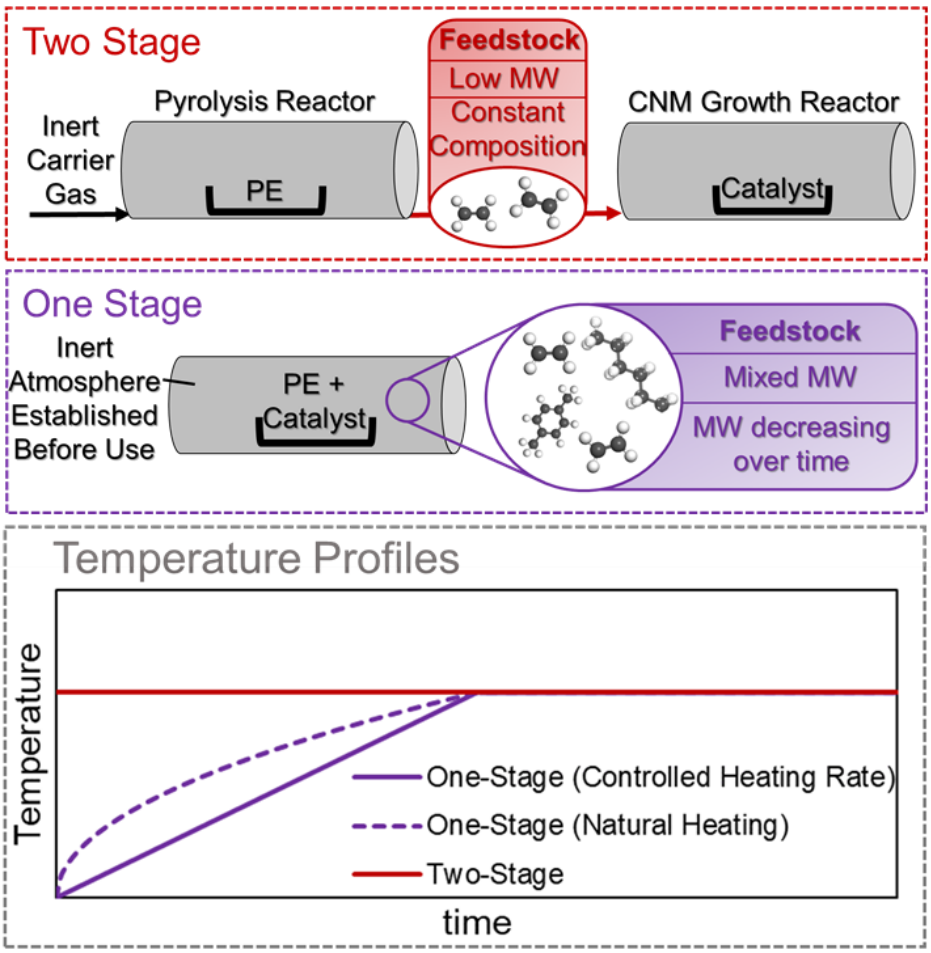


**Figure 1.6.** *Comparation between one-stage and two-stage experimental set-ups, feedstock composition and temperature profile.*

## 1.5 Research Question and Project Aims

Conventional approaches for the catalytic conversion of plastic waste into CNMs typically involve a two-stage process. This method is often complex and cost-intensive, requiring separate reactors for pyrolysis and carbon material growth, each with its own catalyst. Instead, this work aims to develop a single multifunctional catalyst capable of simultaneously facilitating pyrolysis and CNM synthesis within a one-stage process. This process offers a key advantage of simplified implementation and reduced capital and operation cost, making small-scale or decentralised plant implementation more feasible. Proven pyrolysis catalysts are integrated as the supporting material to support the dual-functionality required in this process. Furthermore, effective metal-support combination has the potential to lead to advantageous synergistic effects.

However, this process configuration does impose significant demands, requiring catalyst with higher carbon flux tolerance, improved resistance to deactivation and

effectiveness over a wider range if operating conditions. Importantly, the roles of different metal species under these intensified conditions are not fully understood. In a one-stage system, the demanding environment may affect catalyst performance differently compared to traditional two-stage setups, altering the relative performances of different metal species. Furthermore, the overall performance of a catalyst is highly influenced by the metal-support interaction, therefore the introducing non-traditional support materials may also shift the relative performances compared to more conventional systems. These metal-support interactions are further influenced during the dispersion of the metal onto the support, making the preparation method used to achieve this another important factor in determining catalyst structure and therefore performance.

A deeper understanding of these mechanisms involved is also required to better explain observed experimental outcomes and to identify the catalytic features that drive high performance. These insights will inform the design of future catalysts tailored specifically for efficient one-stage CNM production from plastic waste.

Objectives:

1. Evaluate the role of different metal catalysts for CNMs conversion, and investigate the underlying mechanistic reasons for the performance differences.
2. Evaluate the role of different catalyst support, and explore how the metal-support interactions and catalyst support morphology influence performance.
3. Investigate the effect of preparation methods and conditions on the performance of one-stage catalysts.

It is predicted that the performance of single-stage plastic pyrolysis systems for CNM synthesis can be significantly improved through holistic catalyst design. It is expected that bimetallic catalysts and secondary promoter metals can enhance catalytic performance under one-stage pyrolysis conditions by improving nanoparticle stability and modifying metal-carbon interactions. These effects are expected to reduce catalyst sintering, optimise carbon solubility and diffusion behaviour, and promote sustained CNM growth with improved graphitic quality. In addition, it is hypothesised that microporous aluminosilicate supports, such as zeolites and clays, will improve CNM formation compared to conventional alumina supports. The confined pore architecture is expected to regulate metal nanoparticle size distribution, strengthen metal-support interactions, and facilitate in situ cracking of polymer-derived

intermediates. This may enable controlled delivery of lower molecular weight carbon precursors to the active metal sites, improving conversion efficiency, CNM quality, and growth selectivity.

## 1.6 Thesis Outline and Novelty

This thesis explores the catalytic conversion of polyolefins into CNMs, focusing on the interaction between transition metal nanoparticles and hydrocarbon intermediates derived from plastic feedstocks. The literature review outlines the mechanistic steps involved in CNM formation and evaluates how catalyst formulation, primarily metal species and support materials, influences performance. The affect and role of different catalyst formulation in a one stage process are tested, with the resulting product evaluated in terms of carbon conversion, quality and morphology. The role of metal species is investigated through a comparison of monometallic and bimetallic transition metal catalysts, examining the influence of properties such as carbon solubility and metal site dispersion. This is followed by an evaluation of different support materials to understand how support morphology and metal-support interactions affect catalytic behaviour. The final results chapter focuses on catalystic development of a high performing metal-support combination through adjustments in calcination temperature, synthesis method and secondary metal addition. The novelty of this work lies in the development and comparation of these catalyst formulations, specifically:

1. A comprehensive evaluation of mono- and bimetallic catalysts in a single-stage plastic pyrolysis system**,** investigating how variations in metal composition and catalyst structure influence CNM growth mechanisms and catalytic performance.
2. A comparation of the roles of secondary promoter metals, providing insights into their individual and relative effects on catalytic performance in plastic to CNM conversion.
3. A direct comparation of diverse aluminosilicate support morphologies, including microporous and layered, which will offer generalised insights into how support morphology governs CNM formation from plastics.
4. An investigation of catalyst preparation parameters, evaluating how synthesis conditions influence catalyst structure and performance in plastic-to-CNM conversion systems.

Overall, the results highlight how careful tuning of catalyst composition and preparation can significantly enhance the conversion of plastic waste into high-value CNMs.

# References


[1] V. S. and M. R. Hannah Ritchie, “Plastic Pollution,” *Our World in Data*.

[2] P. Europe, “Plastics – the Facts 2020. An analysis in European plastic production, demand and waste data,” *PlasticEurope*, 2020.

[3] Hannah Ritchie, “How much of global greenhouse gas emissions come from plastics?,” *Our World in Data*, 2023.

[4] J. R. Jambeck *et al.*, “Plastic waste inputs from land into the ocean,” *Science (1979).*, vol. 347, no. 6223, 2015, doi: 10.1126/science.1260352.

[5] S. C. Gall and R. C. Thompson, “The impact of debris on marine life,” *Mar. Pollut. Bull.*, vol. 92, no. 1–2, 2015, doi: 10.1016/j.marpolbul.2014.12.041.

[6] Q. Schuyler, B. D. Hardesty, C. Wilcox, and K. Townsend, “Global Analysis of Anthropogenic Debris Ingestion by Sea Turtles,” *Conservation Biology*, vol. 28, no. 1, 2014, doi: 10.1111/cobi.12126.

[7] C. J. Rhodes, “Solving the plastic problem: From cradle to grave, to reincarnation,” *Sci. Prog.*, vol. 102, no. 3, 2019, doi: 10.1177/0036850419867204.

[8] C. Wilcox, E. Van Sebille, B. D. Hardesty, and J. A. Estes, “Threat of plastic pollution to seabirds is global, pervasive, and increasing,” *Proc. Natl. Acad. Sci. U. S. A.*, vol. 112, no. 38, 2015, doi: 10.1073/pnas.1502108112.

[9] A. S. C. M. A. T. L. F. M. Saskia Manshoven, “Microplastic pollution from textile consumption in Europe,” *ETC/CE Report*, Feb. 2022.

[10] I. Peeken *et al.*, “Arctic sea ice is an important temporal sink and means of transport for microplastic,” *Nat. Commun.*, vol. 9, no. 1, 2018, doi: 10.1038/s41467-018-03825-5.

[11] A. A. Koelmans, N. H. Mohamed Nor, E. Hermsen, M. Kooi, S. M. Mintenig, and J. De France, “Microplastics in freshwaters and drinking water: Critical review and assessment of data quality,” 2019. doi: 10.1016/j.watres.2019.02.054.

[12] C. M. Rochman, E. Hoh, B. T. Hentschel, and S. Kaye, “Long-term field measurement of sorption of organic contaminants to five types of plastic pellets: Implications for plastic marine debris,” *Environ. Sci. Technol.*, vol. 47, no. 3, 2013, doi: 10.1021/es303700s.

[13] R. Lohmann, E. Jurado, M. E. Q. Pilson, and J. Dachs, “Oceanic deep water formation as a sink of persistent organic pollutants,” *Geophys. Res. Lett.*, vol. 33, no. 12, 2006, doi: 10.1029/2006GL025953.

[14] M. C. Rillig, “Microplastic in terrestrial ecosystems and the soil?,” 2012. doi: 10.1021/es302011r.

[15] A. A. De Souza MacHado *et al.*, “Impacts of Microplastics on the Soil Biophysical Environment,” *Environ. Sci. Technol.*, vol. 52, no. 17, 2018, doi: 10.1021/acs.est.8b02212.

[16] Ellen MacArthur Foundation, “The New Plastics Economy: Rethinking the Future of Plastics & Catalysing Action,” *Ellen MacArthur Foundation*, 2017, doi: 10.1103/Physrevb.74.035409.

[17] J. Raynaud, *Valuing Plastics: The Business Case for Measuring, Managing and Disclosing Plastic Use in the Consumer Goods Industry*. 2014.

[18] United Nations, “Transforming Our World: the 2030 Agenda for Sustainable Development United Nations United Nations Transforming Our World: the 2030 Agenda for Sustainable Development,” *United Nations*, 2015.

[19] H. Jones, J. McClements, D. Ray, C. S. Hindle, M. Kalloudis, and V. Koutsos, “Thermomechanical Properties of Virgin and Recycled Polypropylene—High-Density Polyethylene Blends,” *Polymers (Basel).*, vol. 15, no. 21, 2023, doi: 10.3390/polym15214200.

[20] N. Roungpaisan *et al.*, “Effect of Recycling PET Fabric and Bottle Grade on r-PET Fiber Structure,” *Polymers (Basel).*, vol. 15, no. 10, 2023, doi: 10.3390/polym15102330.

[21] J. Yu, L. Sun, C. Ma, Y. Qiao, and H. Yao, “Thermal degradation of PVC: A review,” *Waste Management*, vol. 48, pp. 300–314, 2016, doi: 10.1016/j.wasman.2015.11.041.

[22] P. Bhavsar, M. Bhave, and H. K. Webb, “Solving the plastic dilemma: the fungal and bacterial biodegradability of polyurethanes,” 2023. doi: 10.1007/s11274-023-03558-8.

[23] S. Sid, R. S. Mor, A. Kishore, and V. S. Sharanagat, “Bio-sourced polymers as alternatives to conventional food packaging materials: A review,” 2021. doi: 10.1016/j.tifs.2021.06.026.

[24] R. Geyer, J. R. Jambeck, and K. L. Law, “Production, use, and fate of all plastics ever made,” *Sci. Adv.*, vol. 3, no. 7, 2017, doi: 10.1126/sciadv.1700782.

[25] J. Hopewell, R. Dvorak, and E. Kosior, “Plastics recycling: Challenges and opportunities,” 2009. doi: 10.1098/rstb.2008.0311.

[26] I. Vollmer *et al.*, “Beyond Mechanical Recycling: Giving New Life to Plastic Waste,” 2020. doi: 10.1002/anie.201915651.

[27] Z. O. G. Schyns and M. P. Shaver, “Mechanical Recycling of Packaging Plastics: A Review,” 2021. doi: 10.1002/marc.202000415.

[28] S. M. Al-Salem, A. Antelava, A. Constantinou, G. Manos, and A. Dutta, “A review on thermal and catalytic pyrolysis of plastic solid waste (PSW),” *J. Environ. Manage.*, vol. 197, no. 1408, pp. 177–198, 2017, doi: 10.1016/j.jenvman.2017.03.084.

[29] J. J. Klemeš, Y. Van Fan, and P. Jiang, “Plastics: friends or foes? The circularity and plastic waste footprint,” *Energy Sources, Part A: Recovery, Utilization and Environmental Effects*, vol. 43, no. 13, 2021, doi: 10.1080/15567036.2020.1801906.

[30] T. F. Astrup, D. Tonini, R. Turconi, and A. Boldrin, “Life cycle assessment of thermal Waste-to-Energy technologies: Review and recommendations,” *Waste Management*, vol. 37, 2015, doi: 10.1016/j.wasman.2014.06.011.

[31] P. M. Lemieux, C. C. Lutes, and D. A. Santoianni, “Emissions of organic air toxics from open burning: A comprehensive review,” 2004. doi: 10.1016/j.pecs.2003.08.001.

[32] V. Sinha, M. R. Patel, and J. V. Patel, “Pet waste management by chemical recycling: A review,” 2010. doi: 10.1007/s10924-008-0106-7.

[33] T. Narancic and K. E. O’Connor, “Plastic waste as a global challenge: Are biodegradable plastics the answer to the plastic waste problem?,” 2019. doi: 10.1099/mic.0.000749.

[34] K. Ragaert, L. Delva, and K. Van Geem, “Mechanical and chemical recycling of solid plastic waste,” *Waste Management*, vol. 69, pp. 24–58, 2017, doi: 10.1016/j.wasman.2017.07.044.

[35] S. E. Levine and L. J. Broadbelt, “Detailed mechanistic modeling of high-density polyethylene pyrolysis: Low molecular weight product evolution,” *Polym. Degrad. Stab.*, vol. 94, no. 5, 2009, doi: 10.1016/j.polymdegradstab.2009.01.031.

[36] T. M. Kruse, H. W. Wong, and L. J. Broadbelt, “Mechanistic modeling of polymer pyrolysis: Polypropylene,” *Macromolecules*, vol. 36, no. 25, 2003, doi: 10.1021/ma030322y.

[37] G. Lopez, M. Artetxe, M. Amutio, J. Bilbao, and M. Olazar, “Thermochemical routes for the valorization of waste polyolefinic plastics to produce fuels and chemicals. A review,” 2017. doi: 10.1016/j.rser.2017.01.142.

[38] G. C. Laredo, J. Reza, and E. Meneses Ruiz, “Hydrothermal liquefaction processes for plastics recycling: A review,” *Cleaner Chemical Engineering*, vol. 5, 2023, doi: 10.1016/j.clce.2023.100094.

[39] R. Shi, K. S. Liu, F. Liu, X. Yang, C. C. Hou, and Y. Chen, “Electrocatalytic reforming of waste plastics into high value-added chemicals and hydrogen fuel,” *Chemical Communications*, vol. 57, no. 94, 2021, doi: 10.1039/d1cc05032j.

[40] S. S. Borkar *et al.*, “Enabling resource circularity through thermo-catalytic and solvent-based conversion of waste plastics,” 2022. doi: 10.1016/j.checat.2022.09.003.

[41] A. Lopez-Urionabarrenechea, I. De Marco, B. M. Caballero, M. F. Laresgoiti, and A. Adrados, “Catalytic stepwise pyrolysis of packaging plastic waste,” *J. Anal. Appl. Pyrolysis*, vol. 96, pp. 54–62, 2012, doi: 10.1016/j.jaap.2012.03.004.

[42] K. Akubo, M. A. Nahil, and P. T. Williams, “Aromatic fuel oils produced from the pyrolysis-catalysis of polyethylene plastic with metal-impregnated zeolite catalysts,” *Journal of the Energy Institute*, 2019, doi: 10.1016/j.joei.2017.10.009.

[43] K. Lewandowski and K. Skórczewska, “A Brief Review of Poly(Vinyl Chloride) (PVC) Recycling,” 2022. doi: 10.3390/polym14153035.

[44] H. Bockhorn *et al.*, “Pyrolysis of Waste Plastics into Fuels,” *Waste Management*, vol. 70, no. 2, 2016.

[45] A. Zolghadr *et al.*, “On the Method of Pulse-Heated Analysis of Solid Reactions (PHASR) for Polyolefin Pyrolysis,” *ChemSusChem*, vol. 14, no. 19, 2021, doi: 10.1002/cssc.202002667.

[46] M. del Remedio Hernández, Á. N. García, and A. Marcilla, “Catalytic flash pyrolysis of HDPE in a fluidized bed reactor for recovery of fuel-like hydrocarbons,” *J. Anal. Appl. Pyrolysis*, vol. 78, no. 2, 2007, doi: 10.1016/j.jaap.2006.03.009.

[47] S. H. Chang, “Plastic waste as pyrolysis feedstock for plastic oil production: A review,” 2023. doi: 10.1016/j.scitotenv.2023.162719.

[48] D. G. Kulas, A. Zolghadr, U. S. Chaudhari, and D. R. Shonnard, “Economic and environmental analysis of plastics pyrolysis after secondary sortation of mixed plastic waste,” *J. Clean. Prod.*, vol. 384, 2023, doi: 10.1016/j.jclepro.2022.135542.

[49] H. H. Shah *et al.*, “A review on gasification and pyrolysis of waste plastics,” 2023. doi: 10.3389/fchem.2022.960894.

[50] Y. Peng *et al.*, “A review on catalytic pyrolysis of plastic wastes to high-value products,” 2022. doi: 10.1016/j.enconman.2022.115243.

[51] A. C. Dupuis, “The catalyst in the CCVD of carbon nanotubes-a review,” 2005. doi: 10.1016/j.pmatsci.2005.04.003.

[52] K. M. Wyss *et al.*, “Upcycling of Waste Plastic into Hybrid Carbon Nanomaterials,” *Advanced Materials*, vol. 35, no. 16, 2023, doi: 10.1002/adma.202209621.

[53] J. C. Acomb, C. Wu, and P. T. Williams, “The use of different metal catalysts for the simultaneous production of carbon nanotubes and hydrogen from pyrolysis of plastic feedstocks,” *Appl. Catal. B*, vol. 180, 2016, doi: 10.1016/j.apcatb.2015.06.054.

[54] D. Yao, Y. Zhang, P. T. Williams, H. Yang, and H. Chen, “Co-production of hydrogen and carbon nanotubes from real-world waste plastics: Influence of catalyst composition and operational parameters,” *Appl. Catal. B*, vol. 221, 2018, doi: 10.1016/j.apcatb.2017.09.035.

[55] D. Yao, H. Li, Y. Dai, and C. H. Wang, “Impact of temperature on the activity of Fe-Ni catalysts for pyrolysis and decomposition processing of plastic waste,” *Chemical Engineering Journal*, vol. 408, 2021, doi: 10.1016/j.cej.2020.127268.

[56] P. T. Williams, “Hydrogen and Carbon Nanotubes from Pyrolysis-Catalysis of Waste Plastics: A Review,” 2021. doi: 10.1007/s12649-020-01054-w.

[57] A. N. Amenaghawon, C. L. Anyalewechi, C. O. Okieimen, and H. S. Kusuma, “Biomass pyrolysis technologies for value-added products: a state-of-the-art review,” 2021. doi: 10.1007/s10668-021-01276-5.

[58] A. Oloruntoba, Y. Zhang, and C. S. Hsu, “State-of-the-Art Review of Fluid Catalytic Cracking (FCC) Catalyst Regeneration Intensification Technologies,” *Energies (Basel).*, vol. 15, no. 6, 2022, doi: 10.3390/en15062061.

[59] J. Gong *et al.*, “Catalytic carbonization of polypropylene by the combined catalysis of activated carbon with Ni2O3 into carbon nanotubes and its mechanism,” *Appl. Catal. A Gen.*, vol. 449, pp. 112–120, 2012, doi: 10.1016/j.apcata.2012.09.028.

[60] X. Wen *et al.*, “Nanosized carbon black combined with Ni2O3 as ‘universal’ catalysts for synergistically catalyzing carbonization of polyolefin wastes to synthesize carbon nanotubes and application for supercapacitors,” *Environ. Sci. Technol.*, vol. 48, no. 7, pp. 4048–4055, 2014, doi: 10.1021/es404646e.

# Chapter 2
# Literature Review

The conversion of polyolefins into carbon nanomaterials (CNMs) is a complex, multi-step process governed by a series of interconnected chemical transformations. Central to this process is the interaction between hydrocarbon intermediates and the catalyst. The catalyst typically consists of transition metal nanoparticles (NPs) dispersed on a thermal stable support material. An effective metal-support formulation will efficiently decompose the hydrocarbon precursor to maximise carbon conversions, whist controlling the flux of carbon growth species to amorphous or defective carbon deposition and catalyst deactivation. This will enable the growth of well-structured CNMs, and ensure catalyst longevity. Therefore, in this section the review the mechanistic steps involved in CNM formation from plastic feedstocks, and evaluate how metal catalyst species, support materials and preparation methods collectively influence catalytic performance.

## 2.1 CNMs types: Morphology, Properties and Applications

The primary types of carbon materials include graphene, graphite, fullerenes, carbon nano-onions (CNOs), carbon nanotubes (CNTs), and carbon nanofibers (CNFs), with the structures of these shown in Figure 2.1.

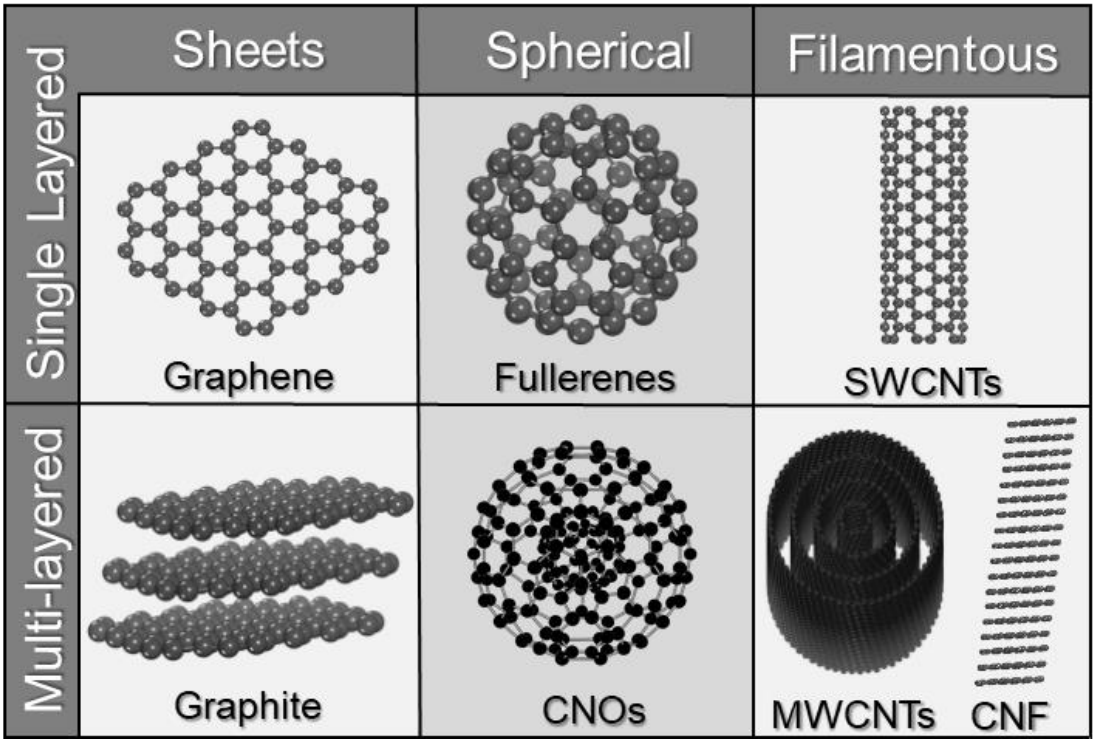


**Figure 2.1.** *The different molecular carbon arrangements for types of CNM, showing the role of geometric type and graphitic layering.*

### *2.1.1 Graphene*

Graphene consists of a single layer of $sp^2$ hybridised carbon atoms arranged in a two-dimensional hexagonal lattice, which is the basic building block for many other carbon allotropes [50]. Although, defects can form in this lattice, including Stone-Wales defects which consist of two pairs of pentagons and heptagons, and point vacancies which are due to a missing carbon atom in the graphitic lattice, which are illustrates in Figure 2.2.

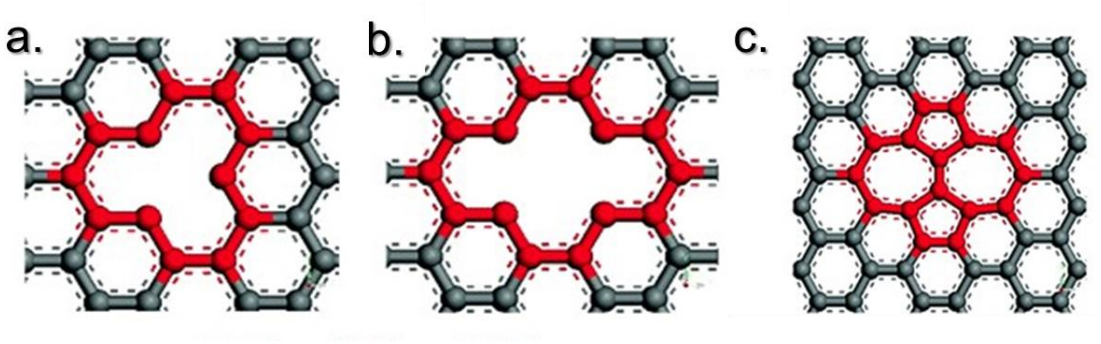


**Figure 2.2.** *Potential defects in hexagonal graphitic lattice (a) and (b) point vacancies and (c) Stone-Wales defect.*

The atomic thickness and delocalised π-electron system of graphene gives it properties including high electron mobility, thermal conductivity and exceptional mechanical strength [51]. Therefore, graphene is suited for ultra-fast transistors and other electronic devices [51] and high thermal conductivity promise in heat dissipation applications such as nano-heat sinks and thermal interface materials. The large surface area and excellent conductivity enhance the performance of batteries and supercapacitors, facilitating rapid charge/discharge cycles and improves energy density in lithium-ion and sodium-ion systems [52] [53]. The high flexibility, transparency and ability to retain electronic conductivity when under mechanical deformation make it suitable for next-generation flexible displays, touch panels, and wearable sensors [54] [50].

Multi-layered graphene, consisting of layers stacked on top of each other and held together only by Van der Waals forces is known as graphite. The individual graphene sheets easily slide across each other making bulk graphite soft and brittle. This also gives graphite properties of high conductivity along the graphene sheet axis, thermal stability, and solid state lubricate [55]**.** The quality of graphite plays a large role in determining the suitability to different application. Low-grade natural flake graphite is commonly used as an industrial lubricant and in metallurgical processes such as steelmaking [55]. High-purity vein or synthetic graphite has more advanced application, including as an anode material for batteries, as the regular layered structure of graphite allows $Li^+$ ions in lithium ion batteries to can intercalate between the graphene layers during charging [56]. Additionally, the crystalline structure of graphene makes it ideal for thermal protection systems in aerospace applications and radiation shielding in nuclear environments [57].

### 2.1.2 Fullerenes

Fullerenes are molecular allotropes of carbon in which carbon atoms are arranged in closed-cage structures [58]. The introduction of 12 pentagons into the hexagonal graphene lattice induces a curved morphology, forming the spherical or ellipsoidal shape of fullerenes. Since then various sizes have been discovered, from the smallest stable form of dodecahedral (C20), to larger structures with over 500 carbon atoms [59]. The unique morphology of fullerenes gives them high surface area and molecule entrapment abilities [60]. Additionally, the delocalised π-electron system and spherical geometry result in exceptional electron affinity and imparts curvature-induced reactivity [61].

Fullerenes have been widely studied for energy applications, serving as electron acceptors in photovoltaic cells, enabling the design of efficient solar cells [62]. Additionally, their structural rigidity and electron conductivity support usage in supercapacitors and as superconducting materials under certain conditions [63]. They have shown promise in biomedical research due to their ability to encapsulate small molecules and interact with biological membranes [64]. Functionalised fullerenes have been proposed as drug delivery vectors for cancer therapeutics and antioxidants [60]. However, their biodistribution, clearance mechanisms, and potential toxicity require careful consideration in clinical applications, making current applications limited.

### 2.1.3 CNOs

CNOs consist of concentrically layered fullerene shells encapsulating one another, with the curvature of the graphene layers contributing to quantum confinement effects and enhanced chemical reactivity. CNOs have attracted considerable attention in electrochemical energy storage due to their high electrical conductivity, accessible surface area and ability to accommodate rapid ion transport [65]. These features make them ideal candidates for supercapacitor electrodes and lithium-ion battery additives [65]. Functionalized CNOs have also demonstrated high electrocatalytic activity, particularly in applications such as oxygen reduction and hydrogen evolution reactions [66]. In biomedical contexts, CNOs have been explored as platforms for bioimaging and drug delivery, owing to their small size low toxicity and amenability to surface modification [67]. Their intrinsic fluorescence and ability to load therapeutic molecules or imaging agents enhance their utility in diagnostics and targeted therapy [68]. Additionally, CNOs show promise as catalysts or catalyst supports due to their

structural robustness and ability to anchor active sites across their curved surfaces [69].

### *2.1.4 CNFs*

CNFs are cylindrical nanostructures composed of graphene layers arranged in various configurations, typically with diameters ranging from tens to hundreds of nanometres. They exhibit good electrical conductivity, high tensile strength, and thermal stability [70]. CNFs are used in a variety of applications such as composite materials to enhance mechanical properties, in catalysis as support materials and in environmental applications for filtration and adsorption [71], [72]. The constituent graphene layers of a CNF can be organised in several distinct ways, namely platelet, ribbon and fishbone, with these morphologies shown in Figure 2.3 [73]. Each of these have differing chemical, physical and electrical properties and therefore suitability to certain application.

A platelet arrangement has graphene layers stacked perpendicular to the fibre axis. This exposes the edge planes of the graphene sheets on the CNF surface, which gives high surface area and enhanced reactivity, making them suitable for in catalyst support applications [74]. In a ribbon structure the graphene layers align parallel to the fibre axis and therefore have continuous graphene planes along the length of the CNF. This offers high electrical conductivity which makes ribbon CNFs suited to applications in energy storage devices like batteries and supercapacitors. Tubular CNFs have concentric cylindrical layers of graphene wrapped round a solid carbon centre. Fishbone CNFs consist of concentrically stacked graphitic cone structures along the fibre axis. This combines the characteristic of exposed graphene edges and graphene layers along the CNF associated with platelet and ribbon type, respectively [75]. Therefore, a balance between surface reactivity and electrical conductivity is provided, which enhances electrochemical reactions and are also used in sensors applications and composite materials to enhance mechanical properties [75] [76]..

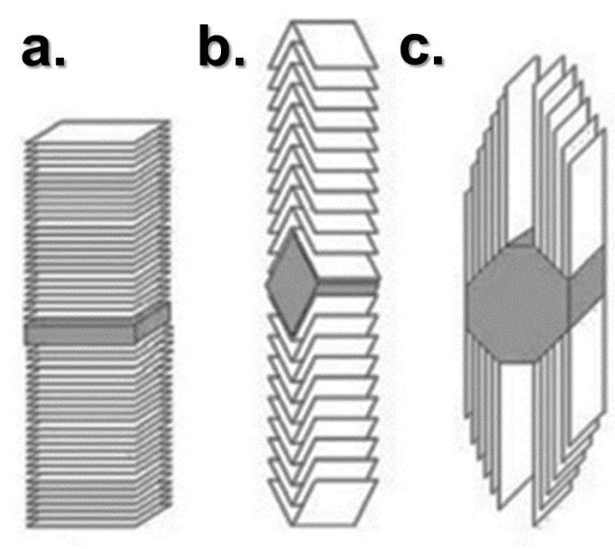


**Figure 2.3.** *Schematic of different types of CNF (a) platelet-type, (b) fishbone-type (c) ribbon-type [73].*

### *2.1.5 CNTs*

CNTs consist of a tube of carbon which is in hexagonal lattice form, which can be capped by hemi-spherical fullerene-like carbon, first synthesised in 1991 [77]. CNTs can either be single walled carbon nanotube (SWNTs) or have multiple concentric giving walls giving multi-walled carbon nanotubes (MWNTs). The diameter of SWNTs can range between 0.4 nm, the smallest currently synthesised, up to 7 nm for the largest [78] [79], with the MWNT diameter being determined by the number of layers each adding ~0.34 nm. The length of CNTs is usually in the order of 10nm-10um, although ultra-long CNTs can reach several centimetres.

CNTs have emerged as one of the most promising materials in the field of nanotechnology due to their remarkable properties, with SWNTs having an electrical conductivity which is 1000 times greater than copper [80] and MWNTs highest tensile strength of any discovered material [81]. SWNTs potential applications include advanced microelectronics [82], supercapacitors [83], semiconductors and biomedical applications such as drug delivery and gene therapy, giving SWNTs a higher value. MWNTs are often used as composite strength reinforcement for aerospace components, polymer materials and concrete [84], and can also be used as to improve conductivity in batteries [85], as an anticorrosive coating and in films for heat dissipation.

Individual CNT structure and overall bulk arrangement are important in determining the properties, and therefore suitability for potential application. The orientation of the

graphic lattice along the CNT has an associated chirality, which determines whether it is a conductor or semi-conductor [86]. Metallic SWNTs exhibit exceptional electron transport properties with ultra-low resistance, making them ideal for interconnects, nanowires, electrodes and field emitters [87]. Semiconducting SWNTs are suitable for transistors, sensors, and photodetectors [87]. Morphologies such as bamboo-like CNTs, characterised by periodic internal compartments, are well-suited for drug delivery, molecular encapsulation and catalytic supports [88]. Helical CNTs, twisted due to non-hexagonal ring incorporation, offer potential in nanoactuators and electromagnetic shielding applications due to their elasticity and complex dielectric properties [89], [90]. A diagram of these individual CNT morphologies is shown in Figure 2.4.

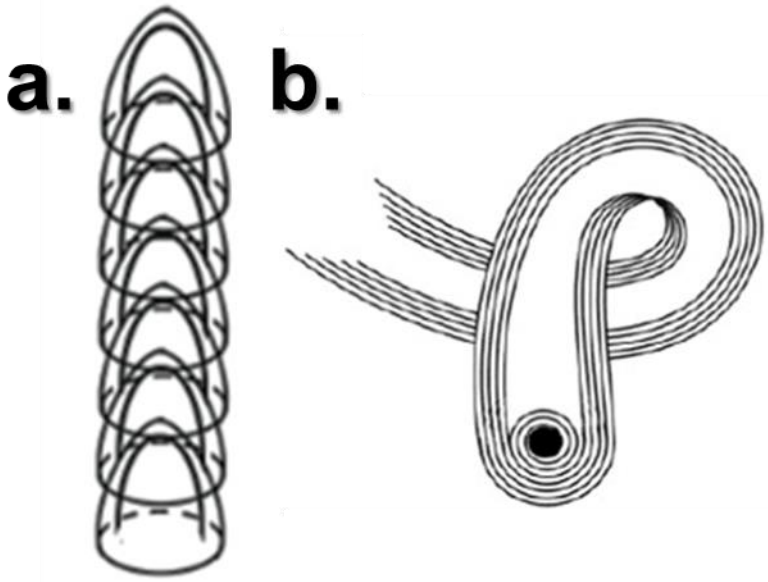


**Figure 2.4.** *Morphological variants of individual CNTs showing (a) Bamboo-like and (b) Helical [76], [91].*

The bulk structure of CNTs, which can be broadly be classified as aligned or tangled, also plays an important role in determining the suitability to certain applications. Aligned CNTs, often referred to as CNT forests, are oriented arrays where nanotubes grow in a uniform direction, enhancing directional electrical conductivity, thermal transport and mechanical strength [92]. Whereas, tangled CNTs form disordered mats or networks, typically resulting from random growth orientations. This entanglement creates a network with a larger void fraction and higher specific surface area, which is particularly advantageous for applications in adsorption, filtration, catalysis support and energy storage [93], [94].

## 2.2 CNM Growth Technologies

A range of technologies have been used to synthesis CNMs, each offering distinct product characteristics and conversion effectiveness. This section provides a comparative analysis of these methods, focusing on their applicability to polyolefin conversion.

### *2.2.1 Arc Discharge*

The arc discharge method is one of the earliest and most well-established techniques for synthesising CNMs, with CNTs discovered using this method in 1991 [77]. The process involves striking a high-current electrical arc between two graphite electrodes in an inert gas atmosphere, causing the sublimation of carbon atoms from the anode. The CNMs formed are usually high-quality with minimal defects, although arc discharge suffers from several drawbacks, particularly with the use of a polyolefin feedstock. Sustaining the arc and maintaining the high-temperature plasma requires substantial energy input, making it economically and environmentally costly on an industrial scale. It requires fairly extensive pre and post processing, especially with a plastic feedstock which need to be processed to form carbon material for the electrodes [95]. Additionally, arc discharge inherently causes the formation of soot and other unwanted biproducts, which would be further exacerbated when using polyolefins feedstock, require post-synthesis purification [96].

### *2.2.2 Laser Ablation*

Laser ablation involves the use of a high-energy laser to vaporise a carbon target, which cools to form CNMs, particularly CNTs and fullerenes, with buckminsterfullerene first discovered by this method in 1985 [58]. The high-energy density and short pulse duration of the laser enable rapid heating and quenching**,** which is ideal for forming uniform, well-ordered CNMs with precise control over particle size and morphology [96]. However, the technique is limited by its high energy consumption, leading to high operational and maintenance costs due to the use of high-powered pulsed lasers and vacuum or inert gas chambers. Therefore, scalability is limited**,** with laser ablation operating primarily in small quantity batch mode reactors, with high running costs and capital investment. Additionally, conversion efficiency is relatively low, especially when utilising polyolefin feedstock. Similar to arc discharge, laser ablation requires a solid carbon target, meaning that plastics must first be converted into a graphitic form before being used [97].

### 2.2.3 Exfoliation Methods

Exfoliation is a top-down approach of isolating atomically thin layers from bulk layered materials, particularly graphite, to produce graphene or graphene-like structures. Indeed, a simple scotch tape mechanical exfoliation by Novoselov and Geim was responsible for the discovery of graphene [50]. While mechanical exfoliation is suitable for fundamental research due to its ability to yield high-quality monolayer graphene, it is not scalable for bulk production, with electrochemical exfoliation methods developed to address this issue. Electrochemical exfoliation typically uses a carbon electrode immersed in an electrolyte, which upon applying a voltage, intercalation and gas evolution cause separation of graphene sheets. A major limitation of exfoliation-based approaches, as with arc discharge and laser ablation, is the need for high quality graphitic carbon. Although, unlike arc-discharge or laser ablation, exfoliation does not rearrange the atoms forming the carbon lattice, therefore a high-quality graphitic material is required as the feedstock. This is particular difficult to form from a polyolefin feedstock, as a large hydrocarbon molecules precursor cause crosslinking between graphitic layers.

### 2.2.4 Carbonisation of Structured Precursors

Carbonisation of structured precursors is a bottom-up synthesis approach where an organic template material is thermally decomposed in an inert atmosphere to produce CNMs that retain aspects of the precursor's original structure. A key advantage of this method is the direct transfer of structural features from the organic precursor to the final carbon product. This strategy allows for morphological control of the resulting carbon, enabling the design of tailored CNMs. Incorporating polyolefins as an additive to the precursor mixture can be a strategy to increase overall carbon yield, particularly for low-carbon-yielding polymers. However, this often comes at the expense of structural integrity. The inclusion of polyolefins can introduce defects, phase separation and impurities in the resulting carbon material, thereby reducing the structural uniformity and quality of the material.

### 2.2.5 Chemical Vapor Deposition (CVD)

Chemical Vapor Deposition (CVD) is among the most versatile and widely used techniques for synthesising CNMs, including CNTs, CNFs, graphene, and carbon spheres. The process involves the thermal decomposition of a hydrocarbon feedstock over a catalyst surface at elevated temperatures, typically between 600°C and 1000°C, which can then recombine to form organised carbon structures [98]. The

catalyst is typically a transition metal based and commonly supported on silica or alumina. When a plastic feedstock is used, it is typically initially decomposed to generate hydrocarbon gases, which serve as carbon sources for CCVD growth. CVD can produce high quality carbon products, with a process that is cost effective, has low energy consumption and is highly scalable. The conversion of plastic to carbon materials can be achieved directly, unlike alternative methods, simplifying and reducing the cost of the process. The combination of CVD with polyolefin pyrolysis is particularly effective as both requiring high temperatures and inert atmospheres, with pyrolysis converting plastic into CVD compatible hydrocarbon gases. Therefore, utilising CVD provides a scalable and efficient route for plastic conversion to valuable carbon materials. However, product purity and catalyst deactivation are issues, but which can be addressed with catalyst design and adjustment of conditions.

Overall, while laser ablation and arc discharge can produce high-quality nanomaterials, their limitations in scalability and cost make them less practical for large-scale production, with the additional drawback of pre-processing of polyolefin to carbon. Exfoliation shares this same problem but with a greater degree of sensitivity to the quality of this intermediate. The introduction of plastic to the carbonisation of structured precursor will likely reduce the structural specificity and quality of the product. Therefore, overall CVD shows the highest potential for large scale CNMs synthesis, and additionally can be effectively integrated with pyrolysis, making it ideal for polyolefin conversion.

## 2.3 CNMs Derived from Plastics

The integration of plastic pyrolysis with CVD for CNM synthesis offers an effective route for polyolefin conversion. Selecting the most appropriate CNM to target is a critical step in developing catalytic upcycling processes for waste plastics. The feasibility of producing different CNM types from plastic using pyrolysis and CVD varies widely. Catalyst type, support material, morphology and reaction conditions all play a crucial role in determining the structure, quality, and yield of the final product. Therefore, identifying suitable target CNMs is essential for guiding catalyst and system design.

### *2.3.1 Graphene*

Graphene can be produced by CVD, although typically a lower molecular weight hydrocarbon precursor is used. This is decomposed on a metallic foil catalyst, which produce single-layer graphene with high crystallinity effectively. However, when

plastic is used as a feedstock, it introduces a broader range of hydrocarbons, including long-chain alkanes, aromatics, and other high-carbon-density compounds. These contribute to multilayer graphene and amorphous carbon formation through catalyst carbon oversaturation [99]. Therefore, achieving high-purity, monolayer graphene from plastic feedstocks remains technically challenging and economically uncompetitive compared to conventional hydrocarbon sources. As a result, graphene production from plastic is currently less viable at scale than other carbon nanomaterials. Additionally, producing well-structured graphite directly from polyolefins is challenging, as it requires precise control over layer stacking and graphitisation. While high-temperature pyrolysis in the presence of catalysts can generate some graphitic carbon, the quality is often inconsistent and inferior to that produced from traditional precursors.

### *2.3.2 Fullerenes*

Specific CVD conditions and controlled thermal degradation of polyolefins have been explored to produce fullerenes, although this presents a particular challenge when using polyolefin feedstock. Fullerenes typically require well-defined precursor fragmentation to provide a uniform growth species, which is particularly difficult to achieve with the mixture of hydrocarbons produced during polyolefin decomposition. Additionally, fullerenes usually require rapid quenching rates to preserve molecular structure, which are difficult to implement in a pyrolysis or CVD process. This makes them well suited for arc-discharge methods, with the yield and purity of fullerenes synthesised by CVD from a plastic feedstock remaining low. Additionally, CVD produces complex carbon mixtures that require separation and purification [100].

### *2.3.3 CNOs*

CNOs show somewhat more potential for growth from a polyolefin feedstock. CNOs can be produced by CCVD on transition metal nanoparticles which serve as nucleation sites around which carbon deposits in multiple spherical layers. Pyrolysis of polyolefins provides higher molecular weight precursors which exhibit high carbon density, which can induce a high carbon flux at the catalyst surface. This causes conditions of moderate to high carbon supersaturation, which can result in the formation of CNOs. The formation of well-defined CNOs is enhanced by isotropic carbon deposition, in which carbon atoms arrive uniformly from all directions, which can be influences by reaction set-up and the nature of the catalyst itself. Therefore,

CNOs are a feasible target product in CVD-based upcycling strategies for waste plastics are the optimal selection for a polyolefin feedstock.

### *2.3.4 CNTs*

CNTs represent one of the most viable and extensively studied carbon nanomaterials that can be synthesised from plastic-derived feedstocks using CVD. Numerous studies have demonstrated that CNTs grown from polyolefin pyrolysis vapours can exhibit structural and functional properties comparable to those obtained from conventional hydrocarbon gases. Similar to CNOs, CNTs grown by CVD nucleate on the surface of transition metal nanoparticles. These nanoparticles facilitate the decomposition of hydrocarbon vapours and promote the precipitation of carbon into tubular graphitic layers. A key distinction, however, lies in the anisotropic nature of CNT growth, which is influenced by the catalyst support interactions. Rate of carbon supply and diffusion on the catalyst also play a key role in determining if CNT or CNO is formed. The ability of CVD to utilise low-cost plastic feedstocks, combined with the high performance and application diversity of CNTs makes them a highly attractive target product in waste plastic upcycling strategies [101].

## 2.4 CNM Stages of Growth and Mechanisms

The growth of CNMs from polyolefins typically proceeds through a multi-step process. Initially, the polyolefin undergoes pyrolysis, producing hydrocarbon intermediates and hydrogen. These can act as reduction agents, allowing the formation of active metal catalyst sites. These hydrocarbon precursors subsequently adsorb onto the surface of the reduced catalyst, where they decompose into active carbon species that facilitate CNM growth. The catalyst-support formulation and reaction conditions used will affect these conversion pathways, and therefore the quality and morphology of the CNM product. Therefore, the factors which effect catalytic performance will be clearer with a detailed understanding of the underlying mechanisms at each stage.

### *2.4.1 Pyrolysis of Polyolefin*

The initial stage, polyolefin pyrolysis, is primarily driven by β-scission reactions that break the polymer chains into lower molecular weight compounds. β-scission reactions are driven by carbon radicles formed by high temperature, or ions formed through catalytic activity [53]. These facilitate chain cleavage, which produces a chain end alkene and radicle/ion terminated chains, which is shown in Figure 2.5a. Hydrogen transfer reactions, including hydrogen shifts within a molecule and hydrogen abstraction between molecules, allow the propagation of the radicle/ion,

facilitating further cracking at various chain locations, and thus producing a range of chain lengths. Additionally, mid-chain radicles/ions facilitate recombination producing branched products and cyclisation reaction producing aromatics, which is shown in Figure 2.5b. The promotion of aromatic intermediates has been proposed as beneficial to the final CNM product, highlighting the importance of the decomposition stage [54] [55].

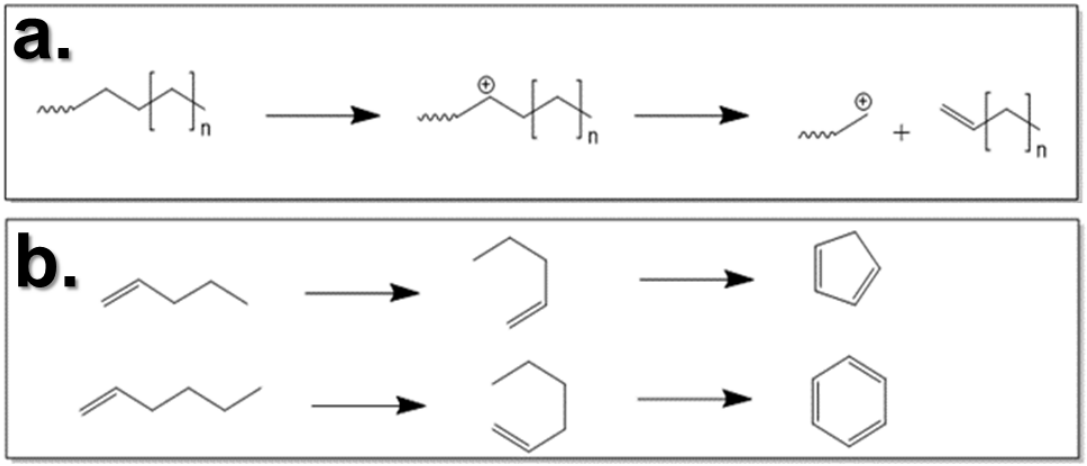


**Figure 2.5.** *A summary of the mechanisms involved in polyolefin pyrolysis, simplified for a carbon backbone showing (a) the β-scission reaction and (b) chain cyclisation reactions*

### *2.4.2 Catalyst Reduction*

Transition metal catalysts used for CNM growth are usually initially in an oxygen enriched form in the fresh catalyst, with reduction to the catalytically active metallic form. The mechanistic of the reduction influences not only the formation of active catalyst sites, but also their size and dispersion, key factors in determining catalytic performance. This reduction typically occurs in situ during the pyrolysis of the plastic, with the hydrogen gas and hydrocarbon radicals generated serving as reduction agents. Hydrogen has also been reported to stabilise metal NPs, allowing for controlled reduction that can maintain stable NPs. Whereas, the high reactivity of the hydrocarbon radicles can rapidly deoxygenate metal oxides, which can destabilise intermediate phases altering the formation pathway. These interactions between pyrolysis by-products and catalyst surfaces significantly shape the growth environment for CNT formation.

### *2.4.3 Adsorption*

Once the metallic catalyst is reduced, the adsorption of hydrocarbon intermediates onto its surface becomes the next critical step. Adsorption strength governs how effectively these precursors bind to the catalyst and undergo activation. Stronger

adsorption facilitates precursor decomposition and dehydrogenation, often enabling CNM growth at lower temperatures. Active sites such as catalyst edges, corners, and defect sites exhibit higher adsorption energies compared to flat facets, enhancing reactivity. The nature of the hydrocarbon species influences adsorption behaviour. Long-chain hydrocarbons, common in PE pyrolysis, tend to bind more strongly due to their higher van der Waals interactions. This can be beneficial in delivering sufficient carbon to the catalyst surface but may also result in uneven surface coverage and reduced mobility, which can impair CNT uniformity [56]. In contrast, smaller hydrocarbons, while offering weaker individual adsorption, can cover the catalyst more uniformly and diffuse more freely, leading to more consistent CNM growth. Moreover, the geometry of the catalyst will influence the adsorption strength, with metal cluster shown the enhanced adsorption due to corner and edge sites by ab initio molecular dynamics simulations [16] [18].

### *2.4.4 Decomposition*

Following adsorption, hydrocarbon precursors undergo catalytic decomposition to yield carbon growth species. This step is initiated primarily by dehydrogenation, in which the metal catalyst cleaves C-H bonds. For smaller, unsaturated hydrocarbons, decomposition typically involves relatively simple pathways, including sequential dehydrogenation and C-C bond cleavage. However, larger, saturated hydrocarbons such as those produced during PE pyrolysis present a more significant challenge. Their bulky and complex molecular structures can introduce side reactions and multi-step decomposition mechanisms. Moreover, their high carbon density increases the likelihood of catalyst oversaturation, which can lead to encapsulation by amorphous carbon or inert graphitic shells, both of which deactivate the catalyst preventing further carbon growth. The catalyst also facilitates the recombination of hydrogen atoms into $H_2$ gas which is essential for sustaining catalyst activity, as the removal of surface hydrogen prevents site passivation and allows continued hydrocarbon activation. This shows the importance of the decomposition efficiency and mechanism on the performance of a catalyst.

### *2.4.5 Graphitic Carbon Formation*

The formation of the CNM itself involves the assembly of carbon atoms into a graphitic lattice, which is governed by carbon dissolution, diffusion, and subsequent precipitation within the metal NP catalyst. Carbon solubility is central to this mechanism, as dissociated carbon atoms enter void spaces within the metal lattice

rather than forming covalent metal-carbon bonds as would occur in carbide formation. In metal solution, carbon atoms retain high mobility, enabling rapid diffusion through the NP, allowing for high uptake and transport of the carbon supply. Precipitation is driven by differences in carbon chemical potential between the dissolved state and the graphitic phase. Continued hydrocarbon decomposition increases the carbon flux to the particle surface, raising the dissolved carbon concentration and therefore its chemical potential. When the chemical potential of carbon in the metal exceeds that of graphitic carbon, the system becomes supersaturated and precipitation is thermodynamically favoured.

The carbon solubility of the catalyst metal strongly influences CNM growth behaviour. If solubility is too low, carbon accumulates rapidly at the surface and can form amorphous deposits that encapsulate the catalyst, terminating growth. Conversely, excessively high carbon solubility can delay supersaturation and promote carbide formation or structural instability in the nanoparticle, reducing catalytic activity. Effective CNM catalysts therefore require moderate carbon solubility to allow carbon dissolution while still enabling controlled precipitation of graphitic carbon.

### *2.4.6 Catalyst Phase Growth Modes*

The physical state of the catalyst during CNM growth can either be liquid or solid, giving two growth modes of VLS (vapour-liquid-solid) or VSS (vapour-solid-solid), with vapour referring to the precursor phase, and the third referring to the solid carbon product state. In VLS growth, the liquid phase of the NP allows rapid, isotropic diffusion of dissolved carbon and enables dynamic reshaping of the catalyst particle. This high atomic mobility facilitates the fast CNM growth rates and can support the formation of smooth, continuous carbon structures, since the metal lattice can easily be reshaped. However, liquid particles are also more prone to migration and coalescence, which can lead to catalyst sintering and therefore larger, less active NPs. Although the bulk melting temperatures of Fe, Ni, and Co are significantly higher than typical CNM synthesis temperatures, several nanoscale effects can reduce the effective melting temperature of catalyst particles. These include melting point depression in small nanoparticles, carbon dissolution within the metal lattice, and possible carbide formation. Under such conditions, the catalyst may behave as a liquid or quasi-liquid phase, enabling VLS-type growth. In VSS growth, the catalyst nanoparticle remains crystalline and solid. Carbon dissolves interstitially within the solid lattice and diffuses through bulk, grain boundaries, or along the surface before

precipitating as graphitic carbon. Diffusion is slower and more anisotropic than in a liquid, and nucleation preferentially occurs at high-energy sites such as edges, facets, or the metal-support interface. This can lead to stronger structural relationships between the metal crystal planes and the growing CNT, influencing diameter control and potentially chirality selection.

### *2.4.7 Tip and Base Growth Modes*

CNTs can grow by two distinct growth modes, either tip or base growth, defined by the relative position of the catalyst to the growing CNT. In tip growth, the metal NP detaches from the substrate, and carbon is incorporated at the exposed tip of the catalyst as the CNT elongates away from the support. In base growth, the catalyst remains anchored to the support, and carbon incorporation at the catalyst interface pushes the CNT outward from its base. The interaction strength between the catalyst and the support largely determines which mechanism dominates, weak interactions favour tip growth, while strong interactions promote base growth. Catalyst particle size also plays a role, with smaller NPs tending to support base growth, while larger ones often lead to tip growth. The orientation of CNT growth relative to the catalyst can be either tangential or perpendicular. In tangential growth, the CNT forms along the catalyst surface, resulting in similar diameters for the CNT and the NP. In perpendicular growth, the CNT emerges from a localised region of the NP, typically observed with larger catalyst particles. Figure 2.6 summarises the different CNM growth modes.

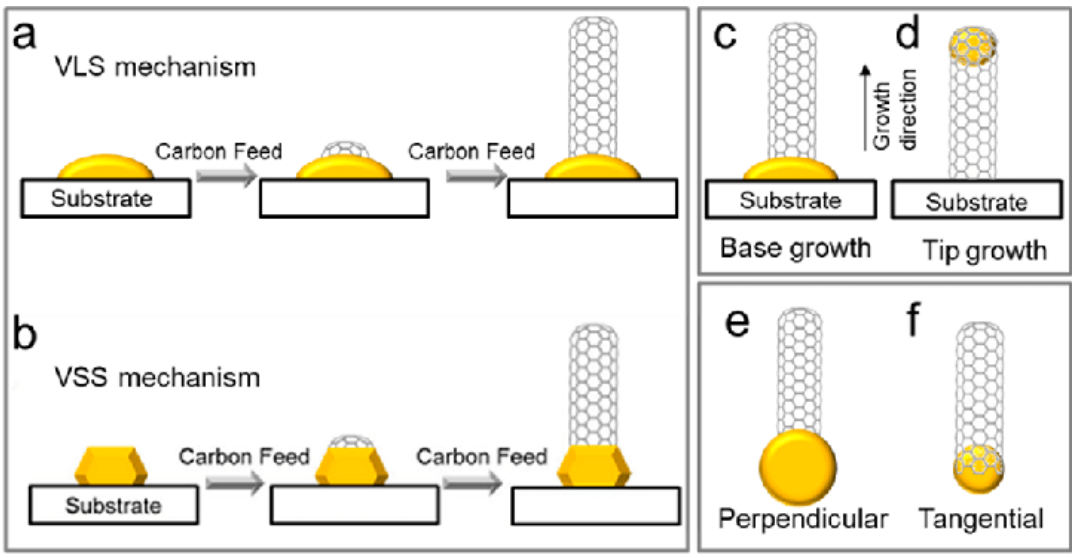


**Figure 2.6.** *Schematic illustration of CNT growth mechanisms and modes showing (a) Vapor–liquid–solid (VLS) mechanism, (b) Vapor–solid–solid (VSS) mechanism (c) Base growth mode, (d) Tip growth, (e) Perpendicular growth (f) Tangential growth [57].*

### *2.4.8 Carbon Separation*

The separation of CNMs from the catalyst is an inherently challenging process, with increased carbon purity typically coming at the expense of structural integrity [58], [59]. Additionally, the removal of transition metal nanoparticles and aluminosilicate supports relies on fundamentally different chemical mechanisms, therefore increasing the complexity of CNM separation from a supported catalyst [60]. Metal removal typically requires chemical treatments due to strong carbon-metal interactions, with encapsulated or pore-confined metal nanoparticles being particularly difficult to extract. Acid leaching is effective at dissolving accessible transition metal species, although are prone to introduce defects into the graphitic lattice, reducing product quality [59], [61]. Chelating agents, such as EDTA, provide a milder alternative, offering a potential route to separation with less CNM damage. Although, chelates are principally effective at ionic species such as metal oxides, and therefore requiring pre-processing to be effective for pure metallic nanoparticles, with this oxidation step itself potentially causing damage [62]. Furthermore, the large size of some common chelate molecules can reduce the ability of them to reach metal sites. The removal of aluminosilicate supports is dependent on the degree of CNM binding or entanglement [60]. Physical methods such as ultrasonication may be sufficient to detach loosely bound, surface-grown CNMs, although will likely by ineffective at strongly bound or framework encapsulated. For these, chemical dissolution of the aluminosilicate framework is required, most commonly achieved through alkaline or acid treatment

[60]. Therefore, for the optimal separation process a multi-stage chemical and physical process is likely required [63].

## 2.5 The Effect of Catalytic Metallic Species

The choice of metal species used for the catalytic conversion of waste plastics into CNMs plays a critical role in determining product yield, quality, and morphology. The effectiveness of each metal depends on its ability to crack hydrocarbon precursors, sustain carbon diffusion and guide the formation of structurally uniform highly graphitic CNMs. To achieve this, metal NPs with small diameters and high thermal stability at reaction temperatures are desired, as larger particles tend to become inactive for CNM growth. The strength of metal–support interactions (MSI) varies by metal and is crucial for stabilising NP morphology under reaction conditions. Therefore, optimal metal species is dependent on the specific support material used.

In addition to the catalyst composition, reactor configuration, processing conditions and feedstock type will all influence catalytic performance. The feedstock type and reactor set up will affect the flux and chemical composition of the hydrocarbon precursor reaching the catalyst. The catalysts ability to efficiently decompose precursor molecules will be more important for higher molecular weight feedstocks. Temperature affects which growth mechanism dominates, with metal catalytic properties such as carbon solubility influencing their effectiveness in following either VLS or VSS mechanisms. Therefore, the suitability of each metal is not absolute but context-dependent, shaped by its synergy with the support and the operating environment.

However, the wide variation in experimental conditions, reactor configurations, supports used and feedstock types in different studies makes it challenging to directly compare the performance of different metallic species. As a result, comparative investigations conducted under consistent and controlled conditions are essential to accurately evaluate the influence of metal species, catalyst preparation, and support pairing. This section reviews the role and relative performance of Fe, Ni and Co monometallic and bimetallic catalysts. These species are selected due to their high performance and low cost, as detailed in the introduction chapter. A focus is put on identifying the mechanistic factors that govern their relative effectiveness in converting plastic waste into high-quality carbon nanomaterials. Some of the results from key papers are summarised in Table 2.1.

**Table 2.1.** *Results from key papers evaluating the performance of different metal species.*

| Catalyst | Stages | Feedstock | Conversion (% Feedstock to Carbon) | Ratio | Reference |
|---|---|---|---|---|---|
| $Fe/Al_2O_3$ | Multi | LDPE | 17.9 | 0.51 | [64] |
| $Co/Al_2O_3$ | | | 6.8 | 0.82 | |
| $Ni/Al_2O_3$ | | | 9.6 | 0.74 | |
| $Cu/Al_2O_3$ | | | 4.7 | 0.85 | |
| $Fe_2O_3$/AC | Single | PP | 5 | Unknown | [65] |
| $Co_2O_3$/AC | | | 12 | Unknown | |
| $Ni_2O_3$/AC | | | 45 | Unknown | |
| $Fe/Al_2O_3$ | Multi | MIXED | 32.6 | 0.72 | [66] [67] |
| $Ni/Al_2O_3$ | | | 21.1 | 0.95 | |
| $FeNi/Al_2O_3$ | | | 40.7 | 0.43 | |

### *2.5.1 Monometallic*

Iron and nickel are the most extensively studied monometallic metals for CNM synthesis from waste plastics, whereas Cobalt has garnered less attention, and has been found to display lower performance. For instance, Acomb et. al. classified the Co-derived carbon as mostly amorphous through temperature programmed oxidation (TPO) analysis, a finding often used to justify the exclusion of Co from subsequent studies. However, this interpretation may be misleading, as Co can reduce the oxidation temperature of carbonaceous materials, potentially shifting the TPO peak position and underestimating the proportion of filamentous carbon. In fact, SEM and TEM imaging from the Acomb et. al. paper revealed that the carbon formed on $Co/Al_2O_3$ included a substantial population of multi-walled CNTs with uniform diameters and low structural variability. Mechanistically, Co's moderate performance has been attributed to strong MSI with the support, particularly with $Al_2O_3$. TPR data showed that the $CoAl_2O_4$ spinel phase remained unreduced up to 900°C under hydrogen, suggesting that reduction to catalytically active $Co^0$ may be hindered. However, post-reaction XRD of the used catalyst confirmed the presence of metallic Co, suggesting that the hydrocarbon pyrolysis products were capable of reducing Co under in situ conditions, enabling highly uniform CNT formation.

Indeed, Co-based catalyst are use in the synthesis of high-purity single-walled CNTs by CO disproportionation and alcohol CVD routes. These systems rely on Co's ability to nucleate highly uniform, narrow-diameter CNTs when paired with suitable promoters and supports. The success of these formulations indicates the potential of Co-based catalyst, with Co's application to plastic to CNT conversion underexplored yet mechanistically promising. Therefore, Co-based catalyst in plastic feedstock systems warrant further investigation, particularly in combination with non-traditional support supports or NP formation promoters.

Iron consistently demonstrates high catalytic performance across multiple studies, especially in two-stage pyrolysis systems, where pyrolysis vapours are converted to carbon over a downstream catalytic bed. Fe-based catalysts have displayed high performance for the conversion of plastic to CNMs. A foundational paper on the effect of different metal species on plastic conversion to CNTs by Acomb et. al., found that $Fe/Al_2O_3$ catalyst displayed a superior performance in terms of yields and graphitisation quality compared to $Co/Al_2O_3$ and $Ni/Al_2O_3$ for converting LDPE [64]. The superior performance of Fe was attributed to the higher carbon solubility of Fe, along with intermediate MSI strength, which enabled effective reduction to $Fe^0$ while avoiding sintering, issues which effected other catalysts [64].

Multiple papers have further confirmed the superior performance of $Fe/Al_2O_3$ over $Ni/Al_2O_3$ in terms of yields and graphitisation in similar two-stage processes, using a feedstock of PP [68] and mixed plastic feedstocks [67]. Fe-derived CNTs were consistently found to be longer, with a more uniform, attributed to the well dispersed and Fe's high catalytic activity [67]. These results show, Fe is a highly effective catalyst for carbon nanomaterial synthesis from a variety of waste plastics, outperforming other metals in multiple traditional two-stage systems.

Although iron generally outperforms nickel in conventional systems, there are several cases where Ni delivers superior results, particularly in non-traditional set up. These include one-stage processes [69], using non-traditional support [69] [54] or when processing complex or impure feedstocks [70]. These include uses of cordierite as a support material [69], the processing of recovered PE-rich landfill waste [70] and AC supporting both one [54] and two stage processing. In each of these cases, these was a vastly lower performance of Fe compared to Ni, suggesting a susceptibility to catalytic deactivation under certain conditions.

The consistently strong performance of Fe across multiple studies can be attributed to its favourable mechanistic and structural properties. Its high carbon solubility supports a bulk-mediated VSS growth mode with rapid carbon diffusion, enabling efficient high yield CNT synthesis, particularly in two-stage reactors where partial decomposition occurs before CVD. Additionally, Fe supports more stable carbon cap formation during nucleation than the other metals, enhancing the likelihood of sustained CNT growth.

The lower carbon solubility of Ni restricts carbon accumulation potential, and thus reduces yields compared to Fe, but makes it more resistant to this poisoning. Although, Ni displays higher effectiveness at supporting surface-mediated CNM growth and strong hydrocarbon cracking ability, makes Ni more resistant to deactivation from carbide formation and carbon oversaturation. Whereas, Fe is more prone to carbon oversaturation, leading to deactivation from amorphous or graphitic can layers around the catalyst, or inactive carbide phase formation. These are a particularly high risk at lower temperatures where carbon can over accumulate before effective bulk diffusion and precipitation can occur. The same mechanism makes Fe more prone to catalyst poising by impurities, such as sulphur, oxygen, or halogens, which can become incorporated in the metallic crystalline structure, explaining the low Fe yield found by [70]. Carbon oversaturation can explain the poor performance of Fe/AC catalysts, with the support material itself inducing this effect, demonstrating the Fe's lower versatility for support pairing. Thus, while Fe-based catalyst offers a higher potential ceiling in optimal conditions, Ni-based catalyst can outperform them particularly in more to challenging synthesis condition [64] [67].

### *2.5.2 Bimetallic Catalysts*

While Fe and Ni individually exhibit strong catalytic activity, numerous studies have shown that combining them into FeNi bimetallic systems produces synergistic effects, and thus improving catalytic performance [67] [68] [71] [72]. Yields and quality of FeNi based catalysts are consistently higher than their monometallic counterparts in $Al_2O_3$ supported two-stage processes, using a variety of feedstocks [67] [68] [71] [72]. Although, the largest discrepancy in yields was found using a one-stage process, demonstrating the intrinsic synergistic effects of the FeNi bimetallic catalysts. In general, the bimetallic catalyst generated longer MWNTs with greater uniformity and reduced structural defects, compared to more curved, short and irregular carbon structures on their monometallic counterparts [68] [71] [72].

The Fe:Ni ratio is a key element in determining the performance of the bimetallic catalyst. Yao et. al. found that FeNi/$Al_2O_3$ with higher Fe favoured higher carbon yields higher yields, whereas increasing the Ni content improved quality. Similarly, Li et al. found higher Fe content promoted carbon yield in unsupported systems. Therefore, these studies indicating that tuning of the bimetallic ratio is a balance between different desirable traits in the CNM product. Li et al. also investigated varied catalyst loadings relative to plastic mass, finding yields began to decrease at just 1 %wt metal loading, indicating that reduction of catalytic activity due to sintering can occur at with low loading in non-supported systems. Additionally, it has been found that 800oC is the optimal temperature for FeNi/$Al_2O_3$ catalysts, with increased yields and graphitisation compared to lower temperature [73]

The enhanced performance of FeNi bimetallic systems is primarily attributed to synergistic effects between the metal species, enhancing overall catalytic performance. The formation of mixed oxide phases, such as $NiFe_2O_4$ spinels, during catalyst preparation which show greater stability compared to monometallic oxides. Therefore, improved fresh catalyst dispersion promoting smaller more uniform NPs and increased sintering resistance during reduction can be achieved, promoting catalyst longevity.

Fe and Ni each bring distinct benefits to catalytic performance. Nickel excels at hydrocarbon decomposition, while iron supports higher carbon solubility and diffusion. FeNi NPs often form a core-shell arrangement, typically with a Ni-rich core and Fe-rich shell. This allows carbon to dissolve efficiently at the Fe surface and diffuse inward, while the Ni core stabilises the particle structure and maintains catalytic activity [72]. Additionally, FeNi alloying alters the electronic structure of the catalyst by tuning the d-band centre. This increases the density of states near the Fermi level, which may enhance hydrocarbon adsorption and promoted dehydrogenation reaction, leading to more efficient hydrocarbon cracking [74]. The performance of Fe Ni and the bimetallic are summarised in Figure 2.7.

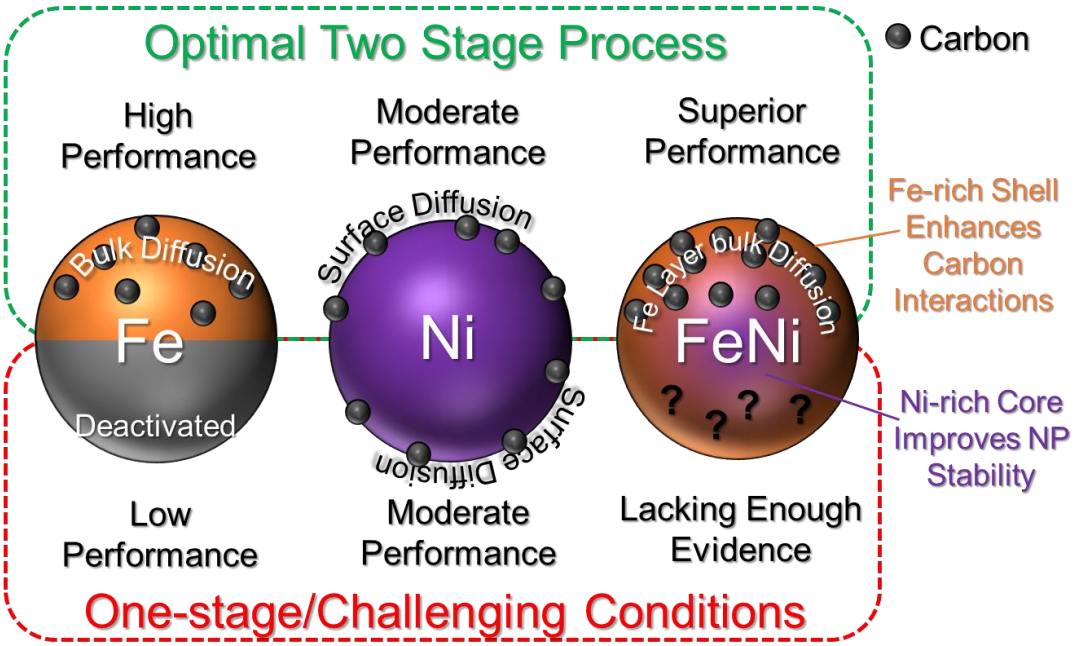


**Figure 2.7**. *Schematic showing the performance and preferred growth mechanisms of Fe, Ni and FeNi under different growth conditions.*

### *2.5.3 Secondary Modifier Metallic Species*

Beyond binary FeNi systems, combining active Fe, Ni, or indeed Co with a secondary catalytic modifying metal has shown promising results in enhancing catalytic performance. These secondary metals often act as promoters rather than actives species themselves, influencing key parameters such as MSI, reducibility, NP dispersion and active phase formation. The effects observed depend strongly on the metal pairings and their influence on CNT growth dynamics, with both promoting and hindering effects observed depending on the metallic species.

Magnesium has displayed a detrimental effect on catalytic performance. Carbon yield dropped sharply highly filamentous for monometallic Ni, to primarily amorphous carbon with the addition of Mg [75] [69]. This was attributed to overly strong MSI and the formation of inactive spinel phases like Ni $Al_2O_4$ and Mg $Al_2O_4$, contributing to a lower surface area reducing the number of accessible active sites [69]. Copper inclusion to Ni based catalysts showed mixed results, on one hand the bimetallic catalyst achieved a significantly higher carbon yield than monometallic Ni [76]. Although, this came at a cost to structural quality with the product displaying a lower graphic order and less uniform CNTs [76].

Two species which have been found to consistently displayed improved performances over other metallic species or monometallic counterpart is Manganese (Mn) and

molybdenum (Mo). Nahil et. al. [75] conducted a comparative study of alloying Ni and Al with different metals [75]. The catalysts are prepared using a co-precipitation method, with Al in a metallic phase rather than Al2O3. The Ni-Mn catalyst exhibited the highest carbon deposition, significantly outperforming Ca and Ce metal species. Although, the poorer quality and yields when compared to work using $Al_2O_3$ suggests that the oxide support form is preferable to the than in metallic form of Al. Additionally, Mn has shown to improve the performance of Fe-based catalysts in terms of yield and quality in a two-stage process using a PP feedstock [77]. The FeMn NPs were found to be smaller and more evenly dispersed, which likely contributed to more uniform and filamentous carbon formation [77].

The incorporation of Mo into Fe-based catalysts has been shown to significantly improve catalyst performance. For instance, the inclusion of Mo in Fe/MgO systems has resulted in approximately double the carbon yield [78] [77]. Likewise, Mo has also proven effective in combination with other transition metals, with both NiMo [79] and CoMo [80] based catalysts demonstrated high performance for the conversion of plastic to CNMs. Furthermore, Dong et. al. [81] combined Mo with Fe, Co and Ni, supported on MgO for the catalytic pyrolysis of biomass and plastics, with substantial improvements observed for all three-metal species. These findings highlight Mo's capacity to synergistically improve the performance of various transition metals for improved CNM synthesis

The performance enhancements observed with the addition of Mn or Mo can be attributed their multifaceted role in enhancing catalytic activity of Fe, Co and Ni. The oxide phases of Mn and Mo coat or embed in the surface of Fe, Co or Ni oxide NPs during synthesis, providing multi-faceted stabilising effects. During thermal reduction, these oxides acts as a dynamic redox buffer which can cycle between different oxidation states [82]. This moderates the formation of active metallic NPs, allowing for a more controlled reduction, and can improve dispersion and control catalytic activity.

Mn and Mo serve as physical barriers that limit NP sintering and migration at high temperatures, although the mechanisms vary between the two species. Mn tends to form a more coherent shell around particles, leading to superior NP dispersion and preventing sintering [83]. Additionally, Mn can act as an interfacial binder that reinforces anchoring between the catalyst and the support surface, further reducing particle agglomeration [83]. Mo, on the other hand, can migrate to the support surface,

modifying the support itself and enhancing acidic or basic surface properties, which indirectly influences catalytic performance. Additionally, this can strengthen MSI and thus suppress sintering of metallic NPs and potentially improve catalytic performance [84][85]. Although, excessive loading of either element is detrimental. High Mn concentrations can lead to catalytically inert Mn-rich alloys, diluting the activity of Fe or Ni [86]. Similarly, excess Mo can form carbides or large oxide aggregates that hinder active sites, disrupting the uniformity.

## 2.6 Effect of Support

Catalyst performance in converting plastics to CNMs is highly dependent on the choice of support. As seen previously, MSI plays a central role by influencing how metal species are dispersed, stabilised and retained. Different metal-support pairings induce unique MSI effects, making the combination more important than the individual components alone. The physical characteristics of the support, such as surface area and porosity, affect NP dispersion and the availability of active sites. In addition, some supports actively catalyse precursor breakdown and regulate carbon delivery to the metal NPs, which further shapes CNM yield, quality and morphology. In addition, the support characteristics play a role in carbon delivery to these active sites, with porosity allowing for bulk precursor diffusion and acid sites catalysing precursor breakdown.

### *2.6.1 Carbon-based Supports*

Carbon-based supports have garnered increasing attention for the synthesis of CNMs, due to their high porosity and surface area, tunability of surface functional groups and inherent thermal stability. Carbon supports are often derived from renewable or waste biomass, promoting the process sustainability. In the context of plastic waste conversion, their ability to stabilise dispersed metal NPs, facilitate hydrocarbon cracking, and influence carbon morphology has been demonstrated across a number of studies. The use of activated carbon, carbon black, and biomass-derived chars have all been shown to produce high quality and yield CNMs.

Modekwe et. al. [87] directly compared the influence of different activation methods, namely non-activated, chemical with KOH and steam activated on the performance of NiMo/AC for PP conversion. Chemical activation yielded the highest CNT yield due to increased surface area and potassium incorporation, which enhanced precursor formation and AC porosity. The resulting CNTs were long, entangled and moderately structured. Steam activation led to s much lower yield but the most crystalline CNTs with a narrower diameter. This was attributed to the formation of metastable $NiMoO_4$

phases, which are catalytically inactive thus reducing yield, but stabilise NP formation thus leading to disperse, small diameter NPs. Additionally, the surface area of the steam active catalyst was the lowest. Non-activated support produced an intermediate yield of bamboo-like CNT structures. The absence of additional chemical species indicate carbonisation was driven more by intrinsic properties of the carbon.

Gong et. al. [54] investigated how different surface functionalisation treatments of AC influence the catalytic performance of $Ni_2O_3$-based systems in the conversion of PP. Air-oxidised AC and untreated AC exhibited the highest hydroxyl group content and correspondingly produced the highest CNT yields. This suggests that surface functional groups, particularly hydroxyl groups, promote the formation of reactive intermediates during PP decomposition and enhance CNT growth. By contrast, hydrogen-treated ACs had significantly lower surface hydroxyl content, reducing the yields obtained using these catalysts. The removal of these surface functional groups reduced the acidity and the ability to stabilise intermediate aromatics, thereby impairing the CNT formation process.

The effectiveness of carbon-based supports has also been demonstrated by [55] by converting a mixed plastic feedstock using a CB support. They demonstrated that the CB support was more effective than traditional aluminosilicate supports for the conversion of plastic mixtures containing PS, which was found to be detrimental to the traditional support catalyst. This was attributed to the CB's ability to stabilise the aromatic intermediates formed during PS pyrolysis and therefore subsequently convert them into an organised carbon lattice.

Despite these promising results, carbon-based supports do have several drawbacks. A key limitation lies in the difficulty of separating the final carbon product from the support material. High temperature oxidation can selectively remove amorphous carbon while preserving graphitic structures, but this process demands precise temperature control. Even with such control, the overlapping oxidation temperatures of various carbon types often result in unintended damage to graphitic CNTs. Moreover, catalysts with high carbon solubility may not be ideal for carbon supports, as strong interactions with the support's carbon atoms can lead to oversaturation and carbide phase formation, hindering CNT formation.

### 2.6.2 Oxide Supports

Oxides used as supports can be broadly grouped into alkaline earth, transition metal, basic metal, and mixed metal categories, each imparting distinct chemical and structural effects on catalytic behaviour. The type of oxide species has a profound impact on catalytic performance by modulating the catalyst's chemical reactivity, structural stability, and compatibility with the metal phase.

Among commonly studied supports, $Al_2O_3$ consistently demonstrates superior catalytic performance across both nickel and iron-based systems. In the conversion of PE, Li et al. [88] reported that Ni/$Al_2O_3$ produced the highest carbon yield and most graphitic carbon, forming uniform bamboo-like MWNTs. Whereas, Ni/$ZrO_2$ and Ni/$Nb_2O_5$ yielded negligible filamentous carbon and instead formed disordered CNOs and amorphous aggregates with low graphitic quality. $Al_2O_3$ has also demonstrated superior performance in Fe-based catalysts for PP conversion, with a moderate yield improvement over Fe/$SO_2$ and Fe/$TiO_2$. Additionally, the Fe/$TiO_2$ catalyst formed mostly twisted carbon nanofibers with inferior structural order, as opposed to the CNTs observed on $Al_2O_3$ and $SiO_2$.

Veksha et. al. [89] investigated how forms of different calcium-based supports influence the performance of nickel catalysts for decomposing plastic-derived hydrocarbons. Among the supports tested, $CaCO_3$ and $Ca(OH)_2$ clearly outperformed CaO, facilitated the formation of MWCNTs, with moderate graphitic quality. In contrast, Ni/CaO produced predominantly non-filamentous carbon and exhibited the poorest level of graphitisation for the tested catalysts. This was attributed to significantly greater pore volumes and higher surface areas of $CaCO_3$ and $Ca(OH)_2$ compared to CaO. These porous properties enabled better dispersion of Ni NPs, improved catalytic accessibility, and more effective decomposition of hydrocarbons. Furthermore, the basic nature of $CaCO_3$ and $Ca(OH)_2$ enhanced hydrocarbon cracking and polyaromatic intermediate formation, which are beneficial for CNT growth.

Calcium-based supports were further investigated by Modekwe et. al. [90] et. al. with the performance of mixed oxide supports in comparison to single metal oxides evaluated for converting PP into CNMs. $CaTiO_3$ demonstrated superior performance with the highest carbon yield and most graphitic CNTs, indicating the synergistic potential of mixed metal oxide support. Despite having a moderate surface area of, its large pore size and the presence of metastable crystalline phases enhanced metal

dispersion, suppressed NP agglomeration and improved catalyst stability. Furthermore, while other catalysts followed a tip-growth mechanism, NiMo/$CaTiO_3$ favoured base-growth, indicating a stronger MSI which anchored the NPs during CNT formation, which improved the uniformity of the CNTs grown.

Jia et. al. [91] et. al. tested $La_2O_3$, MgO, and SrO effect on the performance of nickel-based catalysts in converting LDPE and PP. The Ni/$La_2O_3$ catalyst showed the best performance, achieving the highest carbon yield of mostly high-quality bamboo-like multi-walled CNTs. This was attributed due to moderate MSI, promoting nickel dispersion and reduction. Ni/Mg, with strong MSI, stabilised smaller nickel particles but hindered reduction, resulting in a lower yield and limited CNT formation. Whereas, Ni/Sr, with weak MSI, had poor nickel dispersion and particle stability, leading to sintering and the formation of defective CNTs and carbon nano-onions. Although some non-traditional oxide supports such as $La_2O_3$ show strong catalytic potential, its high cost limits large-scale feasibility. In comparison, $Al_2O_3$ is not only widely available and cost-effective but has consistently shown good performance across a range of catalytic systems. While the alternative oxides may not match the full potential of $Al_2O_3$-based supports, these studies highlight how properties such as porosity, balanced MSI and surface functional groups are critical in enhancing catalytic efficiency and CNT quality.

### *2.6.3 Aluminosilicate Supports*

Aluminosilicates are a diverse group of materials with a range of structures and properties, which include zeolites, clays and mesoporous aluminosilicates. Zeolites are crystalline aluminosilicates characterised by a highly ordered framework composed of $SiO_4$ and $AlO_4$ tetrahedra linked by shared oxygen atoms. Zeolites have a well-defined microporous network, which can exhibit 1D, 2D or 3D pore channels which imparts high surface area and porosity. The substitution of $Si^{4+}$ by $Al^{3+}$ in the framework introduces a negative charge, which is balanced by extra-framework cations. This introduces strong acid sites into the zeolite framework, which can be enhanced by increasing the Al/Si, offering a high degree of control over catalytic performance. Mesoporous offer larger pore sizes than zeolites and facilitate the diffusion of bulky molecules, making them suitable for plastic waste conversion. However, their synthesis often requires template-assisted or surfactant-directed methods, which are more complex and expensive compared to conventional supports. Clays are natural abundant and inexpensive, and typically display a

phyllosilicate structure with a layered morphology and interlayer cation. These features can offer a uniform surface for metal dispersion and stabilisation, although the lack of porosity and low acidity may limit catalytic performance.

The performance of zeolite and clay-based supports was tested by Song et. al. [92] [93] using Beta zeolite, H-ZSM-5 zeolite and montmorillonite clay as a support for $Ni_2O_3$. It was found that Beta yielded a significantly higher carbon outperformed the other supports, producing a high carbon yield and greater MWNT purity. This enhanced activity was attributed to H-Beta's stronger acidity and larger pore size, which facilitated better hydrocarbon cracking and access to active sites, respectively. The thermal behaviour of the Beta support may also be beneficial, with partial structural breakdown under high-temperature conditions exposing new acid sites during the reaction, effectively increasing in situ catalytic surface area and enhancing overall conversion efficiency.

Yao et al. [94] expanded this comparative framework by employing Ni-Fe bimetallic catalysts on different zeolite and mesoporous supports, including MCM-41, ZSM-5, Beta, and NKF-5, for converting mixed plastic waste. Ni-Fe/MCM-41 exhibited the highest carbon yield and graphitisation, a result attributed to its high surface area and mesoporous structure, which supported excellent metal dispersion and reactive intermediate diffusion. Ni-Fe/ZSM-5 and Ni-Fe/Beta performed intermediately, while Ni-Fe/NKF-5 displayed the worst performance largely due to its limited pore volume and poor metal dispersion. This indicates the promise of mesoporous silica supports. Indeed, Yang et al. [95] studied the effect of aluminium incorporation in mesoporous silica material SBA-15, when used as a support for Ni-based catalyst. They found that the acidity and mesoporous structure could be precisely tuned by varying the Si/Al ratio, thereby modulating CNT yield and quality. Catalysts with moderately high aluminium content provided an optimal balance, enhancing precursor cracking without excessive acidity leading to structural collapse and hindered metal dispersion.

These results indicate zeolites and ordered aluminosilicates have several features which give them high potential of as supports for plastic conversion to CNM. The presence of strong acid sites, enhance catalysing dehydrogenation, cyclisation, and aromatisation reactions, which generate polyaromatic intermediates for CNT nucleation [92] [93]. The larger pore materials support the diffusion of bulky hydrocarbon molecules and promote efficient mass transfer throughout the catalyst matrix, thereby improving access to active sites, and leading to uniform CNT growth

and improved graphitisation [92] [93]. Additionally, the regular ordered porous structure of the support surface can impart regularity to the dispersion of metal NPs.

## 2.7 Preparation Methods

The method and any pre-processing steps used to disperse metal species onto a support material can significantly influence catalytic performance. The preparation technique governs the dispersion of metal NPs on the catalyst and influences the MSI. Additionally, preparation method can alter key support characteristics such as surface area and porosity. Several alternative approaches have been investigated with the aim of improving catalyst structure and performance. This section covers these methods, their current applications and catalytic changes they can make which effect performance.

### *2.7.1 Wet Impregnation*

Typically, wet impregnation is employed due to its simplicity and cost-effectiveness. This involves dissolving a metal salt into a solvent and thus liberating the metallic ions. A supporting material can then be added to this solution, allowing for the metal to bind to the support. However, the undirected nature of metal ion distribution in solution onto a pre-formed crystalline can lead to uneven dispersion, resulting in a heterogeneous catalyst that is less effective for the growth of ordered CNMs. This is a particular issue for supports lacking ordered porosity, such as alumina, as surface adsorption limits the integration of metal species and support matrix and can allow for agglomeration. Although for zeolites wet impregnation can be more effective, as it allows for ion exchange into the pores and thus more even distribution of metal species due to the regular crystalline structure.

### *2.7.2 Sol-Gel Preparation of Alumina-Supported Catalyst*

To address the limitations of the wet impregnation method, sol-gel (SG) $Al_2O_3$-supported catalysts have been tested. The SG method is a versatile synthesis technique that enables the homogeneous dispersion of metal species within a support matrix. It begins with dissolving a metal alkoxide precursor in a solvent such as alcohol or water, typically aluminium-tri-sec-butoxide (ATB). Hydration of this precursor leads to hydrolysis, forming hydroxyl groups that condense into a three-dimensional metal-oxygen network. This process produces a colloidal suspension of alumina NPs that, over time, crystallises into larger $Al_2O_3$ phases, ultimately forming a gel with improved porosity and increased surface area.

Yao and Wang [68] found that sol-gel-derived FeNi catalysts exhibit a specific surface area more than double that of wet-impregnated counterparts, with Jagodzińska et al. [70] reporting an approximately three times increase. The FeNi metal salt solution can be introduced either at the start of the sol-gel process or after partial $Al_2O_3$ crystallisation. Early addition typically promotes the formation of crystalline spinel phases like $NiAl_2O_4$ upon calcination. In contrast, later-stage addition is preferred for CNM catalysts, allowing for improved surface-dispersed metal NPs. This approach often yields metastable surface-mixed oxides and non-stoichiometric phases [96]. These intermediate phases enhance MSI and metal NP dispersion. Indeed, Yao and Wang [68] found that SG prepared FeNi catalysts achieved a higher metal dispersion and availability of active sites compared to wet impregnation.

These improved structural and catalytic properties result in sol-gel-derived FeNi catalysts outperforming their wet-impregnated counterparts. For instance, Yao and Wang [68] reported improved conversion of PP to a higher quality CNTs with a SG catalyst compared to a traditional wet impregnation. TEM revealed that the SG prepared catalyst had less amorphous carbon deposited, particularly on the outer MWNT walls. The increased performance was attributed to the amorphous matrix and uniform metal distribution in the sol-gel catalysts further helped prevent sintering, in contrast to the crystalline and less porous structure seen in impregnated catalysts. Jagodzińska et al. [70] further supported these findings, higher conversion and significantly higher carbon quality from the sol-gel-prepared catalyst in the conversion of landfill recovered PE to CNTs. Therefore, demonstrating the robustness of SG prepared catalyst to deal with challenging feedstock.

### *2.7.3 Hydrothermal Synthesis of Zeolites*

Hydrothermal synthesis is a widely employed technique for the crystallisation of zeolite-based supports. This method typically involves dissolving silicon and aluminium precursors in an alkaline aqueous solution, followed by crystallisation under elevated temperatures and autogenous pressure in a sealed autoclave [97]. The introduction of metal precursors during the synthesis stage allows for direct interaction between metal ions and the forming crystalline matrix, similar to sol–gel preparation methods used for alumina-based catalysts. The hydrothermal route enables the incorporation or anchoring of metal ions preferentially within the zeolite framework over on the zeolite surface, especially compared to traditional impregnation [98]. Upon calcination, the inherent porosity of the zeolite can direct the

formation of well-dispersed metal NPs, resulting in a controlled size distribution. Metal-zeolite composites synthesised by this method often exhibit strong MSI and enhanced thermal stability [99].

However, a key limitation of this approach is that metal ions embedded deeply within the microporous structure may be inaccessible to hydrocarbon feedstocks or may be geometrically constrained, thereby limiting their catalytic effectiveness [100]. This reduced accessibility can result in fewer active surface sites available for CNM nucleation and growth, ultimately lowering catalytic activity and yield. Additionally, typically laboratory-scale hydrothermally synthesised zeolites are often lower in structural uniformity compared to commercially produced materials. Small, relatively simple autoclave systems provide less precise control over parameters such as temperature gradients, mixing and pressure stability compared to large-scale industrial reactors. As a result, lab-prepared zeolites may exhibit incomplete crystallisation causing a higher defect density and a greater variation in crystal size. This can affect catalytic performance by altering the framework thermal stability, metal site dispersion and precursor cracking ability, due to acidity and porosity changes. Therefore, hydrothermal synthesis is not typically the preferred method for preparing CNM growth catalysts. Nonetheless, due to its ability to achieve high metal dispersion, it has the potential to have beneficial results in terms of CNM structure, morphology or uniformity.

### *2.7.4 Metal Complexing Agents*

The incorporation of complexing agents during catalyst preparation offers a practical strategy for improving NP morphology and dispersion. These additives form stable chelates with transition metal ions in solution. By temporarily sequestering the metal ions, these agents regulate their availability during drying and calcination, preventing premature aggregation or precipitation. This results in finer, more uniformly distributed metal NPs with narrower size distributions, which enhances catalytic activity and selectivity. Although their application in catalysts for plastic-to-CNM conversion is limited, promising results from traditional catalyst systems suggest high potential. For instance, chelating agents have been shown to produce highly dispersed, thermally stable NPs when used with iron and nickel precursors, indicating that their application could be similarly beneficial in plastic pyrolysis contexts [101]. Furthermore, their role in enhancing MSI could help balance dispersion and stability, particularly when combined with porous supports or bimetallic systems. This method has been used to

prepare catalysts for CNM synthesis using citric acid [102] or EDTA [103], although the effect of these in combination with a plastic feedstock is unclear.

## 2.8 Conclusion

Catalyst design for efficient conversion of polyolefins to CNMs relies on the integration of multiple interconnected factors. Enhanced catalytic performance can be achieved through selection of optimal active metal species, inclusion of secondary stabilising metals, favourable metal-support combinations and preparation methods that enhance overall catalyst structure.

The choice of metallic species is central to the efficiency and selectivity of CNM synthesis from waste plastics. Iron consistently delivers superior carbon yields and CNT quality in two-stage systems, owing to its high carbon solubility and balanced MSI. However, its performance declines in one-stage or impurity-rich conditions due to sintering, carbide formation, and susceptibility to poisoning. Nickel, while typically yielding less carbon, is more resilient under these challenging scenarios thanks to its robust surface-mediated cracking and resistance to deactivation. Cobalt, although less explored, exhibits promising features such as uniform CNT morphology and stable small NPs. FeNi bimetallic catalysts outperform monometallic ones by leveraging synergistic effects that enhance NP dispersion, thermal stability, and catalytic activity. Incorporating secondary metals like manganese and molybdenum improve the catalytic behaviour of the active metal catalyst species by tuning MSI, enhancing reducibility, and stabilising small well dispersed NPs.

Support materials play a critical role in determining catalyst performance by regulating MSI strength, NP dispersion, and hydrocarbon cracking. Strong MSI enhances thermal stability and reduces NP sintering, though excessively strong interactions can hinder catalytic activity. MSI also influences whether CNTs follow a tip- or base-growth mechanism, thereby affecting the resulting carbon morphology. High surface area and well-controlled porosity improve access to active sites for NP to form on. Furthermore, regular porous structures can impart uniformity to the NP distribution through favourable adsorption sites. The support can actively catalyse the decomposition of feedstock through acid site, thus improving yields. Porosity in combination with acid sites can facilitate precursor decomposition but also modulate the delivery of carbon species to the active sites, shaping both yield and structure of the CNMs. Mesoporous aluminosilicates and zeolites are some of the most promising options for catalyst support which display all these beneficial features.

The catalyst preparation method will strongly influence its overall structure and properties. Techniques that involve growing the support material in direct contact with metal ion solutions can produce a higher surface area catalyst with enhanced metal dispersion and induce a wider range of more complex MSI. Additionally, the use of additives such as complexing agents can further control NP formation by regulating the availability of metal ions during synthesis. This can lead to improved uniformity in particle size, better distribution across the support, and increased thermal and chemical stability of the final catalyst. This shows the complex interconnecting roles of the catalyst elements, indicating a holistic approach to catalyst design will allow for improvements in catalytic performance.

Despite these insights, several research gaps remain:

1. Current literature lacks direct comparisons between different metal species and bimetallic species for their effectiveness on one-stage systems and whether synergistic effects found in two-stage can be achieved.
2. The integration of porous aluminosilicate materials as catalyst supports within one-stage pyrolysis systems remains insufficiently explored, despite their effectiveness as a support and as a pyrolysis catalyst.
3. The influence of catalyst preparation techniques on CNM aluminosilicate-supported catalysts is not clear, despite some favourable properties such as improved metal dispersion evidence from use in other applications.
4. While both molybdenum and manganese have shown effectiveness as promoters in CNM synthesis, there is a lack of direct comparative studies to determine which element is more effective in the context of plastic convention to CNMs.

Addressing these gaps defines the novelty of this work:

1. Comprehensive evaluation of mono- and bimetallic catalysts in a one-stage system, investigating how variations in metal composition and catalyst structure influence CNM growth mechanisms and overall performance.
2. Direct comparation of diverse catalyst support morphologies, interconnected 3D pore zeolite, linear 1D pored zeolite and flat clay, which will offer generalised insights into how support morphology governs CNM formation from plastics.

3. Influence of zeolite-supported catalyst preparation methods, with direct comparison of wet impregnation and hydrothermal synthesis methods and zeolite calcination temperature impacts.
4. Comparation of the roles of manganese and molybdenum as secondary promoter metals, providing insights into their individual and relative effects on catalytic performance in plastic to CNM conversion.

# References


[1] K. S. Novoselov *et al.*, “Electric Field Effect in Atomically Thin Carbon Films,” 2000.

[2] H. W. Lu *et al.*, “The promise of graphene-based transistors for democratizing multiomics studies,” 2022. doi: 10.1016/j.bios.2021.113605.

[3] K. Chen, Q. Wang, Z. Niu, and J. Chen, “Graphene-based materials for flexible energy storage devices,” 2018. doi: 10.1016/j.jechem.2017.08.015.

[4] M. F. El-Kady and R. B. Kaner, “Scalable fabrication of high-power graphene micro-supercapacitors for flexible and on-chip energy storage,” *Nat. Commun.*, vol. 4, 2013, doi: 10.1038/ncomms2446.

[5] L. H. Hess, M. Seifert, and J. A. Garrido, “Graphene transistors for bioelectronics,” *Proceedings of the IEEE*, vol. 101, no. 7, 2013, doi: 10.1109/JPROC.2013.2261031.

[6] “Mechanical Properties and Application of Graphite and Graphite-based Nanocomposite : A Review,” *Chemistry and Materials Research*, 2023, doi: 10.7176/cmr/15-1-02.

[7] J. Xu *et al.*, “Recent Progress in Graphite Intercalation Compounds for Rechargeable Metal (Li, Na, K, Al)-Ion Batteries,” 2017. doi: 10.1002/advs.201700146.

[8] J. D. Arregui-Mena *et al.*, “Multiscale characterization and comparison of historical and modern nuclear graphite grades,” *Mater. Charact.*, vol. 190, 2022, doi: 10.1016/j.matchar.2022.112047.

[9] H. W. Kroto, J. R. Heath, S. C. O’Brien, R. F. Curl, and R. E. Smalley, “Kroto Et Al 1985,” *Nature*, vol. 318, 1985.

[10] X. Lu and Z. Chen, “Curved Pi-conjugation, aromaticity, and the related chemistry of small fullerenes (<C60) and single-walled carbon nanotubes,” 2005. doi: 10.1021/cr030093d.

[11] M. Kumar and K. Raza, “C60-fullerenes as Drug Delivery Carriers for Anticancer Agents: Promises and Hurdles,” *Pharm. Nanotechnol.*, vol. 5, no. 3, 2017, doi: 10.2174/2211738505666170301142232.

[12] B. Saha, S. Shindo, S. Irle, and K. Morokuma, “Quantum chemical molecular dynamics simulations of dynamic fullerene self-assembly in benzene combustion,” *ACS Nano*, vol. 3, no. 8, pp. 2241–2257, 2009, doi: 10.1021/nn900494s.

[13] S. Holliday *et al.*, “High-efficiency and air-stable P3HT-based polymer solar cells with a new non-fullerene acceptor,” *Nat. Commun.*, vol. 7, 2016, doi: 10.1038/ncomms11585.

[14] L. K. Shrestha *et al.*, “Biomass Nanoarchitectonics for Supercapacitor Applications,” 2023. doi: 10.5650/jos.ess22377.

[15] S. Bibi, S. Urrehman, L. Khalid, M. Yaseen, A. Q. Khan, and R. Jia, “Metal doped fullerene complexes as promising drug delivery materials against COVID-19,” *Chemical Papers*, vol. 75, no. 12, 2021, doi: 10.1007/s11696-021-01815-4.

[16] V. Dhand, M. Yadav, S. H. Kim, and K. Y. Rhee, “A comprehensive review on the prospects of multi-functional carbon nano onions as an effective, high- performance energy storage material,” 2021. doi: 10.1016/j.carbon.2020.12.083.

[17] M. E. Plonska-Brzezinska, “Carbon Nano-Onions: A Review of Recent Progress in Synthesis and Applications,” 2019. doi: 10.1002/cnma.201800583.

[18] M. D’amora, V. Maffeis, R. Brescia, D. Barnes, E. Scanlan, and S. Giordani, “Carbon nano-onions as non-cytotoxic carriers for cellular uptake of glycopeptides and proteins,” *Nanomaterials*, vol. 9, no. 8, 2019, doi: 10.3390/nano9081069.

[19] O. Mykhailiv, H. Zubyk, and M. E. Plonska-Brzezinska, “Carbon nano-onions: Unique carbon nanostructures with fascinating properties and their potential applications,” 2017. doi: 10.1016/j.ica.2017.07.021.

[20] J. Bartelmess and S. Giordani, “Carbon nano-onions (multi-layer fullerenes): Chemistry and applications,” 2014. doi: 10.3762/bjnano.5.207.

[21] S. Kumar, H. Doshi, M. Srinivasarao, J. O. Park, and D. A. Schiraldi, “Fibers from polypropylene/nano carbon fiber composites,” *Polymer (Guildf).*, vol. 43, no. 5, 2002, doi: 10.1016/S0032-3861(01)00744-3.

[22] M. M. S. Awan, P. Soroushian, A. Ali, and M. Y. S. Awan, “Carbon nano fibre reinforcements in concrete,” *Indonesian Journal of Science and Technology*, vol. 4, no. 1, 2019, doi: 10.17509/ijost.v4i1.4140.

[23] M. Sharma, S. Gao, E. Mäder, H. Sharma, L. Y. Wei, and J. Bijwe, “Carbon fiber surfaces and composite interphases,” 2014. doi: 10.1016/j.compscitech.2014.07.005.

[24] D. Yadav, F. Amini, and A. Ehrmann, “Recent advances in carbon nanofibers and their applications – A review,” 2020. doi: 10.1016/j.eurpolymj.2020.109963.

[25] M. Zakaria, M. A. R. Bhuiyan, M. S. Hossain, N. M. M. U. Khan, M. A. Salam, and K. Nakane, “Advances of polyolefins from fiber to nanofiber: fabrication and recent applications,” 2024. doi: 10.1186/s11671-023-03945-y.

[26] L. Feng, N. Xie, and J. Zhong, “Carbon nanofibers and their composites: A review of synthesizing, properties and applications,” 2014. doi: 10.3390/ma7053919.

[27] J. Restivo, O. S. G. P. Soares, and M. F. R. Pereira, “Processing methods used in the fabrication of macrostructures containing 1d carbon nanomaterials for catalysis,” 2020. doi: 10.3390/pr8111329.

[28] S. Iijima, “Helical microtubules of graphitic carbon,” *Nature*, vol. 354, no. 6348, 1991, doi: 10.1038/354056a0.

[29] N. Wang, Z. K. Tang, G. D. Li, and J. S. Chen, “Single-walled 4 Å carbon nanotube arrays,” *Nature*, vol. 408, no. 6808, 2000, doi: 10.1038/35040702.

[30] M. He *et al.*, “Precise determination of the threshold diameter for a single-walled carbon nanotube to collapse,” *ACS Nano*, vol. 8, no. 9, 2014, doi: 10.1021/nn5042812.

[31] S. Hong and S. Myung, “Nanotube electronics: A flexible approach to mobility,” 2007. doi: 10.1038/nnano.2007.89.

[32] M. F. Yu, O. Lourie, M. J. Dyer, K. Moloni, T. F. Kelly, and R. S. Ruoff, “Strength and breaking mechanism of multiwalled carbon nanotubes under tensile load,” *Science (1979).*, vol. 287, no. 5453, 2000, doi: 10.1126/science.287.5453.637.

[33] H. W. C. Postma, T. Teepen, Z. Yao, M. Grifoni, and C. Dekker, “Carbon nanotube single-electron transistors at room temperature,” *Science (1979).*, vol. 293, no. 5527, 2001, doi: 10.1126/science.1061797.

[34] X. Wen *et al.*, “Nanosized carbon black combined with Ni2O3 as ‘universal’ catalysts for synergistically catalyzing carbonization of polyolefin wastes to synthesize carbon nanotubes and application for supercapacitors,” *Environ. Sci. Technol.*, vol. 48, no. 7, pp. 4048–4055, 2014, doi: 10.1021/es404646e.

[35] P. T. Williams, “Hydrogen and Carbon Nanotubes from Pyrolysis-Catalysis of Waste Plastics: A Review,” 2021. doi: 10.1007/s12649-020-01054-w.

[36] T. A. Saleh and V. K. Gupta, *Nanomaterial and Polymer Membranes: Synthesis, Characterization, and Applications*. 2016. doi: 10.1016/C2013-0-19381-6.

[37] A. J. Page, Y. Ohta, S. Irle, and K. Morokuma, “Mechanisms of single-walled carbon nanotube nucleation, growth, and healing determined using QM/MD methods,” *Acc. Chem. Res.*, vol. 43, no. 10, 2010, doi: 10.1021/ar100064g.

[38] K. Y. Amsharov, “Combinatorial approach for the synthesis of precursors for chirality-controlled synthesis of SWCNTs,” *Phys. Status Solidi B Basic Res.*, vol. 252, no. 11, 2015, doi: 10.1002/pssb.201552189.

[39] K. Shah *et al.*, “Conversion of pyrolytic non-condensable gases from polypropylene co-polymer into bamboo-type carbon nanotubes and high-quality oil using biochar as catalyst,” *J. Environ. Manage.*, vol. 301, 2022, doi: 10.1016/j.jenvman.2021.113791.

[40] D. C. Wang, Y. Lei, W. Jiao, Y. F. Liu, C. H. Mu, and X. Jian, “A review of helical carbon materials structure, synthesis and applications,” 2020. doi: 10.1007/s12598-020-01622-y.

[41] Q. Kong and J. Zhang, “Synthesis of straight and helical carbon nanotubes from catalytic pyrolysis of polyethylene,” *Polym. Degrad. Stab.*, vol. 92, no. 11, 2007, doi: 10.1016/j.polymdegradstab.2007.08.002.

[42] A. Shaikjee and N. J. Coville, “The synthesis, properties and uses of carbon materials with helical morphology,” 2012. doi: 10.1016/j.jare.2011.05.007.

[43] A. Shibuya, G. Chen, A. Miyoshi, and D. N. Futaba, “Improving the synthetic efficiency of single-wall carbon nanotube forests using a gas-analysis-designed mixed carbon feedstock,” *Carbon N. Y.*, vol. 170, pp. 59–65, 2020, doi: 10.1016/j.carbon.2020.08.001.

[44] M. F. L. De Volder, S. H. Tawfick, R. H. Baughman, and A. J. Hart, “Carbon nanotubes: Present and future commercial applications,” 2013. doi: 10.1126/science.1222453.

[45] S. Abdalla, F. Al-Marzouki, A. A. Al-Ghamdi, and A. Abdel-Daiem, “Different Technical Applications of Carbon Nanotubes,” 2015. doi: 10.1186/s11671-015-1056-3.

[46] L. Yaqoob, T. Noor, and N. Iqbal, “Conversion of Plastic Waste to Carbon-Based Compounds and Application in Energy Storage Devices,” 2022. doi: 10.1021/acsomega.1c07291.

[47] R. Das, Z. Shahnavaz, M. E. Ali, M. M. Islam, and S. B. Abd Hamid, “Can We Optimize Arc Discharge and Laser Ablation for Well-Controlled Carbon Nanotube Synthesis?,” 2016. doi: 10.1186/s11671-016-1730-0.

[48] A. I. Yardimci and N. Yagmurcukardes, “Synthesis methods of carbon nanotubes,” in *Handbook of Carbon Nanotubes*, 2022. doi: 10.1007/978-3-030-91346-5_52.

[49] M. José-Yacamán, M. Miki-Yoshida, L. Rendón, and J. G. Santiesteban, “Catalytic growth of carbon microtubules with fullerene structure,” *Appl. Phys. Lett.*, vol. 62, no. 6, 1993, doi: 10.1063/1.108857.

[50] J. Chase, C. Zhuo, and Y. A. Levendis, “Feasibility Study on Power Generation from Waste Plastics with Partial Precombustion Carbon Capture and Conversion,” *Journal of Energy Engineering*, vol. 141, no. 2, 2015, doi: 10.1061/(asce)ey.1943-7897.0000223.

[51] L. Dai *et al.*, “Holistic utilization of waste plastics through a tandem process,” *J. Environ. Chem. Eng.*, vol. 11, no. 5, Oct. 2023, doi: 10.1016/j.jece.2023.110547.

[52] H. U. Modekwe, M. O. Daramola, M. A. Mamo, and K. Moothi, “Recent advancements in the use of plastics as a carbon source for carbon nanotubes synthesis - A review,” 2024. doi: 10.1016/j.heliyon.2024.e24679.

[53] X. Zhou, L. J. Broadbelt, and R. Vinu, “Mechanistic Understanding of Thermochemical Conversion of Polymers and Lignocellulosic Biomass,” in *Advances in Chemical Engineering*, vol. 49, 2016. doi: 10.1016/bs.ache.2016.09.002.

[54] J. Gong *et al.*, “Catalytic carbonization of polypropylene by the combined catalysis of activated carbon with Ni2O3 into carbon nanotubes and its mechanism,” *Appl. Catal. A Gen.*, vol. 449, pp. 112–120, 2012, doi: 10.1016/j.apcata.2012.09.028.

[55] X. Wen *et al.*, “Nanosized carbon black combined with Ni2O3 as ‘universal’ catalysts for synergistically catalyzing carbonization of polyolefin wastes to synthesize carbon nanotubes and application for supercapacitors,” *Environ. Sci. Technol.*, vol. 48, no. 7, pp. 4048–4055, 2014, doi: 10.1021/es404646e.

[56] J. J. H. B. Sattler, J. Ruiz-Martinez, E. Santillan-Jimenez, and B. M. Weckhuysen, “Catalytic dehydrogenation of light alkanes on metals and metal oxides,” 2014. doi: 10.1021/cr5002436.

[57] F. Yang, M. Wang, D. Zhang, J. Yang, M. Zheng, and Y. Li, “Chirality Pure Carbon Nanotubes: Growth, Sorting, and Characterization,” 2020. doi: 10.1021/acs.chemrev.9b00835.

[58] A. F. Ismail, P. S. Goh, J. C. Tee, S. M. Sanip, and M. Aziz, “A review of purification techniques for carbon nanotubes,” 2008. doi: 10.1142/S1793292008000927.

[59] P. X. Hou, C. Liu, and H. M. Cheng, “Purification of carbon nanotubes,” 2008. doi: 10.1016/j.carbon.2008.09.009.

[60] H. Igarashi, H. Murakami, Y. Murakami, S. Maruyama, and N. Nakashima, “Purification and characterization of zeolite-supported single-walled carbon nanotubes catalytically synthesized from ethanol,” *Chem. Phys. Lett.*, vol. 392, no. 4–6, 2004, doi: 10.1016/j.cplett.2004.05.104.

[61] L. W. Taylor, O. S. Dewey, E. G. Biggers, M. Durán-Chaves, J. F. Khoury, and M. Pasquali, “Purification of carbon nanotubes for dissolution in chlorosulfonic acid,” *Carbon N. Y.*, vol. 228, 2024, doi: 10.1016/j.carbon.2024.119317.

[62] Y. Wang *et al.*, “Minimizing purification-induced defects in single-walled carbon nanotubes gives films with improved conductivity,” *Nano Res.*, vol. 2, no. 11, 2009, doi: 10.1007/s12274-009-9087-7.

[63] P. X. Hou, S. Bai, Q. H. Yang, C. Liu, and H. M. Cheng, “Multi-step purification of carbon nanotubes,” *Carbon N. Y.*, vol. 40, no. 1, 2002, doi: 10.1016/S0008-6223(01)00075-6.

[64] J. C. Acomb, C. Wu, and P. T. Williams, “The use of different metal catalysts for the simultaneous production of carbon nanotubes and hydrogen from pyrolysis of plastic feedstocks,” *Appl. Catal. B*, vol. 180, 2016, doi: 10.1016/j.apcatb.2015.06.054.

[65] J. Gong *et al.*, “Catalytic carbonization of polypropylene by the combined catalysis of activated carbon with Ni2O3 into carbon nanotubes and its mechanism,” *Appl Catal A Gen*, vol. 449, pp. 112–120, 2012, doi: 10.1016/j.apcata.2012.09.028.

[66] D. Yao, Y. Zhang, P. T. Williams, H. Yang, and H. Chen, “Co-production of hydrogen and carbon nanotubes from real-world waste plastics: Influence of catalyst composition and operational parameters,” *Appl Catal B*, vol. 221, 2018, doi: 10.1016/j.apcatb.2017.09.035.

[67] D. Yao, Y. Zhang, P. T. Williams, H. Yang, and H. Chen, “Co-production of hydrogen and carbon nanotubes from real-world waste plastics: Influence of catalyst composition and operational parameters,” *Appl. Catal. B*, vol. 221, 2018, doi: 10.1016/j.apcatb.2017.09.035.

[68] D. Yao and C. H. Wang, “Pyrolysis and in-line catalytic decomposition of polypropylene to carbon nanomaterials and hydrogen over Fe- and Ni-based catalysts,” *Appl. Energy*, vol. 265, 2020, doi: 10.1016/j.apenergy.2020.114819.

[69] J. Wang, B. Shen, M. Lan, D. Kang, and C. Wu, “Carbon nanotubes (CNTs) production from catalytic pyrolysis of waste plastics: The influence of catalyst and reaction pressure,” 2020. doi: 10.1016/j.cattod.2019.01.058.

[70] K. Jagodzińska, P. G. Jönsson, and W. Yang, “Pyrolysis and in-line catalytic decomposition of excavated landfill waste to produce carbon nanotubes and hydrogen over Fe- and Ni-based catalysts – Investigation of the catalyst type and process temperature,” *Chemical Engineering Journal*, vol. 446, 2022, doi: 10.1016/j.cej.2022.136808.

[71] Q. Liu *et al.*, “Investigating the influences of metal-support interaction in Ni[sbnd]Fe catalysts on the quality of carbon nanomaterials from waste polypropylene,” *Fuel Processing Technology*, vol. 236, 2022, doi: 10.1016/j.fuproc.2022.107428.

[72] K. Li, H. Zhang, Y. Zheng, G. Yuan, Q. Jia, and S. Zhang, “Catalytic preparation of carbon nanotubes from waste polyethylene using feni bimetallic nanocatalyst,” *Nanomaterials*, vol. 10, no. 8, 2020, doi: 10.3390/nano10081517.

[73] D. Yao, H. Li, Y. Dai, and C. H. Wang, “Impact of temperature on the activity of Fe-Ni catalysts for pyrolysis and decomposition processing of plastic waste,” *Chemical Engineering Journal*, vol. 408, 2021, doi: 10.1016/j.cej.2020.127268.

[74] N. Cai *et al.*, “Bimetallic carbon nanotube encapsulated Fe-Ni catalysts from fast pyrolysis of waste plastics and their oxygen reduction properties,” *Waste Management*, vol. 109, 2020, doi: 10.1016/j.wasman.2020.05.003.

[75] M. A. Nahil, C. Wu, and P. T. Williams, “Influence of metal addition to Ni-based catalysts for the co-production of carbon nanotubes and hydrogen from the thermal processing of waste polypropylene,” *Fuel Processing Technology*, vol. 130, no. C, 2015, doi: 10.1016/j.fuproc.2014.09.022.

[76] A. A. Aboul-Enein and A. E. Awadallah, “Production of nanostructure carbon materials via non-oxidative thermal degradation of real polypropylene waste plastic using La2O3 supported Ni and Ni–Cu catalysts,” *Polym. Degrad. Stab.*, vol. 167, 2019, doi: 10.1016/j.polymdegradstab.2019.06.015.

[77] S. He, Y. Xu, Y. Zhang, S. Bell, and C. Wu, “Waste plastics recycling for producing high-value carbon nanotubes: Investigation of the influence of Manganese content in Fe-based catalysts,” *J. Hazard. Mater.*, vol. 402, 2021, doi: 10.1016/j.jhazmat.2020.123726.

[78] A. A. Aboul-Enein and A. E. Awadallah, “Production of nanostructured carbon materials using Fe–Mo/MgO catalysts via mild catalytic pyrolysis of polyethylene waste,” *Chemical Engineering Journal*, vol. 354, 2018, doi: 10.1016/j.cej.2018.08.046.

[79] A. A. Aboul-Enein, H. Adel-Rahman, A. M. Haggar, and A. E. Awadallah, “Simple method for synthesis of carbon nanotubes over Ni-Mo/Al2O3 catalyst via pyrolysis of polyethylene waste using a two-stage process,” *Fullerenes Nanotubes and Carbon Nanostructures*, vol. 25, no. 4, 2017, doi: 10.1080/1536383X.2016.1277422.

[80] A. M. Haggar, A. E. Awadallah, A. A. Aboul-Enein, and G. H. Sayed, “Non-oxidative conversion of real low density polyethylene waste into hydrogen and carbon nanomaterials over MgO supported bimetallic Co-Mo catalysts with different total Co-Mo contents,” *Chem. Eng. Sci.*, vol. 247, 2022, doi: 10.1016/j.ces.2021.117092.

[81] H. Dong *et al.*, “Pyrolysis gas from biomass and plastics over X-Mo@MgO (X = Ni, Fe, Co) catalysts into functional carbon nanocomposite: Gas reforming reaction and proper process mechanisms,” *Science of the Total Environment*, vol. 831, 2022, doi: 10.1016/j.scitotenv.2022.154751.

[82] C. Z. Loebick *et al.*, “Effect of manganese addition to the Co-MCM-41 catalyst in the selective synthesis of single wall carbon nanotubes,” *Journal of Physical Chemistry C*, vol. 113, no. 52, 2009, doi: 10.1021/jp908262u.

[83] B. Chen *et al.*, “Tailoring of Fe/MnK-CNTs composite catalysts for the fischer-tropsch synthesis of lower olefins from syngas,” *Ind. Eng. Chem. Res.*, vol. 57, no. 34, 2018, doi: 10.1021/acs.iecr.8b01795.

[84] S. Panic *et al.*, “Molybdenum anchoring effect in Fe–Mo/MgO catalyst for multiwalled carbon nanotube synthesis,” *Reaction Kinetics, Mechanisms and Catalysis*, vol. 122, no. 2, 2017, doi: 10.1007/s11144-017-1291-y.

[85] J. D. Xu, K. T. Zhu, X. F. Weng, W. Z. Weng, C. J. Huang, and H. L. Wan, “Carbon nanotube-supported Fe-Mn nanoparticles: A model catalyst for direct conversion of syngas to lower olefins,” in *Catalysis Today*, 2013. doi: 10.1016/j.cattod.2013.04.018.

[86] Z. Zolfaghari, A. Tavasoli, S. Tabyar, and A. N. Pour, “Enhancement of bimetallic Fe-Mn/CNTs nano catalyst activity and product selectivity using microemulsion technique,” *Journal of Energy Chemistry*, vol. 23, no. 1, 2014, doi: 10.1016/S2095-4956(14)60118-2.

[87] H. U. Modekwe, K. Moothi, M. O. Daramola, and M. A. Mamo, “Corn Cob Char as Catalyst Support for Developing Carbon Nanotubes from Waste Polypropylene Plastics: Comparison of Activation Techniques,” *Polymers (Basel).*, vol. 14, no. 14, 2022, doi: 10.3390/polym14142898.

[88] Q. L. Li, R. Shan, S. X. Wang, H. R. Yuan, and Y. Chen, “Carbon nanotubes production from catalytic pyrolysis of polyethylene over nickel-based catalysts: The influence of support materials,” *Fuel*, vol. 343, 2023, doi: 10.1016/j.fuel.2023.127966.

[89] A. Veksha, A. Giannis, W. Da Oh, and G. Lisak, “Catalytic processing of non-condensable pyrolysis gas from plastics: Effects of calcium supports on nickel-catalyzed decomposition of hydrocarbons and HCl sorption,” *Chem. Eng. Sci.*, vol. 189, 2018, doi: 10.1016/j.ces.2018.06.014.

[90] H. U. Modekwe, M. A. Mamo, K. Moothi, and M. O. Daramola, “Effect of different catalyst supports on the quality, yield and morphology of carbon nanotubes produced from waste polypropylene plastics,” *Catalysts*, vol. 11, no. 6, 2021, doi: 10.3390/catal11060692.

[91] J. Jia, A. Veksha, T. T. Lim, and G. Lisak, “In situ grown metallic nickel from X–Ni (X=La, Mg, Sr) oxides for converting plastics into carbon nanotubes: Influence of metal–support interaction,” *J. Clean. Prod.*, vol. 258, 2020, doi: 10.1016/j.jclepro.2020.120633.

[92] R. Song, B. Li, S. Zhao, and L. Li, “Transferring polypropylene into carbon nanotubes via combustion of PP/zeolites (H-ZSM-5 or H-Beta)/Ni2O3,” *J. Appl. Polym. Sci.*, vol. 112, no. 6, 2009, doi: 10.1002/app.29754.

[93] R. Song, Y. Yang, Jiqing, and B. Li, “Application of aromatization catalyst in synthesis of carbon nanotubes,” *Bulletin of Materials Science*, vol. 35, no. 1, 2012, doi: 10.1007/s12034-011-0250-x.

[94] D. Yao, H. Yang, Q. Hu, Y. Chen, H. Chen, and P. T. Williams, “Carbon nanotubes from post-consumer waste plastics: Investigations into catalyst metal and support material characteristics,” *Appl. Catal. B*, vol. 280, 2021, doi: 10.1016/j.apcatb.2020.119413.

[95] R. X. Yang, K. H. Chuang, and M. Y. Wey, “Carbon nanotube and hydrogen production from waste plastic gasification over Ni/Al-SBA-15 catalysts: Effect of aluminum content,” *RSC Adv.*, vol. 6, no. 47, 2016, doi: 10.1039/c6ra04546d.

[96] M. Crişan *et al.*, “Sol-gel based alumina powders with catalytic applications,” *Appl. Surf. Sci.*, vol. 258, no. 1, 2011, doi: 10.1016/j.apsusc.2011.08.104.

[97] C. S. Cundy and P. A. Cox, “The hydrothermal synthesis of zeolites: Precursors, intermediates and reaction mechanism,” 2005. doi: 10.1016/j.micromeso.2005.02.016.

[98] M. Shamzhy, M. Opanasenko, P. Concepción, and A. Martínez, “New trends in tailoring active sites in zeolite-based catalysts,” 2019. doi: 10.1039/c8cs00887f.

[99] Y. L. H. S. L. Z. Y. W. Y. H. L. M. J. H. A. T. N. M. D. J. Z. L. Z. W. & F. P.-G. Junyan Zhang, “Tuning metal-support interactions in nickel–zeolite catalysts leads to enhanced stability during dry reforming of methane,” *Nat. Commun.*, Oct. 2024.

[100] B. C. Gates, A. Katz, and J. Liu, “Nested Metal Catalysts: Metal Atoms and Clusters Stabilized by Confinement with Accessibility on Supports,” 2023. doi: 10.1021/prechem.2c00011.

[101] L. Shen, X. Zhang, Y. Li, X. Yang, J. Luo, and G. Xu, “Effect of organic additives in catalyst preparation on the growth of single-wall carbon nanotubes prepared by catalyst-assisted chemical vapour deposition,” *Nanotechnology*, vol. 15, no. 3, 2004, doi: 10.1088/0957-4484/15/3/018.

[102] M. O. Kazakov *et al.*, “Comparative study of MWCNT and alumina supported CoMo hydrotreating catalysts prepared with citric acid as chelating agent,” *Catal. Today*, vol. 357, 2020, doi: 10.1016/j.cattod.2019.03.051.

[103] F. M. M. R. A. R. Shahla Karimi, “Development of a novel method to synthesize Ni/SiO2.MgO catalysts using EDTA as a chelating agent for the methane decomposition proces,” *Powder Technol.*, vol. 443, Jul. 2024.

# Chapter 3
# Methodology

This section outlines the methodological approach employed in the thesis. The experimental set-up and catalyst preparation method are explained and justified. The selection of materials used in this work are detailed, particular explaining why based on their molecular structure, the different aluminosilicate supports were selected. The combination of characterisation techniques used to assess both the fresh and used catalysts, as well as the carbon deposits formed during reactions, are detailed. The rationale behind each technique, the underlying theory, and ultimately the relevance to the study are explained.Figure 3.1 presents a schematic overview of the experimental workflow, outlining the key stages in catalyst preparation and CNM synthesis, with the primary inputs, processing steps and analytical techniques summarised.

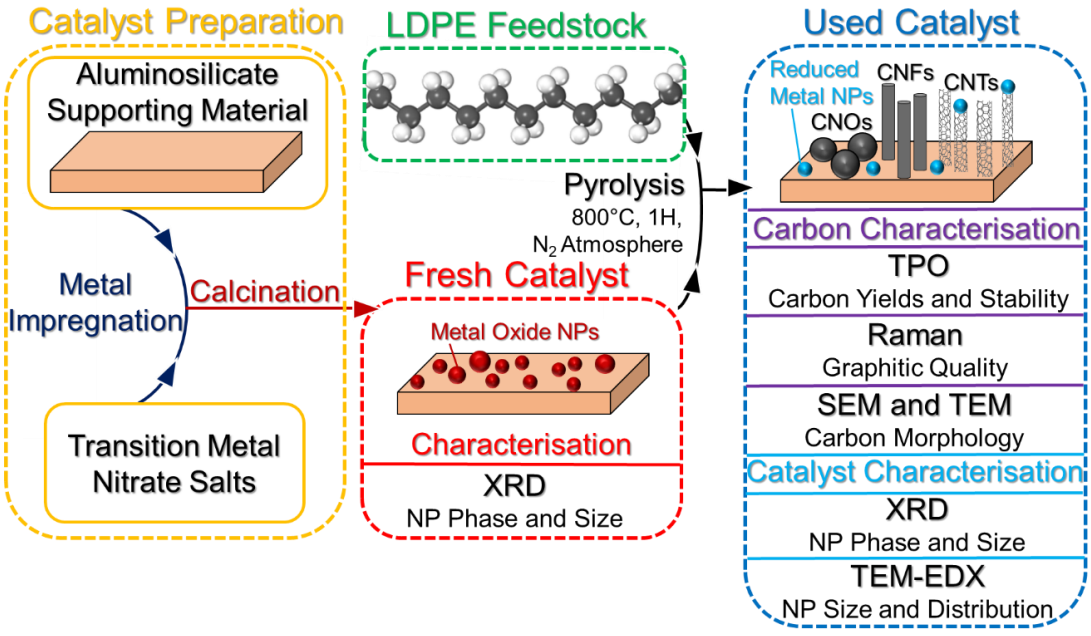


**Figure 3.1.** *Flow chart of the experimental procedure, highlighting primary inputs, processing steps and analytical techniques.*

## 3.1 Catalyst Preparation

### *3.1.1 Effect of Metal Species*

In Chapter 4, each catalyst was prepared using 5 g of α-$Al_2O_3$ support and 5 wt% metal content. The metals were used in their nitrate salt forms: Fe(III) nitrate nonahydrate, Co(II) nitrate hexahydrate and Ni(II) nitrate hexahydrate. These precursors are advantageous due to their solubility in a range of solvents and the ease with which they decompose thermally, releasing active metal ions. The nitrate ligands can be easily burnt off in later stages. The nitrates were dissolved in ethanol, selected for its superior performance in dispersing metal ions compared to other solvents. Support was gradually added to the metal solution under continuous stirring to form a uniform slurry. The mixture was stirred for 2 h and then dried overnight on a hot plate at ~80 °C. Dried samples were calcined at 800 °C for 5 h with a heating rate of 5 °C/min. The calcination temperature was used to match the preparation temperature used for alumina-based catalysts, to allow for better comparation to the most similar catalyst testing in literature which then was used for further catalyst formulation to improve comparability between different supporting materials. Additionally, calcining at the same temperature as CNT growth was intended to stabilise the catalyst structure prior to reaction, minimising further structural evolution during synthesis. The calcinated catalysts were crushed using a mortar and pestle, then sieved to obtain a fine, consistent powder for testing.

### *3.1.2 Effect of Catalyst Supporting Material*

In Chapter 5, the catalysts are prepared in the same way as for Chapter 4, which allows for direct comparation to traditional alumina support. The method differed only by using 5g of different supporting material replacing alumina, namely Y-type Faujasite (FAU), mordenite zeolite (MOR) and Kaolin clay (KAO), and only using the monometallic and FeNi bimetallic. These aluminosilicate materials are selected, with each being classified differently in terms of structural features, therefore allowing for broader role of support morphology to be determined. FAU with a three- dimensional arrangement of interconnected pore channels, and mordenite zeolite (MOR) featuring a one-dimensional parallel liner pore channel architecture. Kaolin clay (KAO) with a flat planar morphology with minimal internal porosity in contrast to the zeolite frameworks. The support materials were all purchased from Sigma Aldrich, with the properties given in this section taken from the data sheet of these purchased materials, and summarised in Table 3.1.

**Table 3.1.** *Material properties of catalyst supports.*

| Material | Structural Type | Si:Al Ratio | Surface Area ($m^2/g$) |
|---|---|---|---|
| Alumina | Non-microporous bulk | N.A. | 6-8 |
| Kaolin (KAO) | Layered sheets | 1:1 | 10-20 |
| Mordenite zeolite (MOR) | One-dimensional pore channels | 13:1 | 425 |
| Y-type Faujasite zeolite (FAU) | Three-dimensional pore network | 5:1 | 900 |

FAU is a highly porous, three-dimensional zeolite with an interconnected channel system, with a surface area of 900 $m^2/g$. Therefore, it is suitable for efficient dispersion of metal species and diffusion of carbon precursors. Additionally, the relatively low Si:Al ratio of 5:1 provides a high density of acid sites for hydrocarbon cracking. MOR features a one-dimensional parallel liner pore channel architecture, with the MOR used here having a surface area of 425 $m^2/g$ and a Si:Al ratio of 13:1. Although this is a reduction from the FAU, reducing precursor cracking ability and diffusion. Although, this ordered linear structure that imposes geometric constraints on the molecular diffusion of metal species particularly relevant when forming surface NPs. has the potential to impart uniformity to the metal NP, and thus carbon product. The flat morphology of KAO provides a continuous and uniform surface for the dispersion of metal NPs, allowing for highly accessible catalytic sites. This promotes surface driven reactions as opposed to the bulk diffusion of the zeolites. Low acid site concentration in comparison to zeolite may reduce the hydrocarbon cracking ability.

### *3.1.3 Effect of Preparation Method Modification*

In Chapter 6, the influence of various modifications to the Co/MOR catalyst are tested. The first variation involved a catalyst similar to the previously prepared Co/MOR sample, but calcined at a lower temperature of 550 °C, designated as $Co/MOR_{550}$. This lower temperature was selected to better preserve the zeolite framework, potentially enhancing the catalyst's cracking activity. All subsequent catalysts discussed in this section were also calcined at 550 °C.

The effect of metal complexing agent was tested by replacing the ethanol solvent with a mixed solvent system of water and ethylenediamine (EDA) in a 10:1 volume ratio, with the catalyst synthesised by this method designated as $Co/MOR_{EDA}$. A total of 20

mL of this solution was prepared, and cobalt nitrate was added to achieve an EDA:Co molar ratio of 3:1, ensuring complete complexation of $Co^{2+}$ ions prior to impregnation. The MOR was then added to this solution, mixed and dried in the same way as previously.

The effect of hydrothermal synthesis of a zeolite in the presence of metal solution was tested, with the resulting catalyst designated Co@MOR. A synthesis gel with the molar composition 6 $Na_2O$:$Al_2O_3$:30 $SiO_2$:780 $H_2O$, commonly used for MOR-type zeolites, was prepared. Initially, 2.85 g of NaOH was dissolved in 20 mL of deionized water, followed by the addition and dissolution of 1.16 g $NaAlO_2$. In parallel, a cobalt solution was prepared by dissolving 2.04 g of cobalt(II) nitrate hexahydrate in 80 mL of water with EDA, maintaining a 3:1 EDA to Co molar ratio to ensure full complex formation. This solution was stirred magnetically for 30 minutes before being added to the basic alumina solution. Next, 12.8 g of fumed silica was added under continuous stirring to form a homogeneous gel. MOR seeds from the purchased zeolite were added at 5 %wt compared to the total expected zeolite weight. The resulting gel was transferred into a 100 mL Teflon-lined autoclave and subjected to hydrothermal synthesis with a ramp rate 1°C/min used to reach 170°C for 24 hours. After synthesis, the product was washed three times with 100 mL of deionised water, using filtration paper to collect solids after each wash. The final product was dried overnight at approximately 80°C on a hot plate.

The CoMo/MOR and CoMn/MOR catalysts were prepared using the same procedure as $Co/MOR_{EDA}$, with the addition of Molybdenum trioxide and Manganese (II) nitrate hydrate to achieve Co:Mo and Co:Mn molar ratios of 1:1 and 2:1, respectively.

## 3.2 CNM Growth

### *3.2.1 Feedstock Selection*

The polyolefin feedstock selected for this study was LDPE, due to its simplified molecular structure consisting solely of carbon and hydrogen atoms in a linear backbone, and a degree of chain branching intermediate for polyolefins. This makes it mechanistically straightforward and a representative model compound for polyolefins in general. The LDPE feedstock, with a density of 0.92g/ml and average molecular weight ~4000 was purchased from Sigma-Aldrich.

### 3.2.2 Reactor Set-up

The CNM synthesis was performed in a quartz tube reactor in batch set up, with total length 0.5 m and internal diameter 25 mm. A diagram of the reactor is shown in Figure 3.2. In each experiment, 0.5 g of LDPE was loaded into a quartz boat, with an equal weight of catalyst layered on top. Although, this ratio is not representative of industrial practice, where catalyst loadings are substantially lower, the ratio was selected for mechanistic clarity rather than process optimisation or direct scale-up. High carbon flux in a one-stage plastic pyrolysis system can rapidly oversaturate metal nanoparticles, leading to encapsulation or carbide formation and premature deactivation. Increasing catalyst loading reduces the chance of oversaturation, and helps to ensure that performance differences reflect intrinsic metal properties rather than catalyst converging on similar deactivated behaviours. This ratio therefore serves a proof-of-concept used for catalytic comparation, and can be optimised in future work. The quartz boat was then placed in the centre of the tube reactor. The tube reactor was then filled with nitrogen at for 20 minutes to ensure a fully inert atmosphere. A heating rate of 20 °C/min was used with a dwell time of 1h at the final temperature of 800 °C.

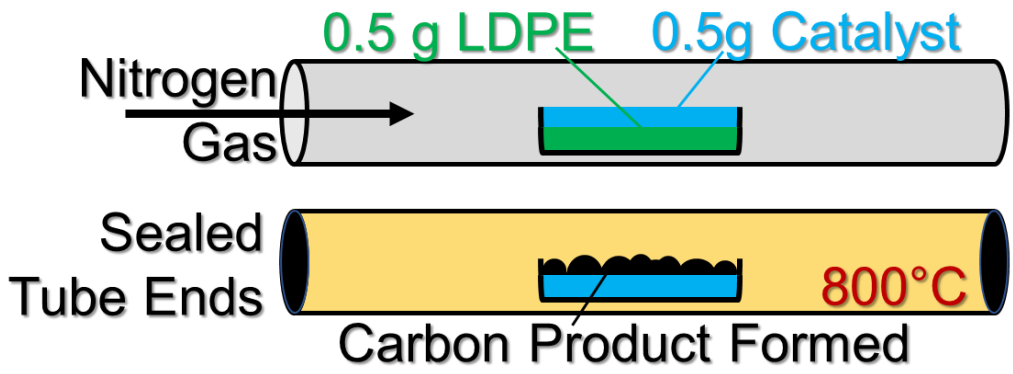


**Figure 3.2.** *Schematic of the reactor set-up used to produce the carbon materials*

### 3.2.3 Error Estimation

The monometallic catalysts using the alumina support were repeated three times, allowing for the reproducibility of the experiment to be evaluated. This was used to gives an estimate for the variability between runs in this system, since due to time constraints, the other catalysts were only ran once. The relative standard deviation (RSD) was calculated by:

$$RSD = \frac{\sigma}{\bar{x}} \tag{3.1}$$

Where $\bar{x}$ is the sample mean and σ is the sample standard deviation, which itself is calculated by:

$$\sigma = \sqrt{\frac{\sum(x_i - \bar{x})^2}{n-1}} \tag{3.2}$$

Where n is the total number of samples and $x_i$ is the conversion value for each individual run.

## 3.3 Analysis

### *3.3.1 X-ray Diffraction Analysis*

X-ray diffraction (XRD) is a non-destructive analytical technique used to determine the crystal structure of materials. Incident X-rays are scattered by parallel planes of atoms within a crystalline lattice. When constructive interference occurs, it corresponds to specific lattice spacings. By scanning across a range of diffraction angles, a composite diffraction pattern is obtained, reflecting the atomic plane spacings characteristic of the crystalline phases present.

XRD analysis was carried out using a Rigaku Miniflex diffractometer, with data processed using Rigaku SmartLab software. This technique was employed to identify crystalline phases in the fresh catalysts, including surface oxides, mixed bimetallic oxides, and metal-support aluminate phases. For the used catalysts, XRD was applied to assess whether metal species had been fully reduced during CNT synthesis, forming active metallic nanoparticles (NPs).

Peak broadening effects in the diffraction patterns can be used to estimate the NP diameters, with two methods used depending on the material. Both methods were implemented within the Rigaku SmartLab software. The Scherrer approximation uses a single peak for the diameter calculation:

$$\mathrm{D} = \frac{\mathrm{K}\lambda}{\beta\cos\theta} \tag{3.3}$$

D is the average crystallite size, K a shape factor (0.9 for roughly spherical NPs), λ is the X-ray wavelength, β is the full width at half maximum intensity of the diffraction peak and θ is the angle of the diffraction peak.

The Halder-Wagner method expands on Scherrer by recognising that total peak broadening contains contributions from both crystallite size and microstrain, and by

analysing multiple diffraction peaks across the scan range the influence if these two effects can be determined. The peak broadening effects are given by:

$$\beta_{strain} = 4\epsilon\, tan\theta \tag{3.4}$$

$$\beta_{size} = \frac{K\lambda}{D\cos\theta} \tag{3.5}$$

ε represents the lattice microstrain.

Which can be combined, and then simplified to give a linear equation:

$$\beta^2 = \beta_{size}\beta + (\beta_{\mathrm{Strain}})^2 \tag{3.6}$$

A plot constructed from several diffraction peaks therefore allows both parameters to be determined, with the slope corresponding to crystallite size and the intercept representing microstrain. Providing there are at least three well-resolved diffraction peaks available, the Halder-Wagner method can provide significantly better results compared to the Scherrer approximation.

In this work, the Scherrer approximation was used to estimate the NP sizes for pure metallic species, since one clear peak with limited secondary peaks and is relatively low intrinsic lattice strain in pure metal particles due to a homogenious crystalline bulk. Whereas, for oxide NPs the Halder-Wagner method was used due to the larger effects of microstrain since due to the presence of non-stoichiometry or mixed oxidation states in the NPs, with multiple clear peaks found in most cases.

Comparisons between fresh and spent catalysts allowed for evaluation of NP dispersion and sintering resistance. While the use of different in size estimation methods may hinder direct comparability, the results are still valuable in identifying trends, particularly in determining which catalysts exhibit improved resistance to sintering under CNT growth conditions.

### *3.3.2 Thermogravimetric Analysis*

The conversion and structural classification of carbonaceous products were determined using thermogravimetric analysis (TGA) under an air atmosphere using a TA Instruments TGA 5500. This enabled temperature programmed oxidation (TPO) to occur, which involves measuring the mass loss due to oxidation of a material over a range of temperatures. A heating rate of 10 °C per minute was applied up to a maximum temperature of 800 °C, at which carbon oxidation is was complete with no further mass loss observed. The dry mass of the used catalyst was taken as the mass

at 300 °C, which allowed for all microporous water to be evaporated without any carbon oxidation occurring. The carbon conversion was defined as the percentage of carbon in the PE feedstock which was converted to carbon on the used catalyst, calculate by

$$Carbon\ conversion = \frac{m_{C,Cat}}{m_{C,PE}} \times 100\% = \frac{m_{Cat,300°C} - m_{Cat,800°C}}{0.86 m_{PE}} \times 100\% \qquad (3.7)$$

Where $m_{C,cat}$ is the mass of carbon found to be deposited on the catalyst and $m_{C,cat}$ is the mass of carbon present in the PE feedstock, $m_{Cat,300°C}$ is the mass of the catalyst at 300 °C, $m_{Cat,800°C}$ is the mass of the catalyst at 800 °C and $m_{PE}$ is the total PE feedstock mass.

TPO provides a more accurate assessment of carbon conversion compared to simple mass balance methods, where sample mass is measured before and after reaction. The results from traditional weighing approaches can be distorted factors such as the mass loss from reduction of metal oxides and moisture content, particularly in porous, high-surface-area supports. TPO, in contrast, enables differentiation of these effects by correlating mass loss with specific temperature ranges. Carbon oxidation typically occurs between 500°C and 700°C, clearly separable from the lower-temperature evaporation of water. Furthermore, the oxidation temperature of carbon is influenced by its morphology and defect structure. Filamentous carbon tends to oxidize at higher temperatures than amorphous carbon, while defective graphitic structures oxidize more readily. However, additional factors may influence oxidation behaviour, such as the presence of certain metal catalysts can promote redox reactions and catalyse carbon oxidation at reduced temperatures. Thus, this technique not only quantifies carbon conversion with greater specificity but also provides indirect insight into carbon structure and quality based on oxidation profiles.

### *3.3.3 Raman Spectroscopy*

Raman spectroscopy was conducted using a LabRAM HR system equipped with a Ventus 532 nm laser to assess the quality of the CNMs. This is achieved by comparation of the intensities of different Raman bands. The G band corresponds to vibrational mode of $sp^2$-hybridised carbon atoms, indicative of graphitic order. Whereas, the D band arises from the presence of $sp^3$-hybridized carbon and structural defects. The intensity ratio of the D and G bands is used to quantify the degree of disorder within graphic lattice. The 2D band provides information on the number of graphene layers and the stacking order of graphitic sheets, with sharper and more

intense peaks associated with fewer layers and higher crystallinity. Where overlapping of Raman bands occurred, particularly due to wide D bands, peak deconvolution was performed to quantify individual contributions accurately. Additionally, Raman spectroscopy was applied to selected Co-containing catalysts to distinguish between $CoAl_2O_4$ and $Co_3O_4$ phases. These cobalt species exhibit similar lattice parameters, making them difficult to differentiate by XRD. Raman, being sensitive to their distinct vibrational modes, offers a complementary technique for phase identification.

### *3.3.4 Scanning Electron Microscopy*

Scanning Electron Microscopy (SEM) analysis was performed using a Tescan Clara ultra-high-resolution microscope. Samples were sputter-coated with Au-Pd using a Polaron SC7640 to enhance image clarity and conductivity. Images were obtained at magnifications up to 25,000x. This provided key morphological information, allowing identification of carbon forms such as filamentous, spherical, or irregular structures. The size, density, and distribution of these features gave insight into catalytic activity and uniformity. Morphologies ranging from highly ordered to chaotic could be linked to defect densities observed from Raman analysis.

### *3.3.5 Transmission Electron Microscopy with Energy Dispersive X-ray*

Transmission Electron Microscopy (TEM) was employed alongside SEM to provide complementary insights into the morphology of the carbon deposits. High-resolution imaging was conducted using a FEI Titan Themis microscope, which allowed for over 1,000,000x magnification and the integration of Energy Dispersive X-ray (EDX) for elemental analysis. Sample preparation involved an initial mechanical thinning using a Gatan dimple grinder, followed by final thinning using a Gatan Precision Ion Polishing System to achieve electron transparency.

TEM provides a complementary imaging technique to SEM, enabling detailed visualisation of the internal structure of carbon materials. This allowed for the differentiation between CNTs and CNFs due to the characteristic hollow cores of CNTs appearing as low-density regions. TEM also revealed the arrangement, stacking order, and crystallinity of graphitic layers, as well as the presence of disordered or amorphous carbon regions. Beyond carbon characterisation, TEM-EDX was used to assess the size, dispersion and distribution of metal NPs. This can complement the average NP sizes found by XRD, and give further insight into the distribution of NPs. In bimetallic systems, TEM-EDX can determine whether alloyed

NPs have been formed, and assesses the effect of any phase separation. Furthermore, by examining the location of metal NPs in used catalysts, it was also possible to infer if tip or base growth modes have occurred.

# Chapter 4
# Effect of Metal Species

The selection of metal species plays a critical role in the catalytic conversion of polyolefins to carbon nanomaterials (CNMs). In this chapter, the influence of active metal composition on catalyst performance is evaluated, with Monometallic and bimetallic configurations of Fe, Co, and Ni tested. Alumina is used as the benchmark support due to its widespread application and well-characterised interactions with transition metals, allowing performance differences to be more directly attributed to the intrinsic properties of the metal species. The catalyst characterisation was carried out by assessing the size and distribution of metal nanoparticles (NPs) on both fresh and spent catalysts to assist in explaining variations in catalytic performance. Catalyst effectiveness is further evaluated through several metrics including carbon conversion, carbon product structure, carbon quality and product stability. Carbon conversion is quantified by measuring the mass of carbon deposited on the spent catalysts. The structure of the resulting carbon is analysed in terms of CNM type and over morphology, as well as internal carbon arrangement, evaluated in terms of the presence and characteristics of graphitic layering. Carbon quality is assessed by quantifying the defect density within the hexagonal carbon lattice, offering insight into crystallinity and degree of graphitisation. The thermal stability of the carbon products under combustion conditions provides complementary evidence for the structural integrity and ordering of the carbon nanomaterials.

## 4.1 Catalyst Characterisation

The structural characteristics of the catalysts in both fresh and used form were characterised using a combination of analytical techniques. XRD was performed to identify the crystalline metallic phases and to estimate the average nanoparticle sizes. To complement the XRD-derived size estimates and provide insight into particle dispersion and morphology, TEM-EDX was carried out on the used catalysts. This enabled direct imaging of the metal nanoparticles, revealing their distribution and size range. For cobalt-containing catalysts, phase identification via XRD was complicated by the similarity of $Co_3O_4$ and $CoAl_2O_4$ lattice parameters, with Raman spectroscopy employed to resolve these ambiguities. Across all samples, the alumina support was confirmed to be the Corundum phase (alpha-$Al_2O_3$), with characteristic primary peaks at around 25.6°, 35.2°, 37.8°, 43.4°, 52.5°, 57.5°, 61.3°, 66.5° and 68.1° displayed for all fresh and used catalysts [1], and shown for a reference in Figure 4.1.

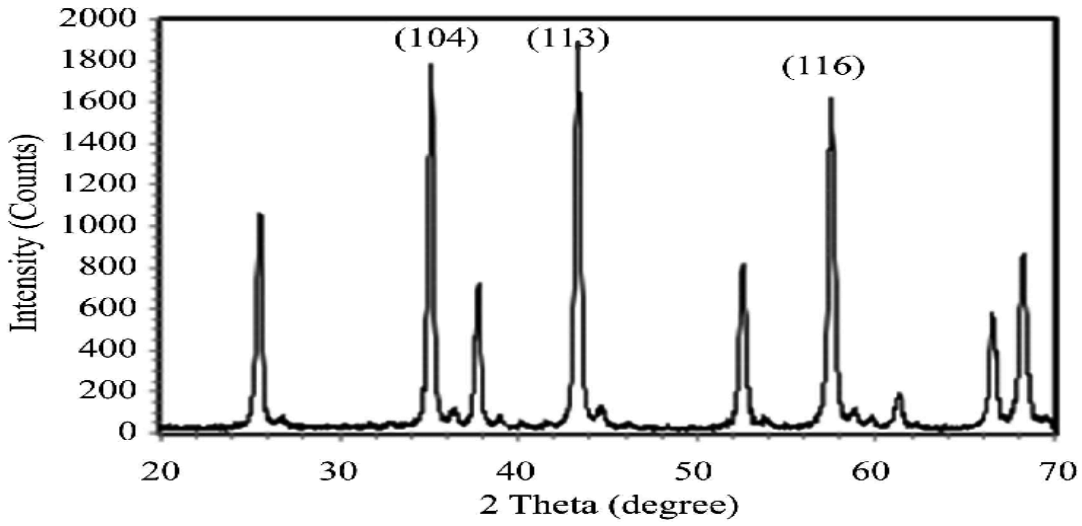


**Figure 4.1.** *Reference XRD Spectra of Corundum phase alumina [1].*

### *4.1.1 Iron*

Figure 4.2 shows that the $Fe/Al_2O_3$ catalyst displayed prominent XRD peaks characteristic of hematite ($\alpha$-$Fe_2O_3$), with primary peaks at 33.1°, 35.6°, and 54.1° 2θ, corresponding to the (104), (110) and (116) planes respectively [2]. The XRD pattern of the used catalyst shows the disappearance of peaks associated with hematite and the appearance of new reflections consistent with metallic $Fe^0$, with the most prominent peak observed at approximately 44.7° corresponding to body-centred cubic (bcc) iron [3]. This confirms that full reduction of the oxide species occurred during the reaction.

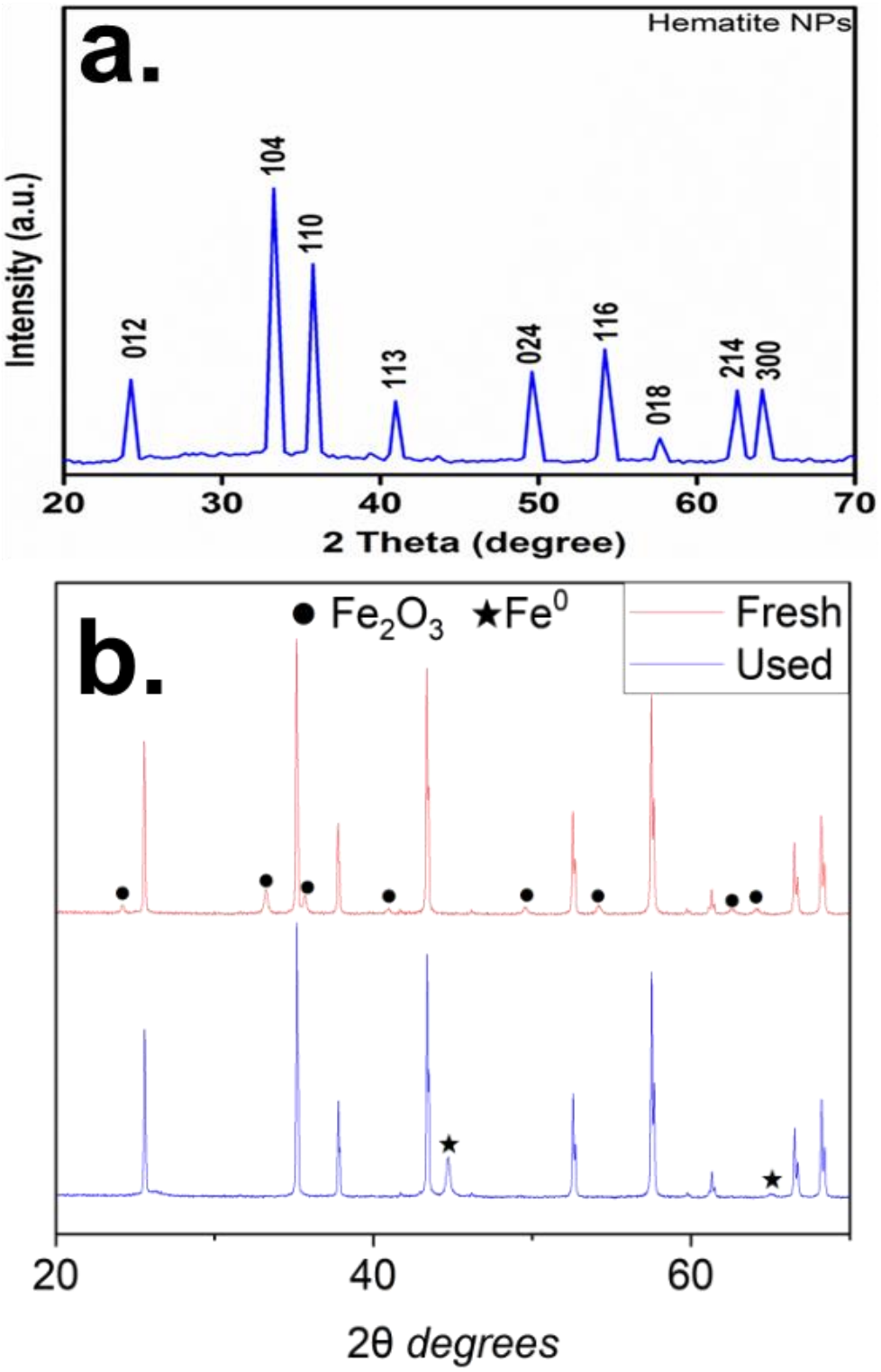


**Figure 4.2.** *Characterisation of the $Fe/Al_2O_3$ catalyst showing (a) Reference XRD pattern for $Fe_2O_3$ [2] and (b) XRD patterns of fresh and used catalysts with the Fe-phases identified.*

Figure 4.3 shows the average nanoparticle (NP) diameter estimated from XRD of the fresh Fe/$Al_2O_3$ catalyst was 44.2 nm, suggesting moderate agglomeration during the calcination process. The used catalysts estimated NP size decreased to 33.0 nm, consistent with expected size decrease due to oxygen loss during reduction. However, analysis of the used catalyst by TEM-EDX revealed significant heterogeneity in particle size and dispersion. While smaller Fe nanoparticles were present, large agglomerates up to ~200 nm were also observed, resulting in poor overall dispersion. Such agglomeration can be attributed to the weak interaction between iron and the $Al_2O_3$ support, coupled with the high surface mobility of Fe at elevated temperatures [4]. These findings highlight the limitations of relying solely on XRD for average particle size estimation, especially based off single peaks, which may obscure the presence of larger, non-uniformly distributed particles. Although, XRD remains suited for identifying relative trends or comparing similar materials.

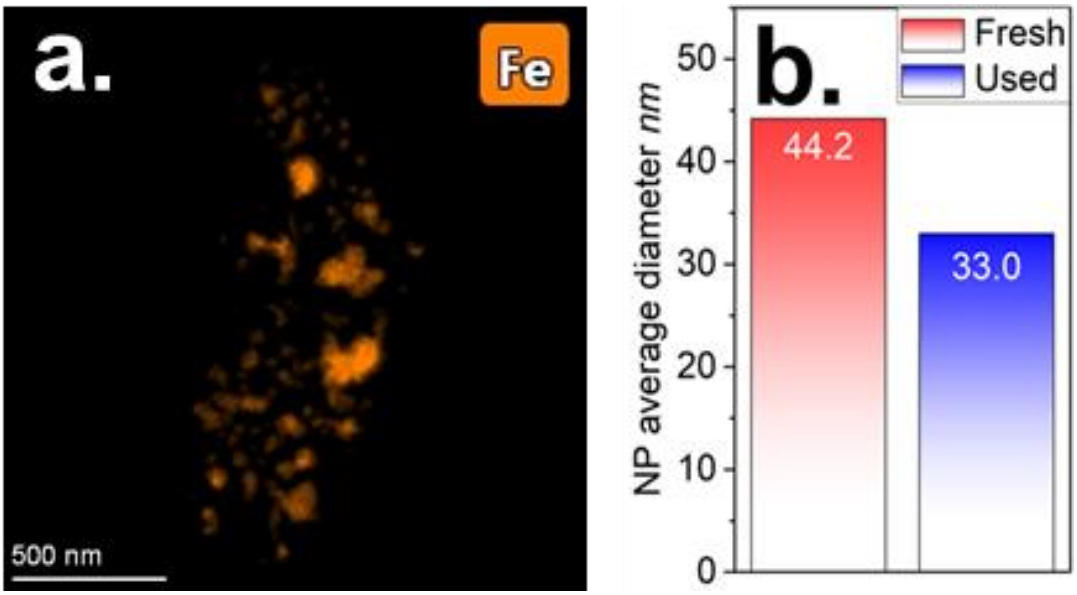


**Figure 4.3.** *Characterisation of the Fe/$Al_2O_3$ catalyst showing (a) TEM-EDX image of the Fe in the used catalyst and (b) the average NP diameters estimated from XRD.*

### *4.1.2 Cobalt*

Figure 4.4 shows the phase identification results for the Co/$Al_2O_3$ fresh and used catalysts. The XRD pattern displays distinct XRD reflections at 31.3°, 36.8°, 59.3° and 65.2° 2θ, corresponding to the (220), (311), (511) and (440) planes of $Co_3O_4$ or $CoAl_2O_4$ [5]. The presence of $Co_3O_4$ was confirmed by Raman spectroscopy, with the most prominent and sharpest band at ~690 $cm^{-1}$ and the expected secondary bands at 190 $cm^{-1}$, 490 $cm^{-1}$ and 520 $cm^{-1}$ [6] [7] [8]. In contrast, $CoAl_2O_4$ would typically display the strongest band at 190$cm^{-1}$ or 520 $cm^{-1}$, thus confirming limited $CoAl_2O_4$

formation. The post-reduction XRD pattern indicates a transformation to metallic cobalt phases, with the main peak at 44.2° corresponding to hexagonal close-packed (hcp) α-$Co^0$ phase.

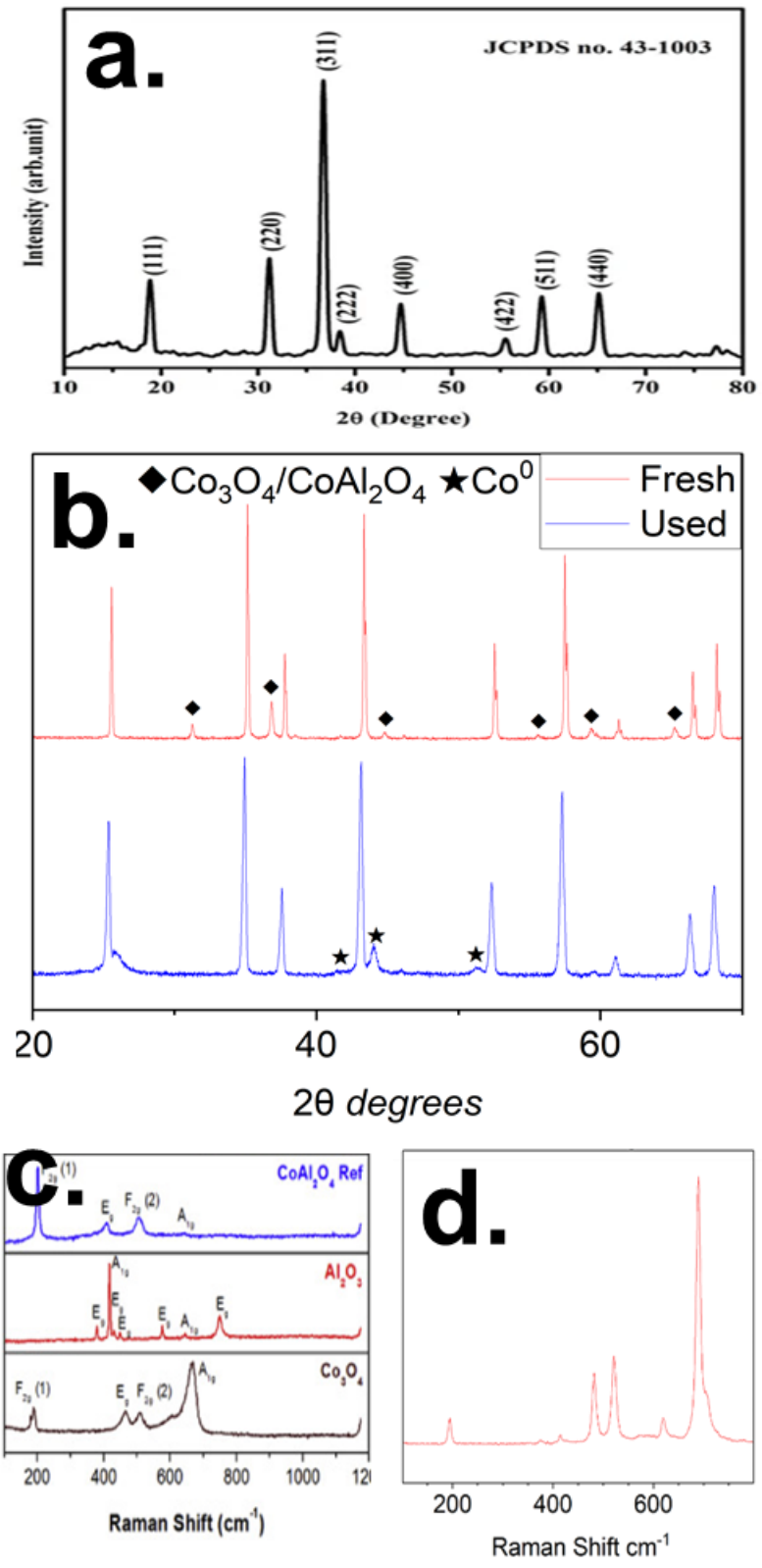


**Figure 4.4.** *Characterisation of the Co/Al₂O₃ catalyst showing (a) Reference XRD pattern for Co₃O₄ [5] (b) XRD patterns of fresh and used catalysts with the Co-phases identified (c) Reference Raman spectra for Cobalt and Alumina species [6] and (d) Raman spectra for the fresh Co/Al₂O₃ catalyst.*

Figure 4.5 shows that the average $Co_3O_4$ nanoparticle diameter in the fresh $Co/Al_2O_3$ catalyst was 73 nm, indicative of substantial agglomeration in the oxide form, with the average NP size post reduction found to be 24.4 nm. This is supported by the TEM-EDX which shows finely dispersed cobalt NPs predominantly under 20 nm, with only a limited number of larger agglomerates up to 60 nm in diameter. The large difference in $Co_3O_4$ and $Co^0$ NPs cannot fully be explained by the loss of lattice oxygen Instead, this observation is consistent with NP fragmentation occurring during the reduction process. While such fragmentation is typically rare under standard $H_2$ reduction, it has been reported under non-conventional conditions.

These include repeated oxidation-reduction cycles and reduction and presence of hydrocarbons have been found to cause this phenonium during $Co_3O_4$ reduction [9] [10]. These conditions are believed to promote the formation of unstable intermediate oxide phases. When coupled with strong metal-support interaction (MSI) between Co and $Al_2O_3$, which is likely stronger than the MSI in Fe-based catalyst, these intermediate phases can anchor to the support surface and fragment into smaller metallic domains [10]. In this process, he presence of mixed hydrocarbon gases during reduction likely facilitated this mechanism, contributing to the unexpectedly fine dispersion of cobalt nanoparticles observed in the used catalyst.

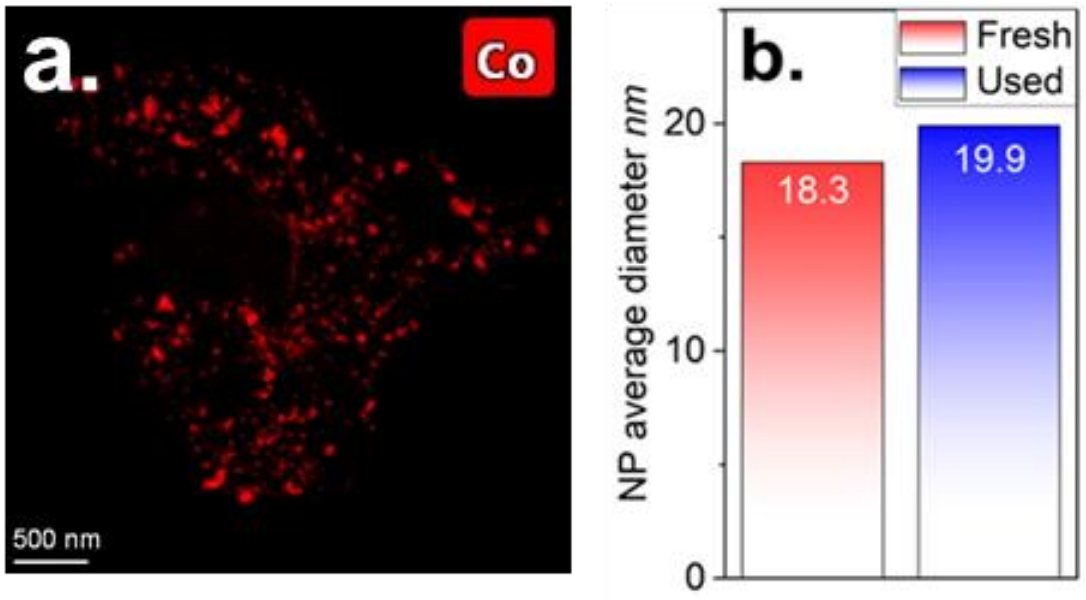


**Figure 4.5.** *Characterisation of the $Co/Al_2O_3$ catalyst showing (a) TEM-EDX image of the Co in the used catalyst and (b) the average NP diameters estimated from XRD.*

### *4.1.3 Nickel*

The phase identification results for the $Ni/Al_2O_3$ catalyst are shown in Figure 4.6 It can be seen from the XRD pattern for the $Ni/Al_2O_3$ catalyst that the main XRD peaks are at 37.2° and 62.9° 2θ, corresponding to the (111), and (220) planes of cubic NiO, respectively [11] with a peak at 43.3° corresponding to the (200) plane heavily overlapping with the $Al_2O_3$ pattern.

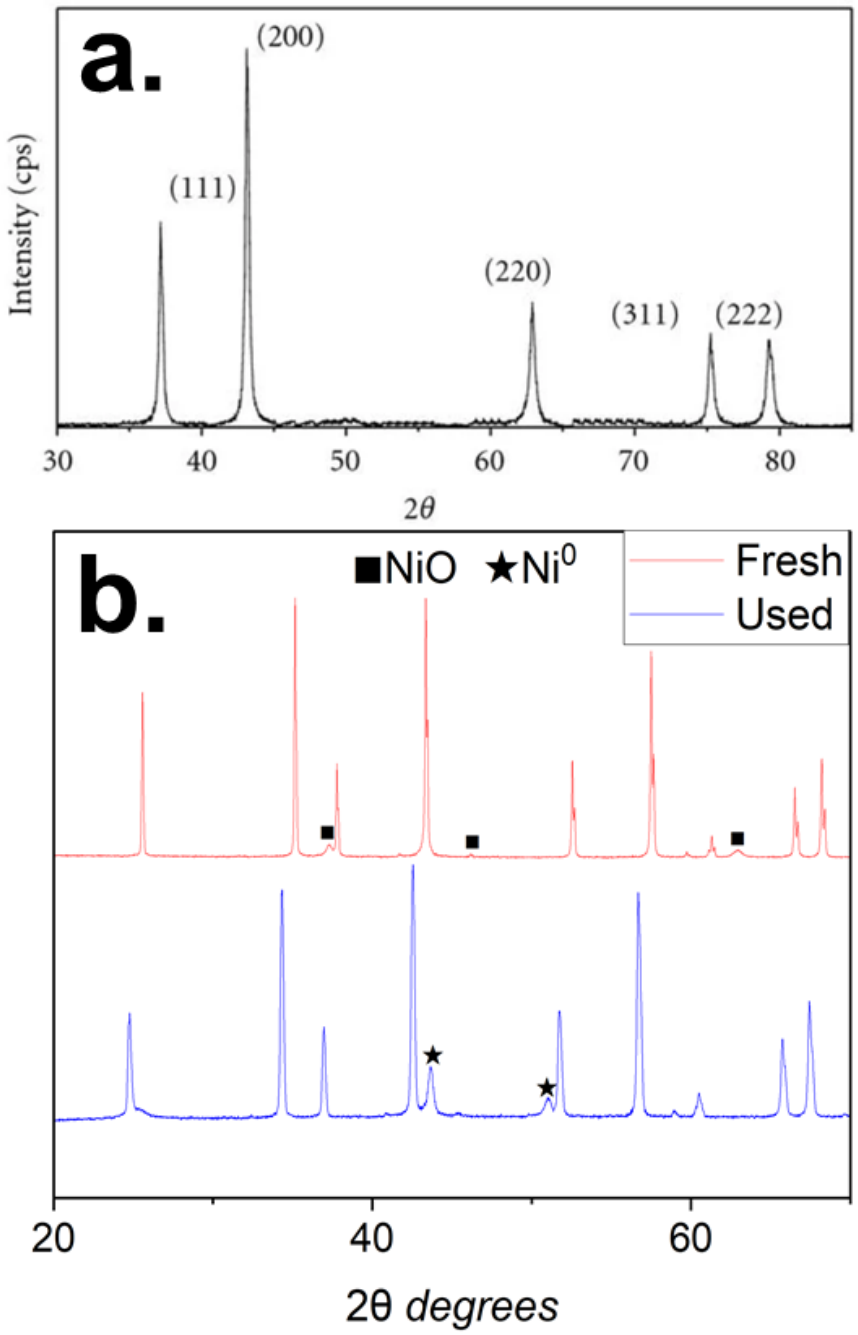


**Figure 4.6.** *Characterisation of the Ni/$Al_2O_3$ catalyst showing (a) Reference XRD pattern for NiO [11] and (b) XRD patterns of fresh and used catalysts with the Ni-phases identified.*

Figure 4.7 shows that the estimated NiO NP diameter in the fresh state was approximately 16.0 nm, suggesting a high degree of dispersion and minimal agglomeration. However, upon reduction, the average NP diameter increased to about 23.7 nm, indicating moderate sintering during thermal treatment. TEM-EDX

imaging showed moderately well-dispersed NPs, with a reasonable population below ~50 nm but with larger agglomerations up to 120 nm observed.

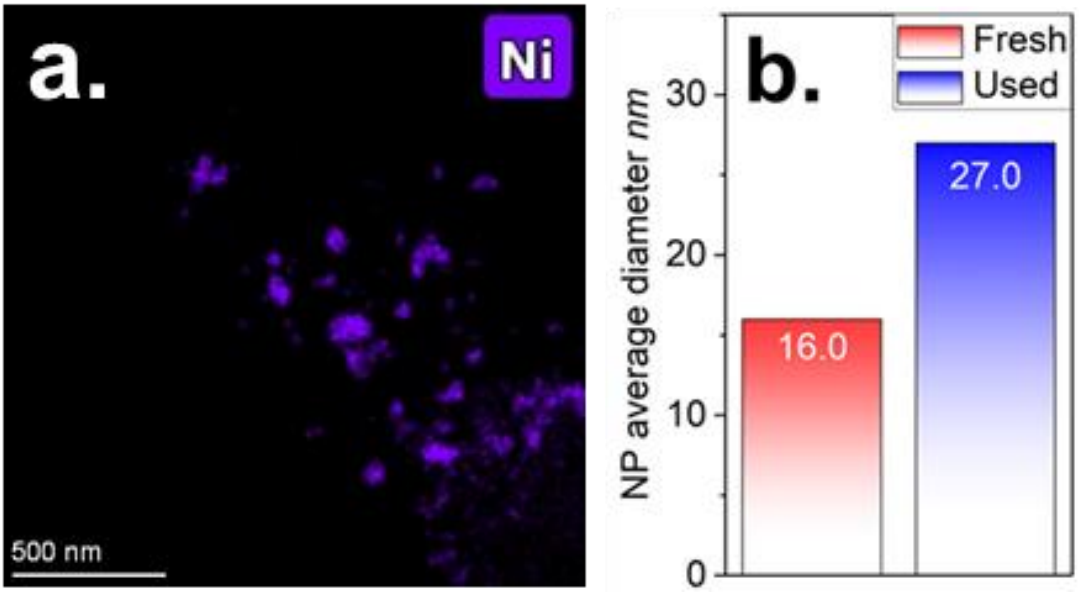


**Figure 4.7.** *Characterisation of the Ni/$Al_2O_3$ catalyst showing (a) TEM-EDX image of the Ni in the used catalyst and (b) the average NP diameters estimated from XRD.*

### *4.1.4 Iron-Cobalt Bimetallic*

Figure 4.8 presents the characterisation results for the fresh and used $FeCo/Al_2O_3$ catalyst. The XRD patterns of the fresh catalyst reveal peaks attributable to ferrite spinel phases such as $Fe_3O_4$ or mixed spinels like $Fe_2CoO_4$ and $Co_2FeO_4$. The incorporation of cobalt likely shifts the preferred iron phase from $Fe_2O_3$, typically observed in the monometallic $Fe/Al_2O_3$ catalyst, to the formation of $CoFe_2O_4$ spinel.

Raman spectroscopy supports this observation, displaying broad bands at approximately 310, 470, and 690 $cm^{-1}$, which is characteristic of cobalt ferrites spinels [12] and the absence of a strong band at 540 $cm^{-1}$, typically associated with $Fe_3O_4$ [13] [14] [15]. A weak band at ~410 $cm^{-1}$ may indicate either a contribution from $Al_2O_3$, which is usually weak, or the formation of $CoAl_2O_4$. The disordered appearance of the Raman spectrum suggests a significant degree of structural disorder and the coexistence of mixed, non-uniform crystalline phases. Upon reduction, XRD analysis confirmed the presence of metallic FeCo nanoparticles.

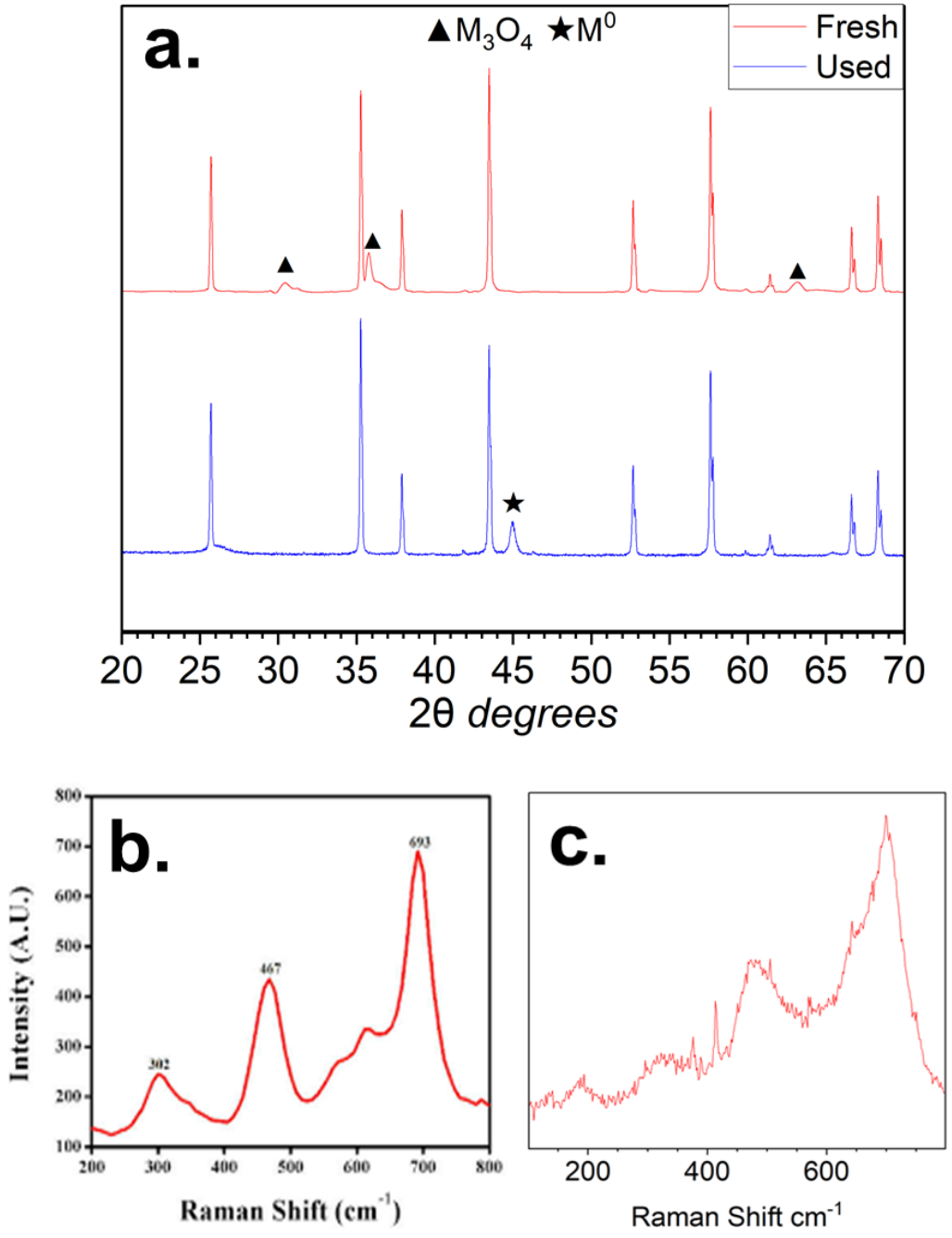


**Figure 4.8.** *Characterisation of the FeCo/$Al_2O_3$ catalyst showing (a) XRD patterns of fresh and used catalysts with the metallic phases identified, (b) Reference Raman spectra for cobalt ferrite species [12] and (d) Raman spectra for the fresh FeCo/$Al_2O_3$ catalyst.*

Figure 4.9 shows that the metallic FeCo NPs exhibited an average crystallite size of 26.3 nm, with TEM-EDX imaging showed a high degree of overlap between Fe and Co signals, indicating successful formation of bimetallic NPs. However, the reduced catalyst showed fewer overall particles and poor dispersion, with large NP up to 100 nm in diameter. Therefore, similar to Fe-based systems, the FeCo catalyst exhibited

sintering, although the presence of Co may have mitigated the extent of sintering to some degree.

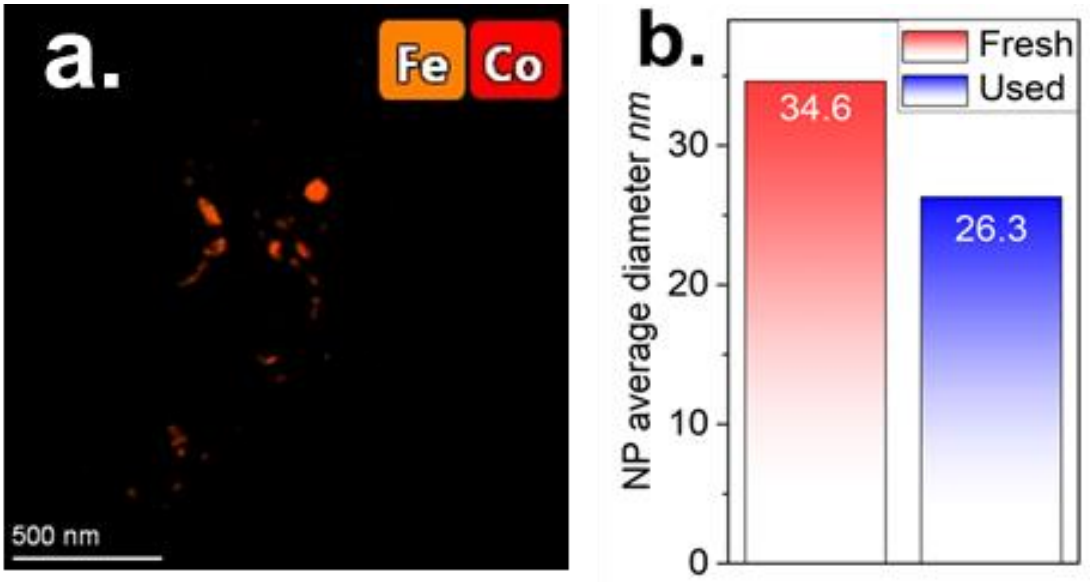


**Figure 4.9.** *Characterisation of the FeCo/$Al_2O_3$ catalyst showing (a) TEM-EDX image of the Fe and Co in the used catalyst and (b) the average NP diameters estimated from XRD.*

### *4.1.5 Iron-Nickel Bimetallic*

Figure 4.10 shows the FeNi/$Al_2O_3$ characterisation, which showed features typical of a ferrite spinel phase, likely $NiFe_2O_4$, with principal XRD peaks at 30.3°, 35.7°, and 62.7° 2θ, indexed to the (220), (311), and (440) planes [16].

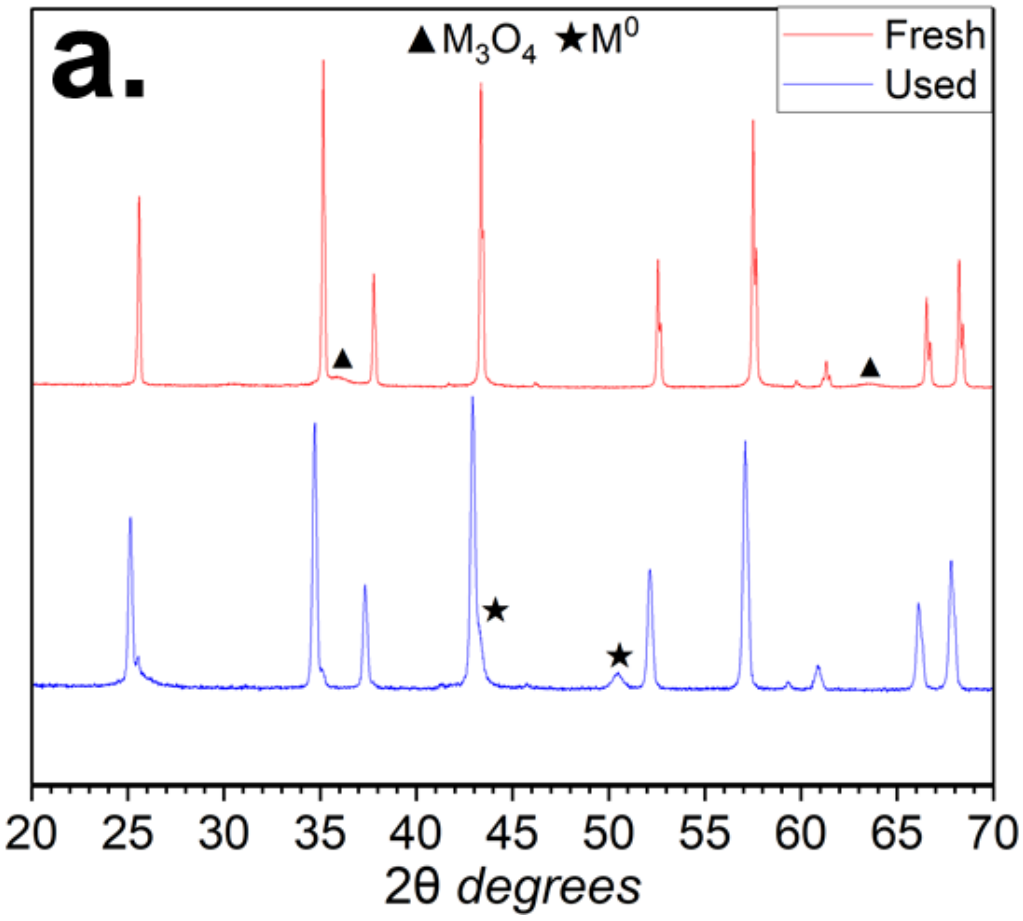


**Figure 4.10.** *Characterisation of the FeNi/$Al_2O_3$ catalyst showing the XRD patterns of fresh and used catalysts with the metallic phases identified.*

Figure 4.11 shows the average NP diameter calculated from peak broadening was 7.6 nm, indicating enhanced thermal stability likely due to the formation of alloyed oxide species. Following reaction, the nanoparticle size increased significantly to 30.8 nm, indicating a considerable degree of sintering. TEM-EDX analysis revealed a high degree of overlap between iron and nickel, confirming the formation of bimetallic alloy nanoparticles. The catalyst exhibited a wide particle size distribution, with many well-dispersed nanoparticles below 40 nm and a secondary population of larger particles in the 70 to 100 nm range.

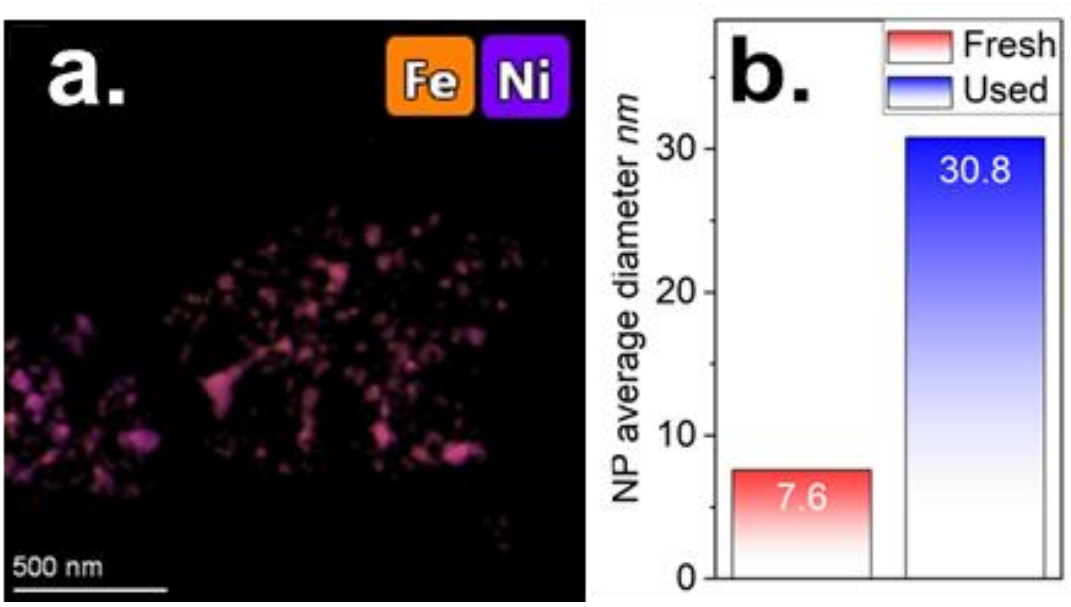


**Figure 4.11.** *Characterisation of the FeNi/$Al_2O_3$ catalyst showing (a) TEM-EDX image of the Fe and Ni in the used catalyst and (b) the average NP diameters estimated from XRD.*

### *4.1.6 Cobalt-Nickel Bimetallic*

Figure 4.12 presents the phase identification of the CoNi/Al2O3 catalyst. The XRD pattern of the fresh catalyst revealed distinct peaks primarily corresponding to the NiO phase, while additional, less intense reflections were attributed to cobalt-containing spinel phases. Raman spectroscopy revealed a strong peak at 690 $cm^{-1}$ and additional secondary peaks associated with $Co_3O_4$. A sharp band at approximately 410 $cm^{-1}$ was also observed, which may originate from either the $CoAl_2O_4$ spinel or the $Al_2O_3$ support. The broader, less defined band centred at 683 $cm^{-1}$, along with the peak shift to lower wavenumbers, further supports the potential presence of $CoAl_2O_4$. However, the overall Raman features were less well-resolved, suggesting some degree of lattice disorder, partial integration with the support, and the coexistence of mixed phases at the interface.

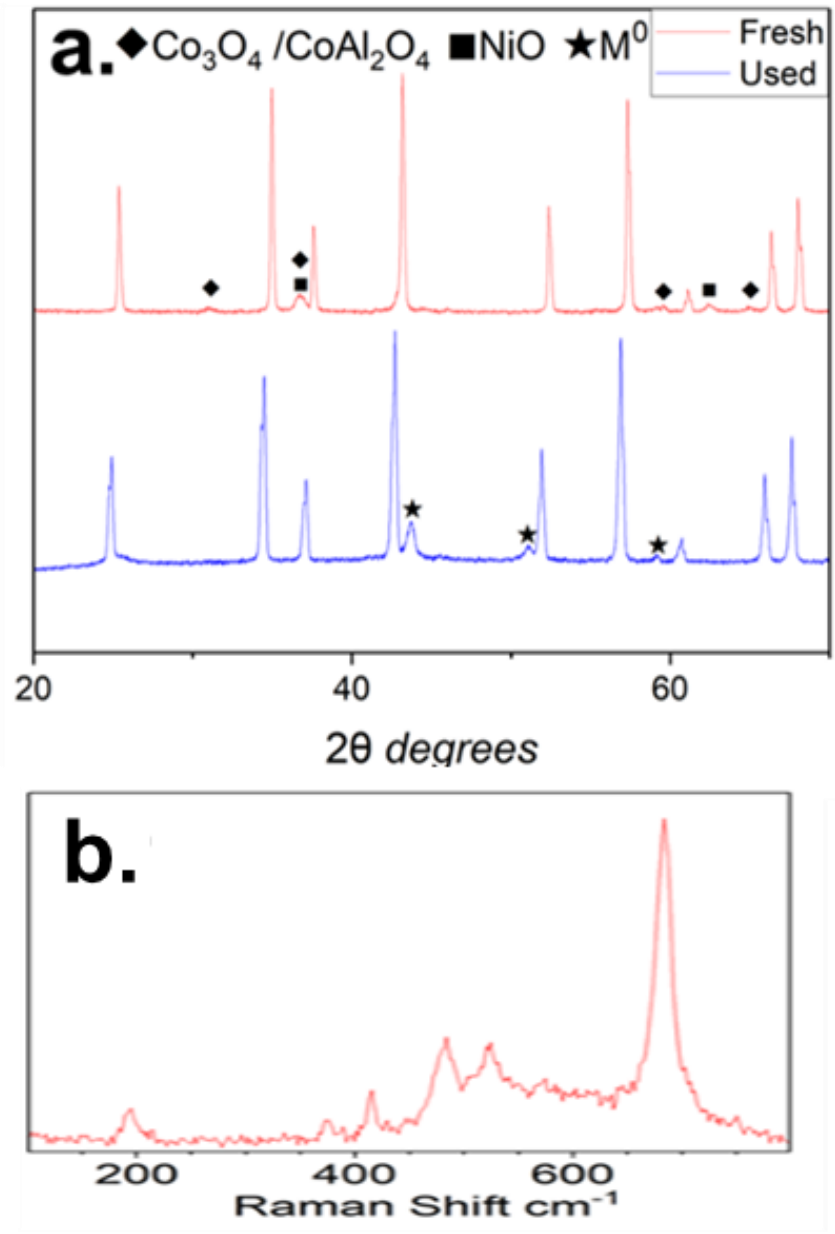


**Figure 4.12.** *Characterisation of the CoNi/Al₂O₃ catalyst showing (a) XRD patterns of fresh and used catalysts with the phases identified, (b) the Raman spectra for the fresh catalyst.*

Figure 4.13 shows that the average NP size was estimated at 18.3 nm for the fresh catalyst and 19.9 nm after use, indicating minimal sintering during operation. TEM-EDX analysis showed excellent nanoparticle dispersion, with the majority of particles under 25 nm and only occasional larger particles around 50 nm. Notably, this catalyst produced the most uniform and spherical nanoparticles among the studied samples. This high degree of morphological control is likely due to the formation of a $CoAl_2O_4$ surface spinel phase, which is known to stabilize nanoparticles on alumina supports and inhibit sintering.

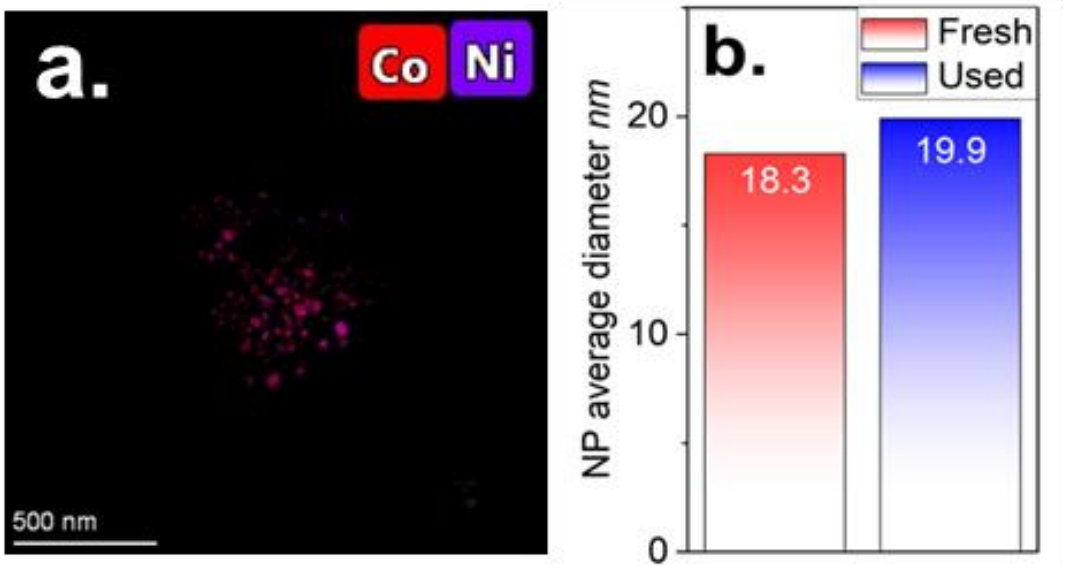


**Figure 4.13.** *Characterisation of the CoNi/$Al_2O_3$ catalyst showing (a) TEM-EDX image of the Co and Ni in the used catalyst and (b) the average NP diameters estimated from XRD.*

## 4.2 Carbon Conversions

### *4.2.1 Carbon Conversions by Different Metal Catalysts*

The percentage of carbon in the PE feedstock converted into carbon material by each catalyst is shown in Figure 4.14.

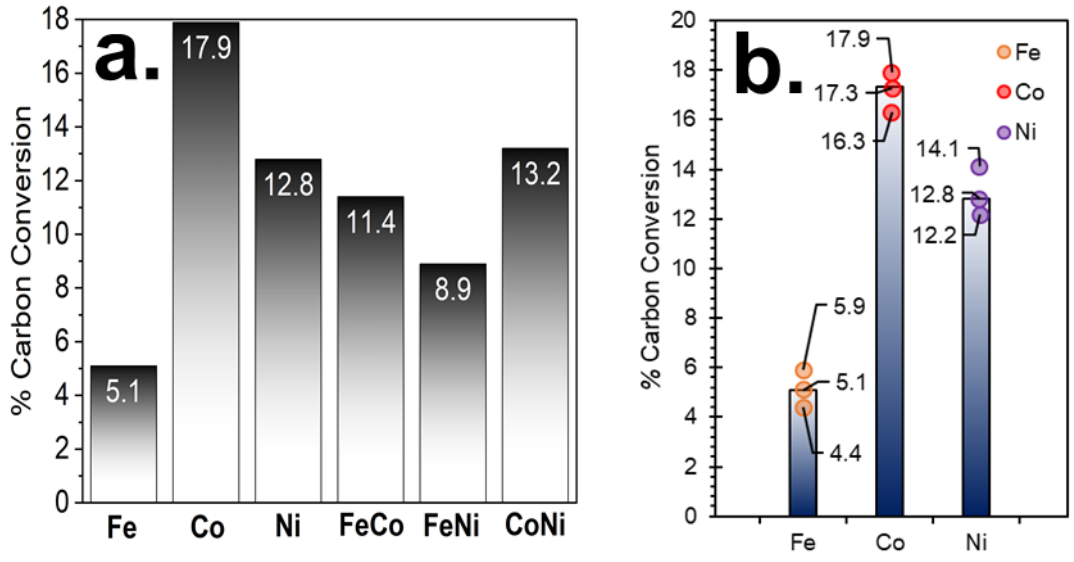


**Figure 4.14.** *Carbon conversions given in feedstock carbon conversion percentage for (a) each catalyst metal species and (b) for the three repeated runs of the monometallic catalysts, with the bar showing the median value.*

Among the catalysts evaluated, Co/$Al_2O_3$ demonstrated the highest carbon conversion at 17.9%, significantly outperforming the other metallic formulations. This

enhanced performance is attributed to its finely dispersed, small NPs, which provide a large surface area and high density of active sites effective for CNM nucleation. The $Ni/Al_2O_3$ catalyst achieved a moderate conversion of 12.8%, which aligns with its moderately sized and well-dispersed NPs observed post-reduction. In contrast, $Fe/Al_2O_3$ exhibited the lowest carbon conversion at 5.1%, a result that can be partially explained by its poor dispersion and the presence of large, agglomerated NPs that are likely too large to serve as effective catalytic site

$CoNi/Al_2O_3$ achieved the highest carbon conversion among the bimetallic catalysts, a result attributed to its uniform, spherical nanoparticles (~20 nm) and the presence of $CoAl_2O_4$. These features indicate the ability of CoNi to resist sintering and thus maintain a high number of active catalytic sites. $FeCo/Al_2O_3$ and $FeNi/Al_2O_3$ exhibited intermediate carbon conversions of 11.4% and 8.9%, respectively. The $FeCo/Al_2O_3$ catalyst showed reduced sintering compared to monometallic Fe, likely due to the inclusion of cobalt, which enhances NP stability. However, it continued to suffer from poor dispersion and agglomeration, indicative of a moderate performance level.

$FeNi/Al_2O_3$ was found to underperform relative to the Ni monometallic catalyst, a result that contrasts with the majority of literature, which reports a beneficial synergistic relationship between Fe and Ni [17] [18] [19] [20]. This synergy typically promotes enhanced catalytic performance in bimetallic systems compared to their individual monometallic counterparts. Although the presence of small nanoparticles associated with $NiFe_2O_4$ in the fresh FeNi catalyst suggests favourable characteristics often linked to improved activity, this did not translate into enhanced carbon conversion. Moreover, in prior studies where FeNi bimetallic outperformed monometallic, Fe was typically more active than Ni [17] [18] [19] [20]. Although, the very low activity observed in this study for the $Fe/Al_2O_3$ catalyst suggests catalytic deactivation, a phenomenon that has previously been reported for Fe-based systems under certain conditions [21] [22] [23]. This deactivation may have not only limited the performance of the Fe monometallic catalyst but also impaired the overall activity of the FeNi bimetallic formulation, thereby diminishing the synergistic effect between the two metals.

The RSD (relative standard deviation) was found to fall within an acceptable range for $Co/Al_2O_3$ and $Ni/Al_2O_3$, with a value of 4.7% and 7.6%, respectively. For $Fe/Al_2O_3$, the high value of 14.6% is due to the low overall conversion, and therefore small variations lead to a large RSD. Overall, the fact that $Co/Al_2O_3$ and $Ni/Al_2O_3$ both give RSD%

comfortably below 10% indicates that for catalysts with a reasonably high conversion the variance between runs is acceptably low.

### 4.2.2 The Deactivation of Iron

The low conversions observed for the Fe catalyst suggest a degree of deactivation, as outlined in the literature review chapter. To further investigate this, XRD analysis was conducted on an $Fe/Al_2O_3$ sample that had been stopped during the temperature ramp, reaching a maximum of 500 °C, which is shown in Figure 4.15. This approach was designed to capture the phase evolution before reaching the final reaction temperature, providing insights into early-stage transformations that may contribute to catalyst deactivation.

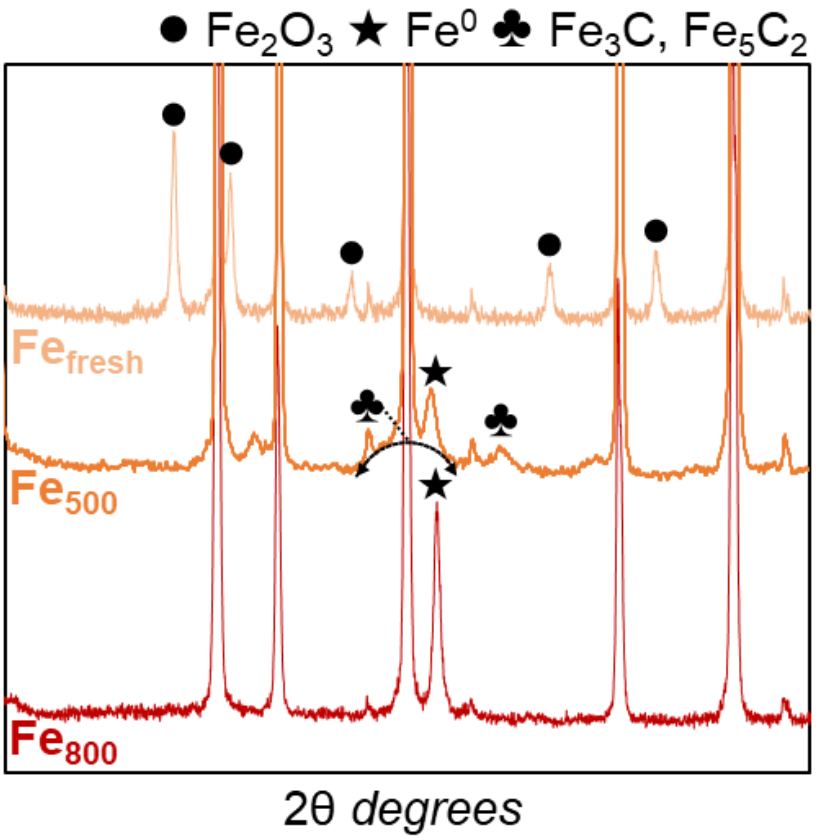


**Figure 4.15.** *XRD pattern of $Fe/Al_2O_3$ catalysts, showing the fresh catalyst in light orange, the catalyst extracted from a run during temperature ramp to 500 °C in dark orange, and the used catalyst in red.*

Comparative XRD analysis between the 500 °C sample and a fully reduced $Fe/Al_2O_3$ catalyst revealed the presence of $Fe^0$, $Fe_3O_4$, but notably not FeO. This suggests that the expected reduction pathway is not fully followed, indicating unstable or non-stochiometric oxide intermediates. The broad XRD peak between ~40-45° 2θ, which can be attributed to iron carbide phases such as $Fe_2C$, $Fe_3C$ and $Fe_5C_2$ [3] [24] [25].

These phases are known to be catalytically inactive and their presence during the ramp stage suggests that iron becomes trapped in an inactive form early in the process. This is critical because while in an inactive state, iron can undergo rapid carbon uptake. The resulting carbon flux may lead to encapsulation of the iron nanoparticles by graphitic layers, effectively deactivating them before the system reaches temperatures conducive to carbon precipitation by the vapour-liquid-solid mechanism. This observation also offers a plausible explanation for the underperformance of the FeNi and FeCo bimetallic catalysts. The formation of inactive iron phases likely disrupted the catalytic function of the more active Co or Ni components.

## 4.3 Carbon Morphology

The carbon morphology deposited on each of the metallic species was analysed by SEM, TEM and TEM-EDX.

### *4.3.1 $Fe/Al_2O_3$*

Figure 4.16 shows the SEM, TEM and TEM-EDX results for the used $Fe/Al_2O_3$ catalyst. SEM showed that $Fe/Al_2O_3$ catalysed the formation of patches of carbon deposits suggesting localised activity due to poor Fe dispersion on the support. These were in the form of spherical aggregates, with TEM confirming these to be were core-shell Fe@CNO structures where Fe nanoparticles were encapsulated in concentric graphitic shells. The limited filament formation, coupled the spherical encapsulation of the NPs, suggests carbon oversaturation [26]. Indeed, high carbon flux has previously been linked to the formation of CNOs due to dangling carbon bonds which binding to the metal NP surface in order to stabilise, and thus a curved morphology is imparted [27]. This would agree well with the inactive carbide phase of the catalyst discussed in Section 4.2.2, as the lack of ability to efficiently decompose precursor molecules will allow for overaccumulation and growth not mediated by active $Fe^0$ NPs. Additionally, TEM-EDX revealed that the carbon formed around detected NPs without alumina support present. Early detachment and therefore lack of MSI would result in a more isotropic NP**,** favouring spherical carbon deposits.

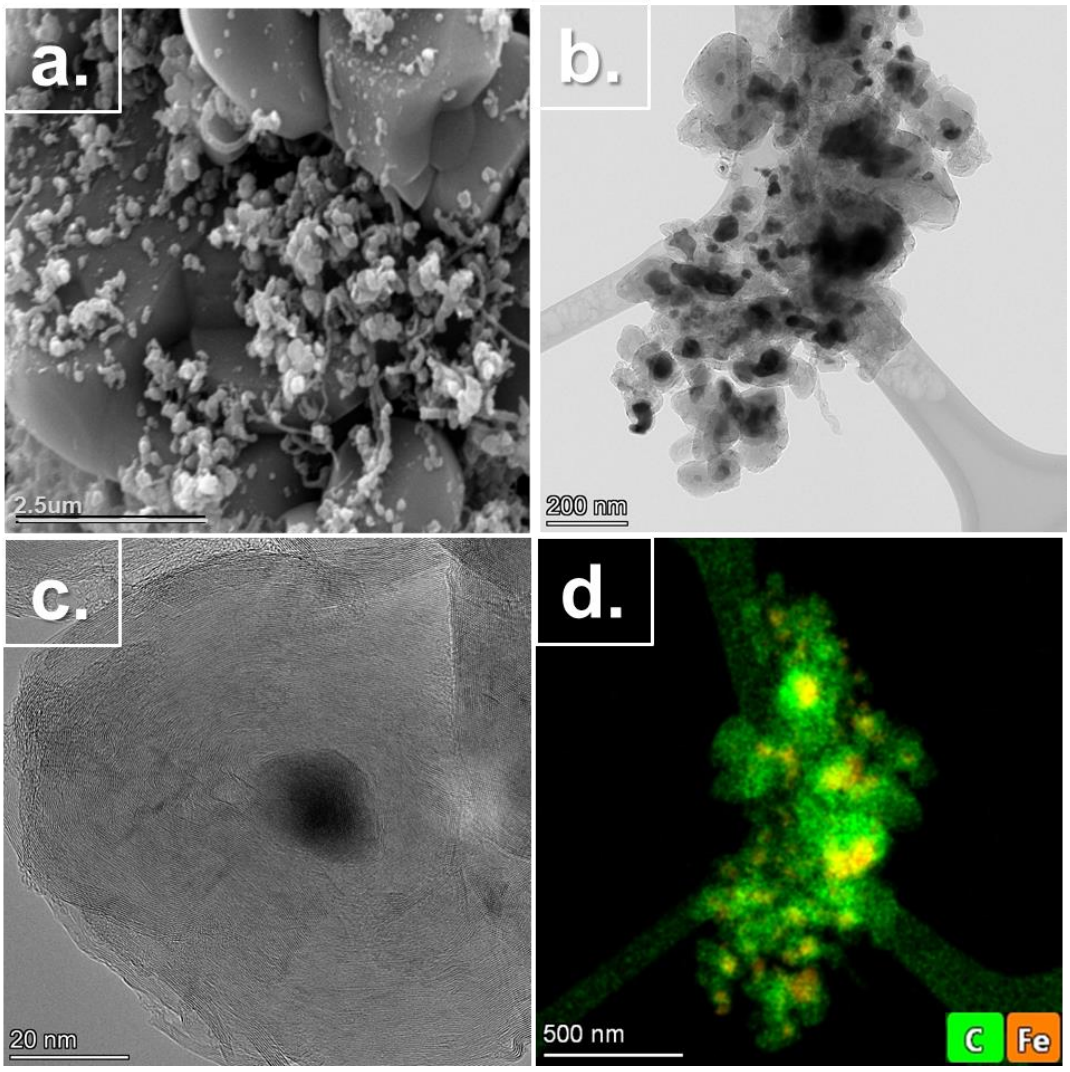


**Figure 4.16.** *Images showing the morphology of the carbon deposited on the Fe/$Al_2O_3$ catalysts, obtained by (a) SEM, (b)(c) TEM and (d) TEM-EDX, with carbon shown in green and Fe in orange.*

### *4.3.2 Co/$Al_2O_3$*

Figure 4.17 illustrates the structural features of the carbon formed using the Co/$Al_2O_3$ catalyst, which facilitated the formation of both dense, spherical carbon aggregates and filamentous carbon as show by the SEM. The TEM image confirms that the spherical structures were core-shell Co@CNOs, with cobalt NPs encapsulated within concentric graphitic layers, with similar structures previously observed for Co-based catalysts [28]. The filamentous structures formed two distinct groups, smaller diameters filaments of ~20nm were found to be MWNTs highly ordered, parallel graphitic walls indicative of uniform growth and stable carbon precipitation. Whereas, larger mixed MWNT and CNF structures were also observed with diameters over 50nm, which exhibited a more disordered structure. The coexistence of Co@CNOs,

MWNTs and CNF in the same system implies that cobalt nanoparticles can initiate multiple carbon growth pathways, depending on factors such as NP morphology, degree of coordination with the support, and local carbon flux. Cobalt has previously been shown to facilitate both encapsulated and tubular carbon formation under similar conditions [29]. TEM-EDX mapping showed that the majority of carbon deposits were located around cobalt nanoparticles that had become detached from the alumina support, indicating a tip growth mode.

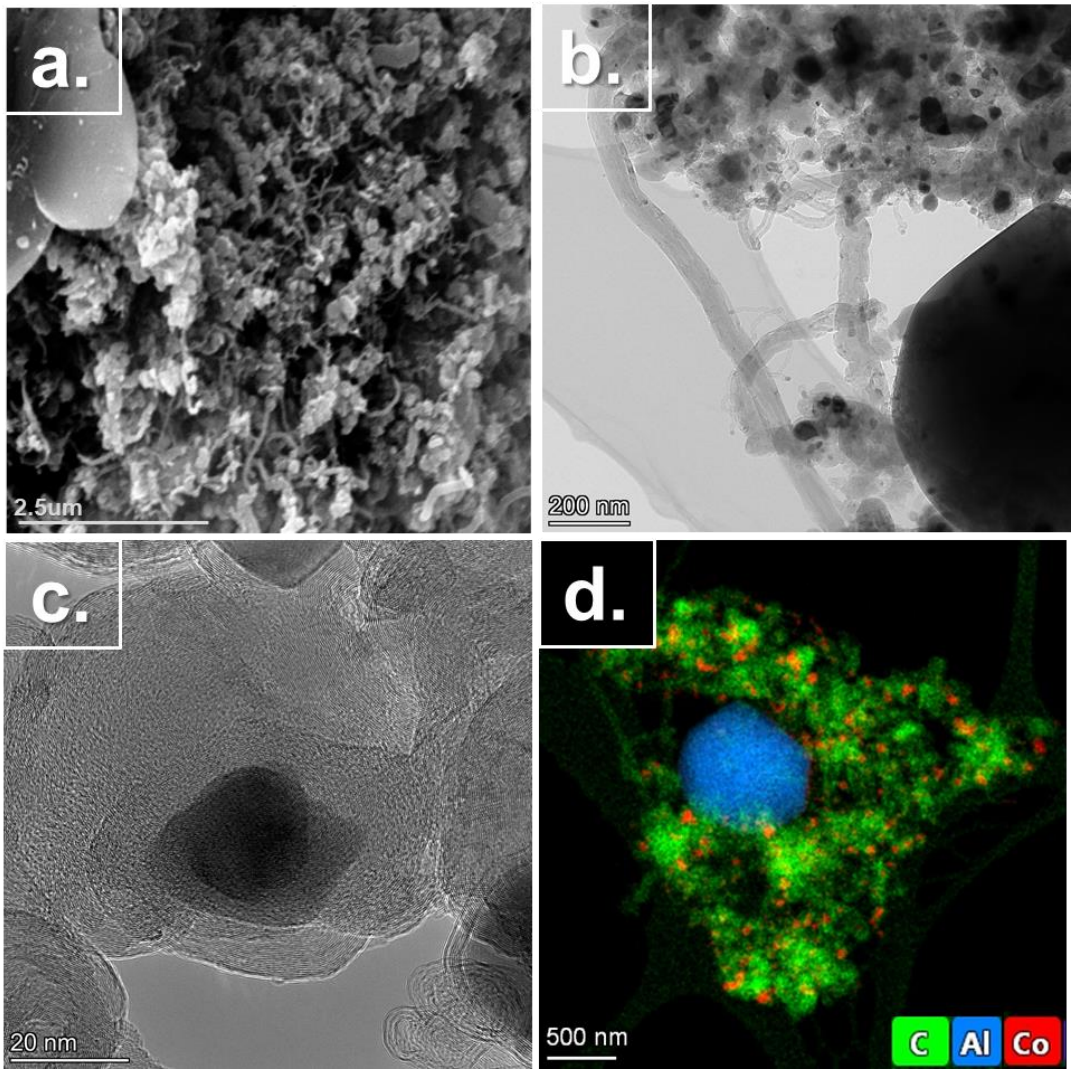


**Figure 4.17.** *Images showing the morphology of the carbon deposited on the Co/$Al_2O_3$ catalysts, obtained by (a) SEM, (b)(c) TEM and (d) TEM-EDX, with carbon shown in green, Co in red and Al in blue.*

### *4.3.3 Ni/$Al_2O_3$*

Figure 4.18 displays the SEM and TEM analysis of the carbon deposited on the Ni/$Al_2O_3$ catalyst. Among the metallic species, nickel produced the highest quantity of

filamentous carbon, which appeared in SEM as dense, interwoven networks spanning the support surface. TEM analysis confirmed these structures to be MWNTs, exhibiting a mixture of straight parallel-walled tubes and angled fishbone-like morphologies. In addition to these structured carbon nanomaterials, some regions displayed amorphous carbon deposits, indicating non-uniform carbon deposits. TEM-EDX revelated that while some Ni NPs remained anchored to the alumina support, there is limit carbon deposits on these. Whereas, a high carbon density can be observed around the detached NPs, indicating that a tip-growth mode is followed, with carbon deposits pushing the NPs of the support surface. The presence of both support-bound and detached NP indicates relatively strong MSI, which likely helped maintain nanoparticle shape and orientation long enough to favour structured CNT formation.

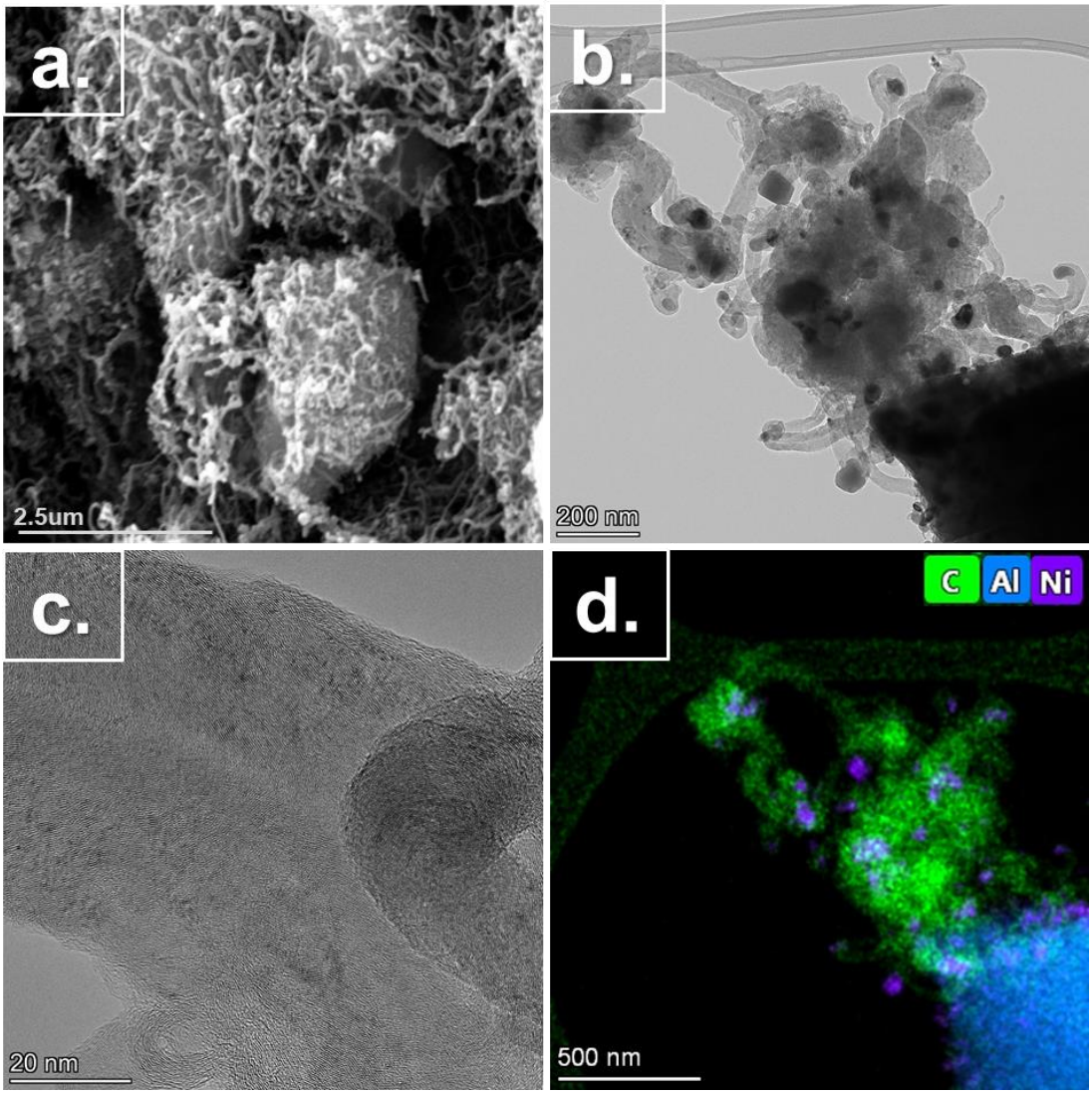


**Figure 4.18.** *Images showing the morphology of the carbon deposited on the Ni/$Al_2O_3$ catalysts, obtained by (a) SEM, (b)(c) TEM and (d) TEM-EDX, with carbon shown in green, Ni in purple and Al in blue.*

### *4.3.4 CoFe/$Al_2O_3$*

Figure 4.19 presents the morphological and structural characterisation of the FeCo/$Al_2O_3$ catalyst after CNM synthesis. SEM revealed the formation of large-diameter filamentous structures, which TEM analysis confirmed to be MWNTs with disordered, bamboo-like wall morphologies showed sparse carbon coverage and low overall CNM conversion. The large FeCo NPs showed poor dispersion, and were coated by carbon of irregular morphology, containing both graphitic and amorphous regions, indicative of catalyst deactivation. The irregular morphology of the carbon products and the low nucleation density suggest that the FeCo bimetallic system failed to exhibit synergistic effects. Furthermore, although a degree of alloying is observed, TEM-EDX reveals both larger Fe-rich and small Co NPs are present. This distribution

implies partial metal segregation, leading to heterogeneous catalytic behaviour. Such phase separation likely hindered uniform carbon growth and contributed to heterogeneous CNM formation.

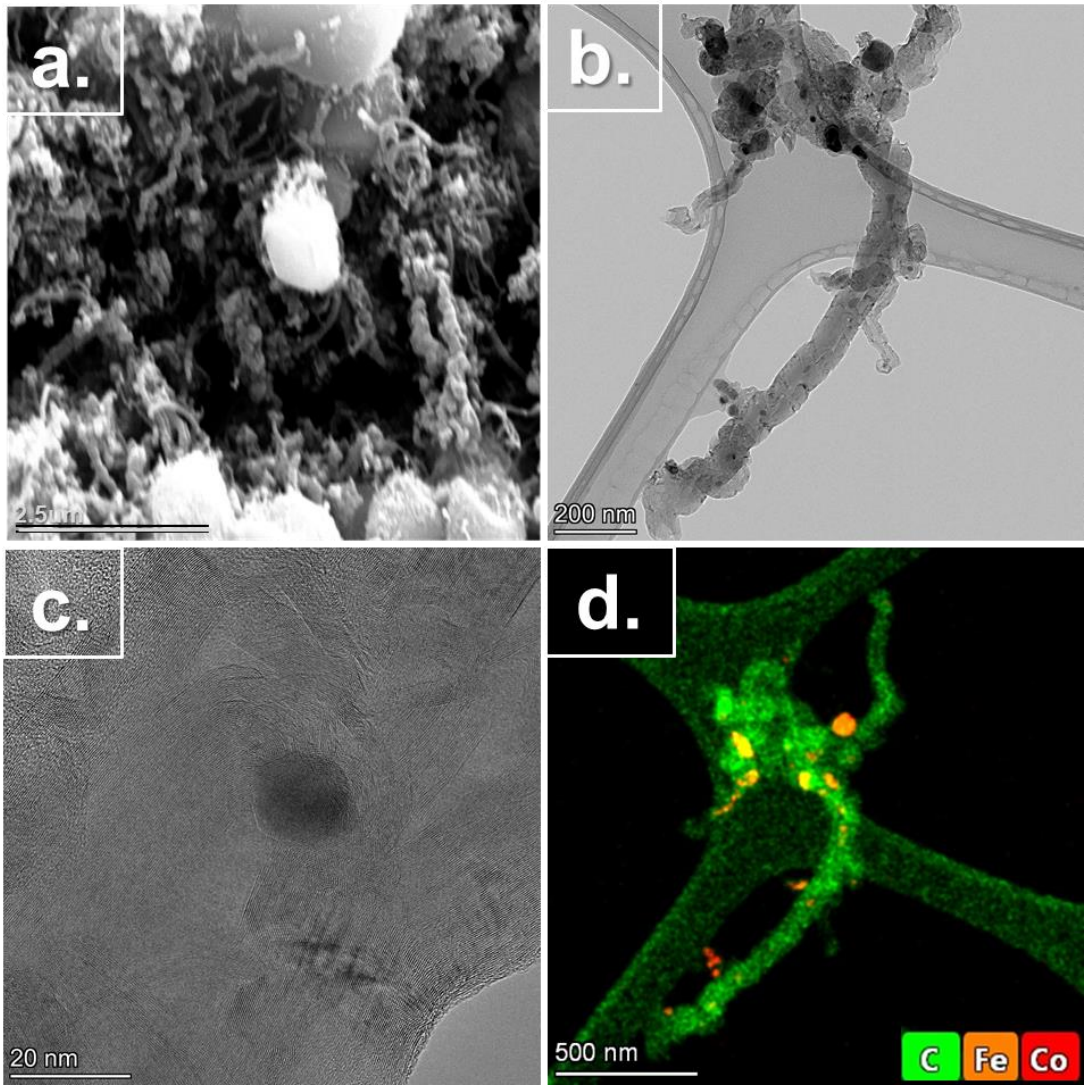


**Figure 4.19.** *Images showing the morphology of the carbon deposited on the FeCo/$Al_2O_3$ catalysts, obtained by (a) SEM, (b)(c) TEM and (d) TEM-EDX, with carbon shown in green, Fe in orange and Co in red.*

### *4.3.5 FeNi/$Al_2O_3$*

Figure 4.20 presents characterisation of the carbon deposited on the FeNi/$Al_2O_3$ catalyst. SEM images revealed the formation of filamentous carbon structures with highly variable diameters, along with spherical carbon aggregates. TEM analysis confirmed he spherical features were identified as FeNi@C core-shell structures, enclosed in graphitic carbon layers. The filaments features were found to be bamboo-like MWNTs, exhibiting disordered graphitic walls. Notably, the bamboo-like CNTs

displayed irregular, sharp bends and occasional Y-junctions, suggesting multi-nucleation growth from uneven or multi-faceted NPs. TEM-EDX analysis showed substantial carbon accumulation around nanoparticles, but with limited formation of extended CNTs. This suggests that encapsulation, rather than tubular growth, was favoured during growth. As with FeCo, EDX also revealed several metal nanoparticles isolated from any carbon deposits, indicating a fraction of inactive sites with poor carbon deposition capabilities. Although, in this case a relatively uniform FeNi alloying, with minimal phase separation was observed, therefore phase separation cannot explain the underperformance of the $FeNi/Al_2O_3$ catalyst.

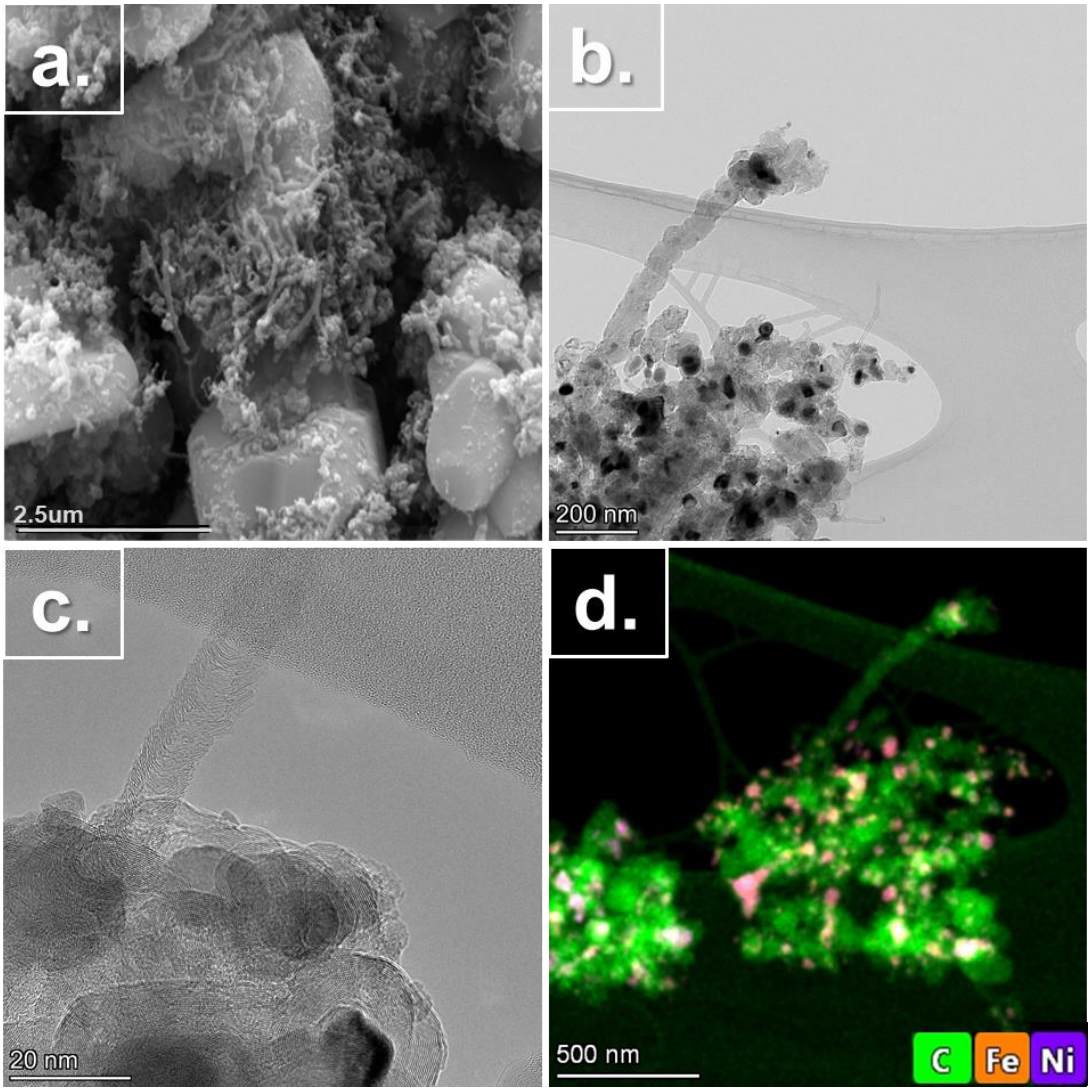


**Figure 4.20.** *Images showing the morphology of the carbon deposited on the $FeNi/Al_2O_3$ catalysts, obtained by (a) SEM, (b)(c) TEM and (d) TEM-EDX, with carbon shown in green, Fe in orange and Ni in purple.*

### 4.3.6 $CoNi/Al_2O_3$

Figure 4.21 depicts the post-synthesis morphology of the $CoNi/Al_2O_3$ catalyst and the carbon formed. SEM revealing a mixture of small spherical carbon structures and filamentous. TEM confirmed these to be encapsulated core-shell CoNi@CNOs and CNTs, respectively. The high volume of spherical carbon morphology can be explained by the high quantity of fairly uniformly sized spherical CoNi NPs. Although graphitic layering was evident across most structures, smaller NP exhibiting more well-ordered thickly layered graphitic shells, while the deposits around larger NPs consisted of fewer graphic layers. This supports a size-dependent catalytic behaviour, where the higher surface curvature and increased surface area of small NPs leads to increased activity. Interestingly, EDX-TEM mapping revealed alumina-derived aluminium atoms embedded within the carbon deposits. This suggests that interfacial incorporation of support material occurred, possibly during the reduction phase, where strong support-carbon interaction cause atomic diffusion into the forming carbon matrix. Moreover, TEM-EDX showed a separation of cobalt and nickel was detected. Regions rich in Ni were more often associated with CNT growth, while Co-enriched domains favoured spherical carbon morphologies.

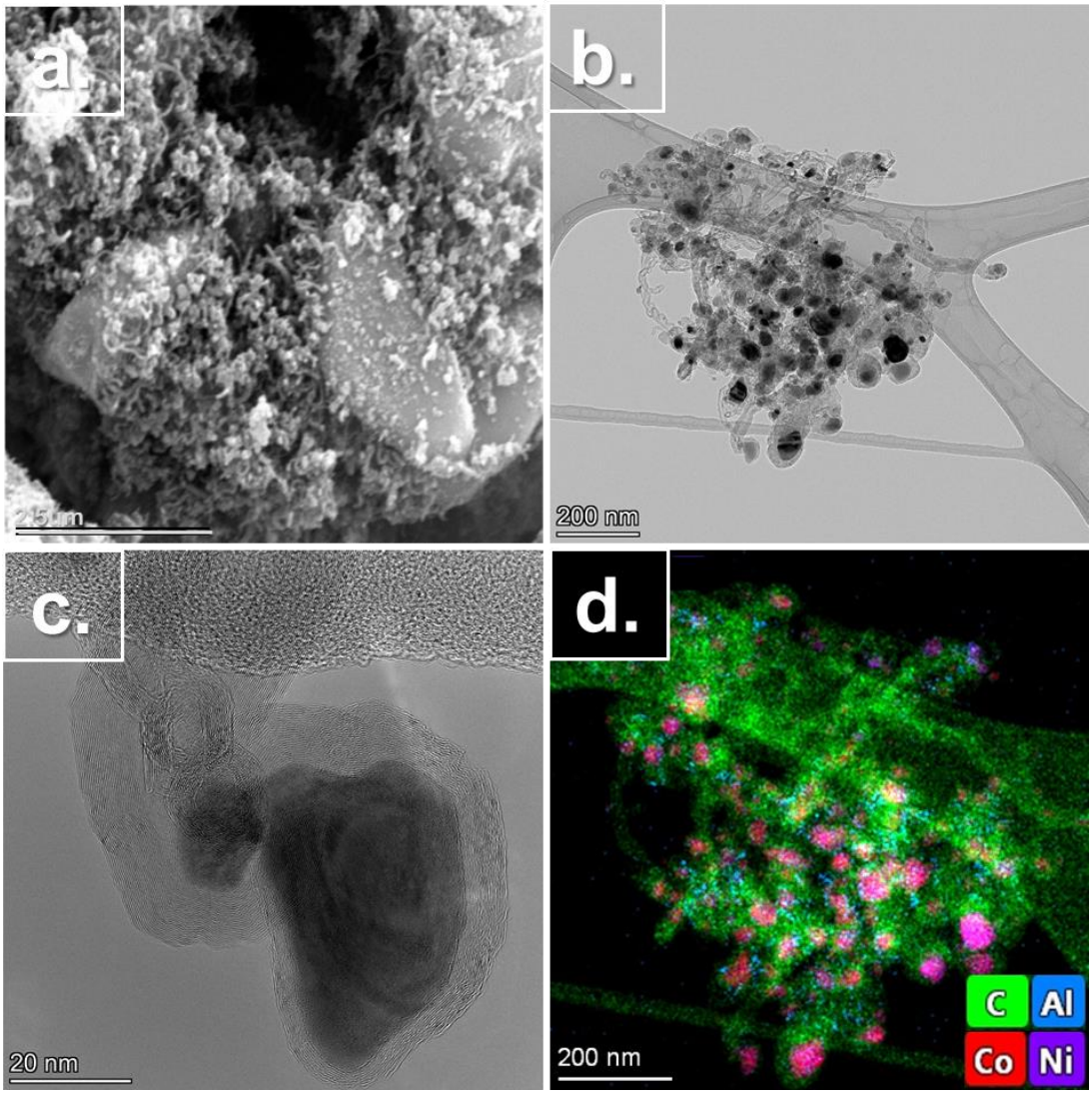


**Figure 4.21.** *Images showing the morphology of the carbon deposited on the CoNi/$Al_2O_3$ catalysts, obtained by (a) SEM, (b)(c) TEM and (d) TEM-EDX, with carbon shown in green, Co in red, Ni in purple and Al in blue.*

## 4.4 Graphitic Quality

Raman spectroscopy, shown in Figure 4.22, was employed to evaluate the structural quality and degree of graphitisation of the CNMs synthesised on each catalyst. The D/G ratio, which refers to the intensity ratio of the disorder-induced D-band to the graphitic G-band, provides insight into the level of defects in the carbon lattice. A lower D/G ratio indicates fewer structural defects and higher graphitic ordering. The 2D/G ratio serves as an additional metric of graphitic character, particularly relevant to the stacking and curvature of graphitic layers in nanotubes or concentric structures.

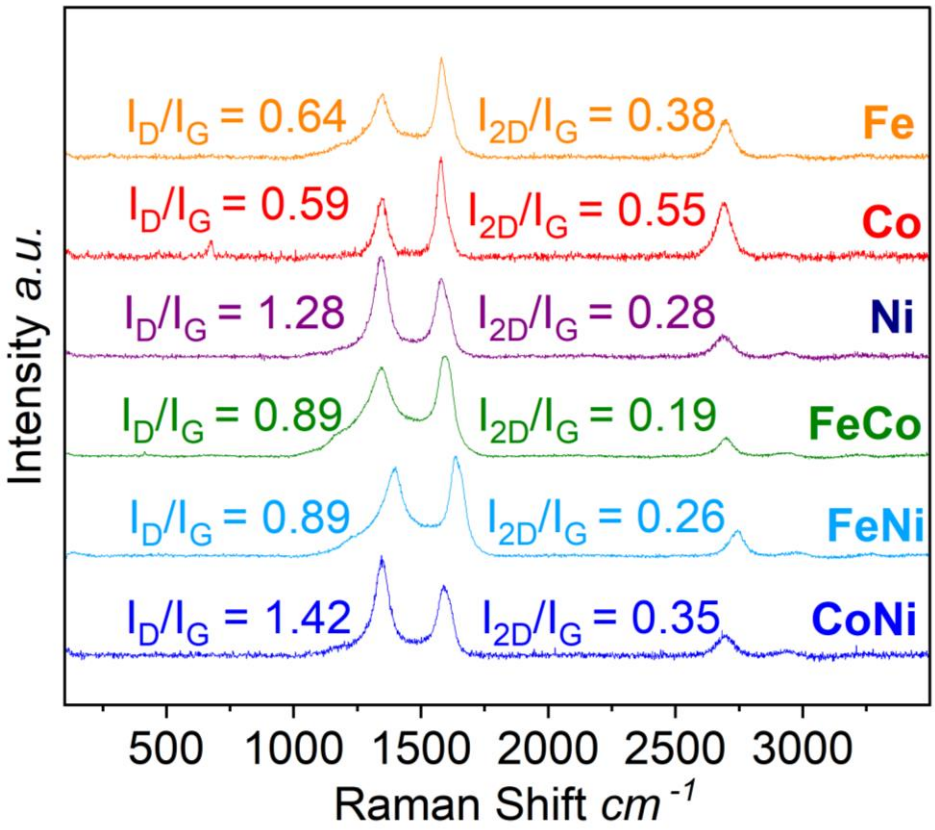


**Figure 4.22.** *Raman spectroscopy of the carbon material deposited on each catalyst with Fe shown in orange, Co in red, Ni in purple, FeCo in green FeNi in light blue and CoNi in dark blue.*

The $Fe/Al_2O_3$ catalyst produced carbon with a relatively low D/G ratio (0.64), indicating a moderate degree of $sp^2$-hybridised carbon and some long-range ordering. The corresponding 2D/G ratio of 0.38 is consistent with the presence of few-layer graphitic domains, consistent with the concentric carbon layers found by TEM. $Co/Al_2O_3$ yielded the most structurally ordered carbon of all catalysts, as reflected by the lowest D/G of 0.59, correlating with well-formed carbon structures with fewer defects. The high 2D/G ratio of 0.55 indicates thin graphic walls, aligning with the thin CNTs and small diameter core-shell structures found be TEM. In contrast, the $Ni/Al_2O_3$ catalyst exhibited a high D/G ratio of 1.28, indicating substantial structural disorder in the resulting carbon. The low 2D/G value of 0.28 further supports this, pointing to the formation of turbostratic carbon with thick poorly aligned graphitic layers.

$FeCo/Al_2O_3$ and $FeNi/Al_2O_3$ catalysts produced carbon with intermediate D/G ratios, with both having a value of 0.89. However, their low 2D/G ratios of 0.19 and 0.26, respectively, indicate a predominance of multi-layered graphitic structures with irregular turbostratic stacking. This agree with the disorder bamboo-like CNTs and

regions of amorphous carbon found by TEM. In the case of $CoNi/Al_2O_3$ despite forming well-dispersed and spherical nanoparticles, the D/G ratio was the highest found at 1.42, suggesting a significant level of structural defects. This can be explained by the inclusion of Al atoms in the CNMs as found by TEM-EDX. The introduction of heteroatomic disruptions to the graphitic lattice, which in turn distorts the conjugated π-system, introduces curvature and generates lattice strain, all of which contribute to increased D-band intensity.

## 4.5 Thermal Stability of Carbon

The thermal stability of the carbon deposits, as measured by temperature programmed oxidation (TPO) and shown in Figure 4.23, can be used to determine if filamentous or amorphous carbon morphology is present. This assumes that filamentous carbon is oxidised at a higher temperature, with amorphous carbon oxidised at a lower temperature. The $Fe/Al_2O_3$ and $FeCo/Al_2O_3$ catalysts exhibited broad oxidation peaks centred around 550 °C. This broadness is indicative of structural heterogeneity in the carbon deposits, suggesting a mixture of amorphous carbon and different types of CNMs. In contrast, $Ni/Al_2O_3$ and $FeNi/Al_2O_3$ demonstrated sharper oxidation peaks near 600 °C, consistent with the presence of thermally stable multi-walled CNTs. Furthermore, the minimal carbon oxidation observed below ~550 °C suggests a higher carbon quality and filamentous purity.

Interestingly, $Co/Al_2O_3$ and $CoNi/Al_2O_3$ showed oxidation onset at significantly lower temperatures despite SEM and TEM evidence confirming the presence of well-formed CNTs and graphitic shells. This lower oxidation temperature may be attributed to a metal-assisted oxidation effect, wherein the proximity of carbon to metal in core-shell nanostructures facilitates earlier combustion. Additionally, the well dispersed nature of the NPs in these systems likely contributes to enhanced oxidation due to increased surface area and greater metal-carbon interface.

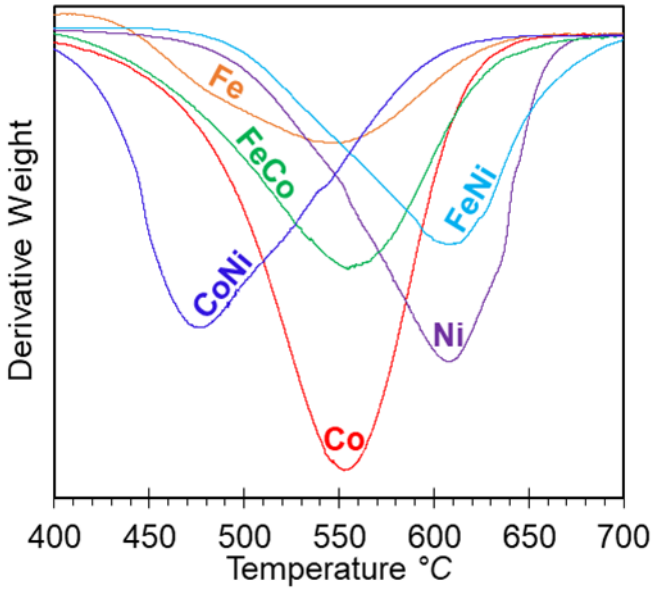


**Figure 4.23.** TPO derivative weight loss curves shown for each alumina supported monometallic and bimetallic catalyst.

## 4.6 Conclusion

The role of metal catalysts and their bimetallic variants were assessed, with the underlying mechanisms for the performances investigated. Cobalt and nickel catalysts demonstrated more efficient reduction and finer nanoparticle dispersion, while iron-based systems suffered from sintering, phase instability and early formation of catalytically inactive carbide species. These inactive phases were shown to hinder catalytic performance and may explain the suppression of expected synergistic effects in bimetallic systems.

The different metal species exhibited a range of morphologies of the deposited carbon. $Co/Al_2O_3$ and $CoNi/Al_2O_3$ facilitated both filamentous and spherical carbon formation, with clear indications of tip-growth mechanisms and high nanoparticle dispersion. Additionally, these catalysts demonstrated the highest conversion efficiencies, driven by well-dispersed, stable nanoparticles and strong metal-support interactions. In contrast, Fe-based catalysts predominantly formed encapsulated CNOs and disordered bamboo-like CNTs, a result of poor dispersion, carbon oversaturation, and nanoparticle detachment. Ni-based catalysts achieved higher CNT conversion but exhibited substantial disorder, as reflected in high D/G ratios from Raman spectra. Collectively, the results underscore the necessity of tuning both the

metal composition and its interaction with the support to achieve optimal catalytic performance.

# References


[1] A. A. Mohammed, Z. T. Khodair, and A. A. Khadom, “Preparation and investigation of the structural properties of α-Al2O3 nanoparticles using the sol-gel method,” *Chemical Data Collections*, vol. 29, 2020, doi: 10.1016/j.cdc.2020.100531.

[2] E. Paterson, “The Iron Oxides. Structure, Properties, Reactions, Occurrences and Uses,” *Clay Miner.*, vol. 34, no. 1, 1999, doi: 10.1180/claymin.1999.034.1.20.

[3] A. Peigney, C. Laurent, O. Dumortier, and A. Rousset, “Carbon nanotubes-Fe-alumina nanocomposites. Part I: Influence of the Fe content on the synthesis of powders,” *J. Eur. Ceram. Soc.*, vol. 18, no. 14, 1998, doi: 10.1016/s0955-2219(98)00141-1.

[4] D. Torres, J. L. Pinilla, and I. Suelves, “Cobalt doping of α-Fe/Al2O3 catalysts for the production of hydrogen and high-quality carbon nanotubes by thermal decomposition of methane,” *Int. J. Hydrogen Energy*, vol. 45, no. 38, 2020, doi: 10.1016/j.ijhydene.2020.05.104.

[5] H. Irfan, K. Mohamed Racik, and S. Anand, “Microstructural evaluation of CoAl2O4 nanoparticles by Williamson–Hall and size–strain plot methods,” *Journal of Asian Ceramic Societies*, vol. 6, no. 1, 2018, doi: 10.1080/21870764.2018.1439606.

[6] C. M. Álvarez-Docio, J. J. Reinosa, A. Del Campo, and J. F. Fernández, “Investigation of thermal stability of 2D and 3D CoAl2O4 particles in core-shell nanostructures by Raman spectroscopy,” *J. Alloys Compd.*, vol. 779, 2019, doi: 10.1016/j.jallcom.2018.11.263.

[7] Y. Ding, C. C. Hu, W. Q. Sheng, K. X. Song, and B. Liu, “Crystal structure, microwave dielectric properties, and dielectric resonant antenna studies of novel low-permittivity CoAl2O4 spinel ceramics,” *Journal of Materials Science: Materials in Electronics*, vol. 32, no. 18, 2021, doi: 10.1007/s10854-021-06760-2.

[8] V. D’Ippolito, G. B. Andreozzi, D. Bersani, and P. P. Lottici, “Raman fingerprint of chromate, aluminate and ferrite spinels,” *Journal of Raman Spectroscopy*, vol. 46, no. 12, 2015, doi: 10.1002/jrs.4764.

[9] S. Sadasivan, R. M. Bellabarba, and R. P. Tooze, “Size dependent reduction-oxidation-reduction behaviour of cobalt oxide nanocrystals,” *Nanoscale*, vol. 5, no. 22, 2013, doi: 10.1039/c3nr02877a.

[10] E. Romeo, M. Saeys, A. Monzón, and A. Borgna, “Carbon nanotube formation during propane decomposition on boron-modified Co/Al2O3 catalysts: A kinetic study,” in *International Journal of Hydrogen Energy*, 2014. doi: 10.1016/j.ijhydene.2014.04.168.

[11] M. J. Lee *et al.*, “Comparative structural and electrical analysis of NiO and Ti doped NiO as materials for resistance random access memory,” *J. Appl. Phys.*, vol. 103, no. 1, 2008, doi: 10.1063/1.2829814.

[12] P. B. Kharat, S. B. Somvanshi, J. S. Kounsalye, S. S. Deshmukh, P. P. Khirade, and K. M. Jadhav, “Temperature dependent viscosity of cobalt ferrite / ethylene glycol ferrofluids,” in *AIP Conference Proceedings*, 2018. doi: 10.1063/1.5028675.

[13] O. N. Shebanova and P. Lazor, “Raman study of magnetite (Fe3O4): Laser-induced thermal effects and oxidation,” *Journal of Raman Spectroscopy*, vol. 34, no. 11, 2003, doi: 10.1002/jrs.1056.

[14] Á. de Jesús Ruíz-Baltazar, S. Y. Reyes-López, and R. Pérez, “Magnetic structures synthesized by controlled oxidative etching: Structural characterization and magnetic behavior,” *Results Phys.*, vol. 7, 2017, doi: 10.1016/j.rinp.2017.05.001.

[15] S. H. Chaki, T. J. Malek, M. D. Chaudhary, J. P. Tailor, and M. P. Deshpande, “Magnetite Fe3O4 nanoparticles synthesis by wet chemical reduction and their characterization,” *Advances in Natural Sciences: Nanoscience and Nanotechnology*, vol. 6, no. 3, 2015, doi: 10.1088/2043-6262/6/3/035009.

[16] M. Sugimoto, “The Past, Present, and Future of Ferrites,” *Journal of the American Ceramic Society*, vol. 82, no. 2, 1999, doi: 10.1111/j.1551-2916.1999.tb20058.x.

[17] D. Yao, Y. Zhang, P. T. Williams, H. Yang, and H. Chen, “Co-production of hydrogen and carbon nanotubes from real-world waste plastics: Influence of catalyst composition and operational parameters,” *Appl. Catal. B*, vol. 221, 2018, doi: 10.1016/j.apcatb.2017.09.035.

[18] D. Yao and C. H. Wang, “Pyrolysis and in-line catalytic decomposition of polypropylene to carbon nanomaterials and hydrogen over Fe- and Ni-based catalysts,” *Appl. Energy*, vol. 265, 2020, doi: 10.1016/j.apenergy.2020.114819.

[19] Q. Liu *et al.*, “Investigating the influences of metal-support interaction in Ni[sbnd]Fe catalysts on the quality of carbon nanomaterials from waste polypropylene,” *Fuel Processing Technology*, vol. 236, 2022, doi: 10.1016/j.fuproc.2022.107428.

[20] K. Li, H. Zhang, Y. Zheng, G. Yuan, Q. Jia, and S. Zhang, “Catalytic preparation of carbon nanotubes from waste polyethylene using feni bimetallic nanocatalyst,” *Nanomaterials*, vol. 10, no. 8, 2020, doi: 10.3390/nano10081517.

[21] J. Wang, B. Shen, M. Lan, D. Kang, and C. Wu, “Carbon nanotubes (CNTs) production from catalytic pyrolysis of waste plastics: The influence of catalyst and reaction pressure,” 2020. doi: 10.1016/j.cattod.2019.01.058.

[22] J. Gong *et al.*, “Catalytic carbonization of polypropylene by the combined catalysis of activated carbon with Ni2O3 into carbon nanotubes and its mechanism,” *Appl. Catal. A Gen.*, vol. 449, pp. 112–120, 2012, doi: 10.1016/j.apcata.2012.09.028.

[23] K. Jagodzińska, P. G. Jönsson, and W. Yang, “Pyrolysis and in-line catalytic decomposition of excavated landfill waste to produce carbon nanotubes and hydrogen over Fe- and Ni-based catalysts – Investigation of the catalyst type and process temperature,” *Chemical Engineering Journal*, vol. 446, 2022, doi: 10.1016/j.cej.2022.136808.

[24] N. Luo, X. Li, X. Wang, H. Yan, C. Zhang, and H. Wang, “Synthesis and characterization of carbon-encapsulated iron/iron carbide nanoparticles by a detonation method,” *Carbon N. Y.*, vol. 48, no. 13, 2010, doi: 10.1016/j.carbon.2010.06.051.

[25] X. Yang *et al.*, “Preparation of iron carbides formed by iron oxalate carburization for fischer-tropsch synthesis,” *Catalysts*, vol. 9, no. 4, 2019, doi: 10.3390/catal9040347.

[26] H. Dong *et al.*, “Pyrolysis gas from biomass and plastics over X-Mo@MgO (X = Ni, Fe, Co) catalysts into functional carbon nanocomposite: Gas reforming reaction and proper process mechanisms,” *Science of the Total Environment*, vol. 831, 2022, doi: 10.1016/j.scitotenv.2022.154751.

[27] A. S. Rettenbacher, M. W. Perpall, L. Echegoyen, J. A. Hudson, and D. W. Smith, “Radical addition of a conjugated polymer to multilayer fullerenes (Carbon Nano-onions),” *Chemistry of Materials*, vol. 19, no. 6, 2007, doi: 10.1021/cm0626132.

[28] M. Xiao *et al.*, “In-situ encapsulation of core-shell structured Co@Co3O4@CNOs as anode for lithium-ion batteries with high rate performance,” *Journal of Electroanalytical Chemistry*, vol. 873, 2020, doi: 10.1016/j.jelechem.2020.114454.

[29] W. Luo *et al.*, “Co-pyrolysis of Chinese herb residue and polypropylene over Ni, Fe, Co and Cu/AC: Co-production and formation mechanism of carbon nanomaterials, liquid oil and pyrolysis gas,” *Energy*, vol. 244, 2022, doi: 10.1016/j.energy.2021.122634.

# Chapter 5

# Effect of Catalyst Support

The synthesis of CNMs is heavily influenced by the nature of the catalyst used, particularly the interplay between the active metal species and the support material. Supports influence not only the physical anchoring and growth dynamics of nanoparticles (NP) but also the thermal and chemical environments experienced during calcination and reaction. Additionally, supports themselves can influence the cracking of precursor molecules, and thus carbon supply rates. Three distinct morphologies are tested, Y-Faujasite zeolite (FAU) with three dimensional interconnected pores, mordenite (MOR) with one dimensional parallel linear pores and Kaolin clay (KAO) which cleaves on a flat plane. The supports are each assessed in terms of the NPs sizes in oxide and metallic phase, to determine dispersion of metal and resistance to sintering. Subsequently, the conversions, quality and morphology of the carbon deposited on each catalyst is analysed. Therefore, this section investigates how different combinations of transition metals and supports affect catalytic behaviour during CNM growth. Therefore, by comparation different catalyst-support combinations can provide insight into how the interplay between metal species and support material affects overall performance.

## 5.1 Characterisation of Fresh Catalysts

The structural characteristics of the catalysts synthesised using each supporting material in both fresh and used form were characterised using a combination of analytical techniques. XRD was performed to identify the crystalline metallic phases and to estimate the average NP sizes. To complement the XRD-derived size estimates and provide insight into particle dispersion and morphology, TEM-EDX carried out on the Co and Ni catalysts enabled direct imaging of the metal NPs, revealing their distribution and size range.

### *5.1.1 KAO-supported*

Figure 5.1 presents the characterisation data for the fresh KAO-supported catalysts. Fe/KAO exhibited prominent XRD peaks consistent with hematite (α-$Fe_2O_3$), with reflections at 2θ = 33.1°, 35.6°, and 54.1°, corresponding to the (104), (110), and (116) crystallographic planes, respectively [1]. For the Co/KAO catalyst, XRD patterns of the fresh samples showed reflections at 2θ of 36.8°, 59.3°, and 65.2°, attributed to the (220), (311), (511), and (440) planes of $Co_3O_4$. This phase assignment was further supported by Raman spectroscopy, which revealed a strong and sharp peak at 690 $cm^{-1}$. The XRD reflection at 2θ = 31.3°, also characteristic of $Co_3O_4$, was excluded from NP size calculations due to its overlap with support-related peaks. Although, minor for the KAO support, this issue was even more pronounced in other supports, where deconvolution was challenging and thus reducing the accuracy of NP size estimates. Among the catalysts, $Fe_2O_3$ NPs exhibited the largest average crystallite size at 17.8 nm. $Co_3O_4$ had the smallest average size at 11.6 nm, while NiO and $NiFe_2O_4$ showed intermediate values of 16.2 nm and 13.8 nm, respectively. These values indicate varying degrees of dispersion and suggest different extents of metal-support interaction and thermal stability during calcination.

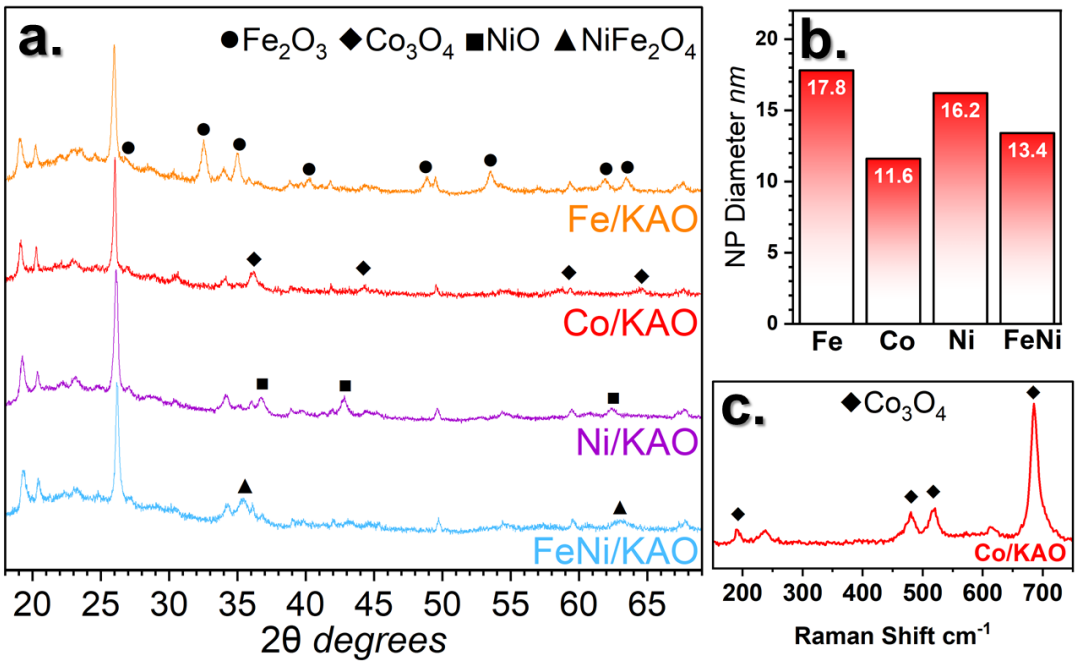


**Figure 5.1**. *Fresh catalyst characterisation for KAO based supports showing (a) XRD patterns with the identified phases and their corresponding peaks, with Fe shown in orange, Co shown in red, Ni shown in purple and FeNi shown in blue (b) average oxide NP size as calculated from the identified XRD peaks and (c) Raman spectra of the Co/KAO catalyst.*

Figure 5.2 displays the XRD patterns of the used KAO-supported catalysts, confirming the successful reduction of all metal oxides to their corresponding metallic phases. Post-reaction, the NP sizes derived from peak broadening indicate that Fe/KAO experienced substantial growth, increasing to 27.9 nm. In contrast, the other metallic species maintained NP sizes comparable to their fresh states, with Co/KAO at 13.0 nm, Ni/KAO at 16.0 nm and FeNi/KAO at 14.6 nm. These results suggest that the KAO support effectively limited sintering, particularly for Co, Ni and FeNi systems. All observed particle sizes post-reduction remained smaller than their counterparts on $Al_2O_3$-supported catalysts, highlighting the superior thermal stabilisation and dispersion properties of the KAO support. This trend is further supported by the TEM-EDX image of the used Co/KAO and Ni/KAO catalyst, which shows a population of well-dispersed NPs, most of which are uniformly distributed and below ~50 nm in diameter. The limited presence of larger agglomerates supports the XRD findings and confirms the stabilising role of KAO in maintaining NP dispersion under reaction conditions.

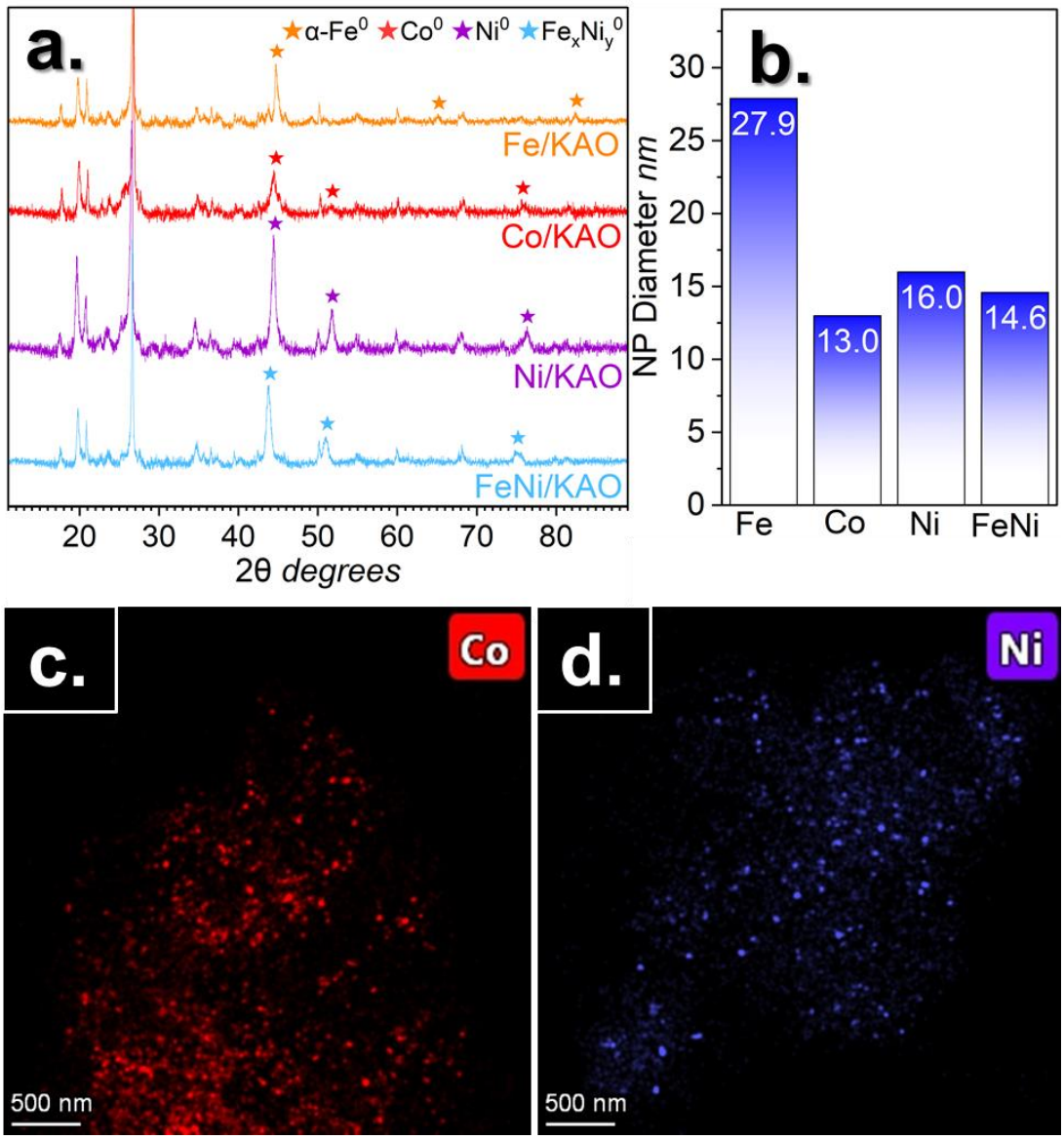


**Figure 5.2.** *Used catalyst characterisation for KAO based supports showing (a) XRD patterns with the identified phases and their corresponding peaks, with Fe shown in orange, Co shown in red, Ni shown in purple and FeNi shown in blue and (b) average metal NP size as calculated from the identified XRD peaks (c) TEM-EDX for the metal sites in the used Co/KAO catalyst and (d) TEM-EDX for the metal sites in the used Ni/KAO catalyst.*

### *5.1.2 MOR-supported*

Figure 5.3 shows the XRD patterns and Raman spectroscopy for the MOR-supported catalysts. The oxide phases detected on the MOR-supported catalysts were consistent with those observed on the KAO-supported catalysts, indicating that the metal oxides formed similarly across different supports. The sharp XRD peaks under

35° 2θ can be attributed to the MOR itself, indicating that the zeolite framework remained intact after calcination for all of the metal/MOR formulations.

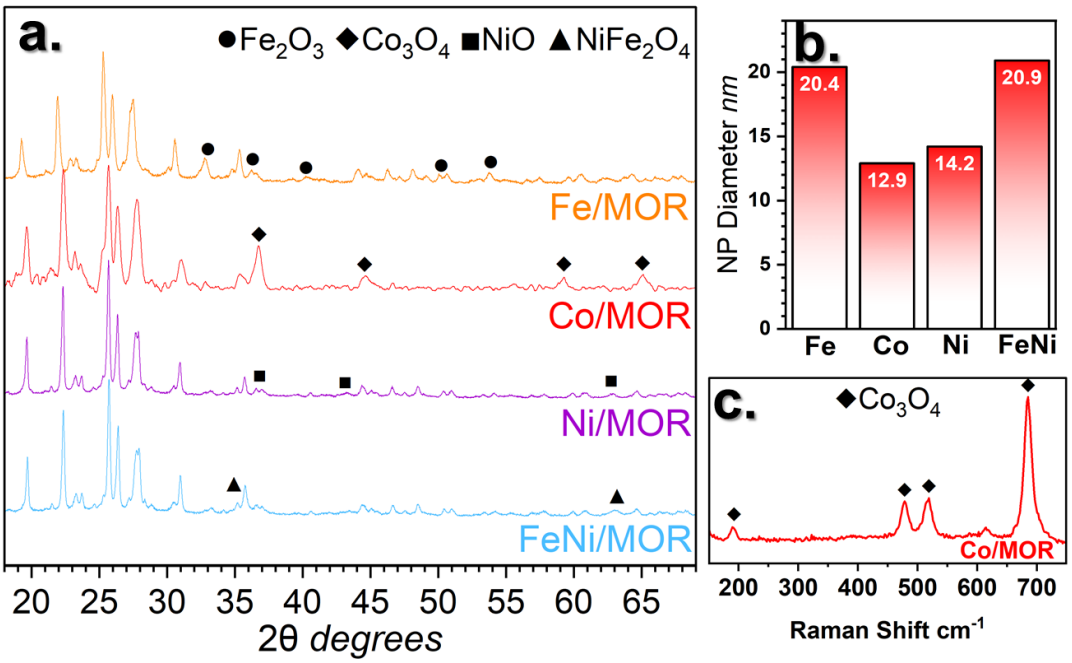


**Figure 5.3.** *Fresh catalyst characterisation for KAO based supports showing (a) XRD patterns with the identified phases and their corresponding peaks, with Fe shown in orange, Co shown in red, Ni shown in purple and FeNi shown in blue (b) average oxide NP size as calculated from the identified XRD peaks and (c) Raman spectra of the Co/KAO catalyst.*

In terms of crystallite size, the MOR-supported catalysts generally exhibited slightly larger oxide NPs than their KAO counterparts. Fe oxides measured at 20.4 nm, Co at 12.9 nm, and FeNi at 20.9 nm, suggesting slightly weaker MSI on the MOR framework, which may contribute to increased particle growth during calcination. In contrast, NiO crystallites on the MOR support were slightly smaller at 14.2 nm compared to KAO-supported NiO, indicating that the MOR support may facilitate better dispersion of Ni species. This could be attributed to effective pore uptake and anchoring of Ni precursors within the MOR zeolite structure, enhancing dispersion during calcination.

Figure 5.4 shows the characterisation results of the used MOR-supported catalysts, confirming the complete reduction of metal oxides to their metallic forms. Although, Fe is found to be in a meta-stable gamma phase. FeNi exhibited a decrease in average NP size to 18.5 nm, a change that can be largely attributed to oxygen loss during reduction rather than NP fragmentation. This suggests that FeNi supported on MOR is highly resistant to sintering. In contrast, Ni and Fe showed moderate

increases in particle size to 25.0 nm and 19.1 nm, respectively, indicating a degree of sintering and NP agglomeration. This trend is supported by the TEM-EDX image of Ni/MOR, which reveals several larger NPs up to ~120 nm and distinct Ni-rich regions without significant NPs formation observes. These areas likely correspond to Ni species that remain encapsulated within the MOR framework, with these entrapped particles presumed to be largely inactive for CNM growth.

Co/MOR showed a more favourable distribution of small-diameter NPs, with an average XRD-derived size of 13.4 nm, notably smaller than that of Ni/MOR. TEM-EDX imaging further confirms this, showing a more uniform distribution of small NPs, with agglomerates rarely exceeding 60 nm. Unlike Ni/MOR, Co/MOR lacked the large regions devoid of NP formation. This may be attributed to partial collapse of the MOR framework during calcination and reaction, as indicated by the lack of sharp XRD peaks below ~35° 2θ. In contrast, the MOR framework remained intact for the other metal species, indicating that the metal species can play a role in framework stability. Indeed, $Ni^{2+}$ is known to anchor within zeolite channels, stabilising the porous structure [2]. his stabilisation effect limits framework collapse and leads to the partial encapsulation of Ni species. Conversely, due to the collapse of the Co/MOR framework, exsolution to form well-dispersed surface NPs occurs.

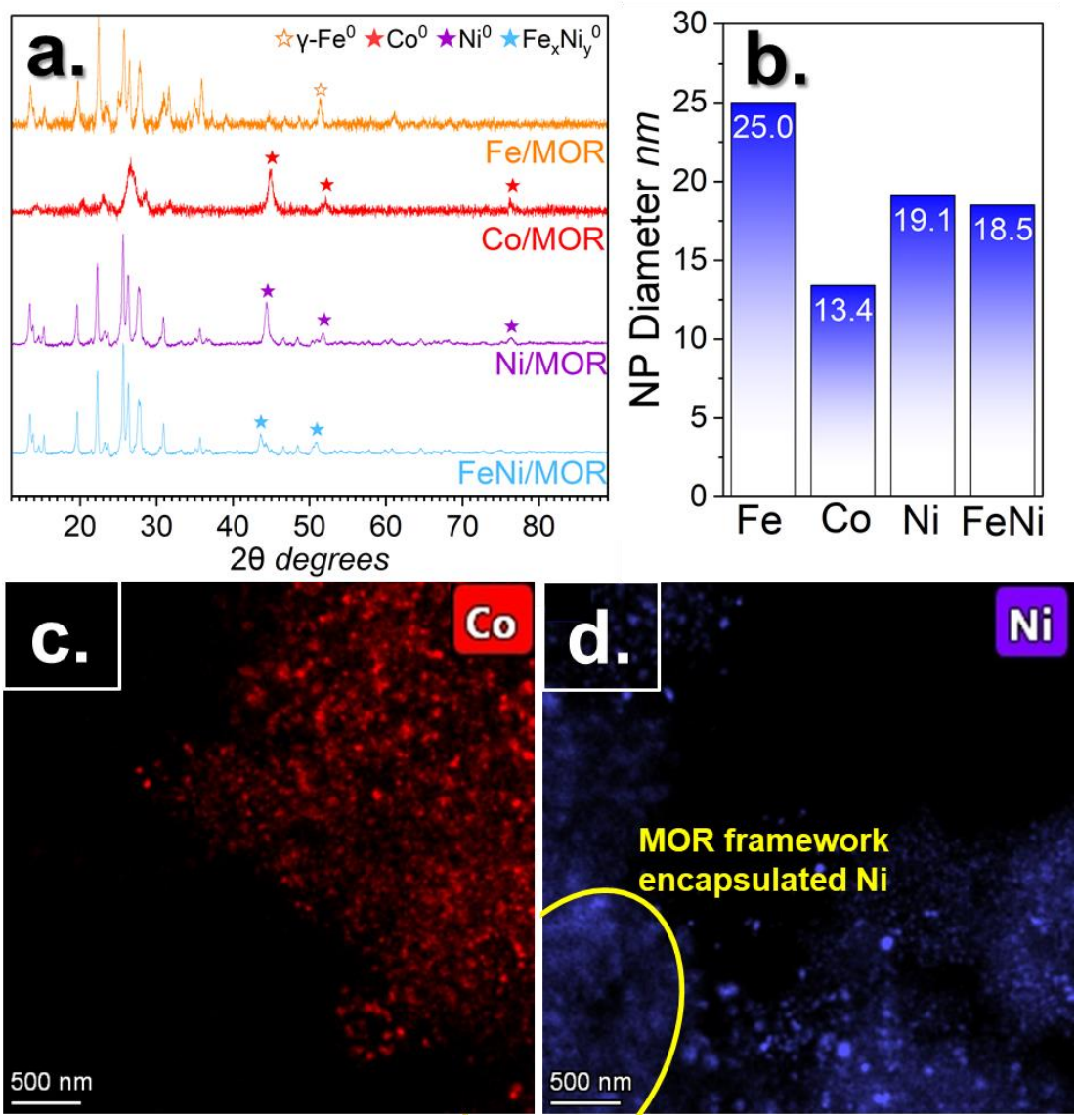


**Figure 5.4.** *Used catalyst characterisation for MOR based supports showing (a) XRD patterns with the identified phases and their corresponding peaks, with Fe shown in orange, Co shown in red, Ni shown in purple and FeNi shown in blue, (b) average metal NP size as calculated from the identified XRD peaks (c) TEM-EDX image showing the Co distribution on the MOR support and (d) TEM-EDX showing the Ni distribution on the MOR support.*

### *5.1.3 FAU-supported*

Figure 5.5 shows the characterisation of the fresh catalysts supported on FAU, with primarily the same phases observed. A difference was the FeNi/FAU catalyst exhibited features characteristic of both NiO and a mixed oxide spinel phase, likely $NiFe_2O_4$, as observed in other supports. XRD peaks observed primarily below 35° 2θ

were attributed to the FAU zeolite framework, confirming that the zeolite structure remained intact after calcination.

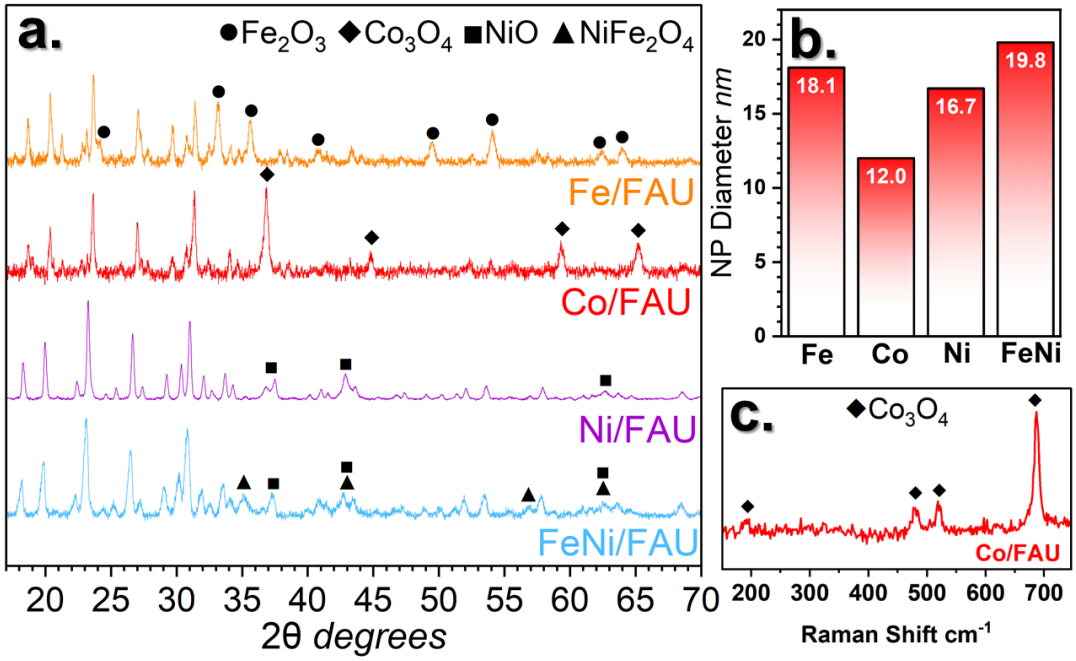


**Figure 5.5.** *Fresh catalyst characterisation for KAO based supports showing (a) XRD patterns with the identified phases and their corresponding peaks, with Fe shown in orange, Co shown in red, Ni shown in purple and FeNi shown in blue (b) average oxide NP size as calculated from the identified XRD peaks and (c) Raman spectra of the Co/KAO catalyst.*

Overall, the average oxide NP sizes on FAU-supported catalysts were intermediate between those observed on KAO and MOR., with the NP sizes found to be 18.1 nm for $Fe_2O_3$, 12.0 nm for $Co_3O_4$ NiO at 16.7 and 19.8nm for FeNi oxides. This suggests moderate metal–support interaction strength on FAU, sufficient to limit excessive sintering while not achieving the high dispersion observed with KAO.

Figure 5.6 shows the characterisation results of the used FAU-supported catalysts. Complete reduction of the metal oxides was again observed. However, in the case of iron, the presence of γ-Fe was detected, suggesting partial transformation to a metastable metallic phase. he particle size increased significantly from 18.1 nm in the oxide form to 28.1 nm post-reduction, indicating sintering. Ni also showed notable growth, increasing from 16.7 nm to 20.2 nm, with Co minimal size increase, rising only from 12.0 nm to 15.5 nm.

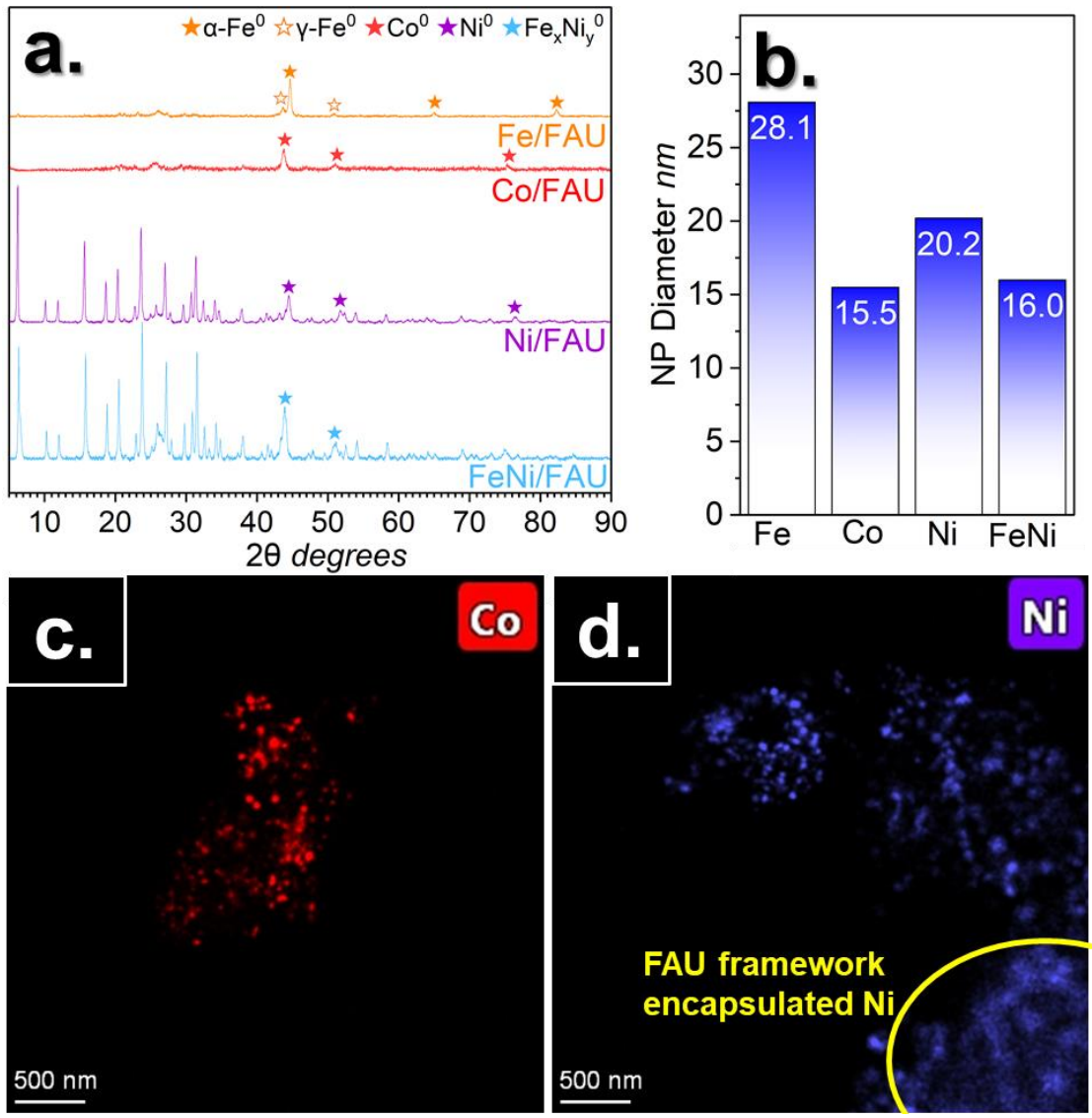


**Figure 5.6.** *Used catalyst characterisation for FAU based supports showing (a) XRD patterns with the identified phases and their corresponding peaks, with Fe shown in orange, Co shown in red, Ni shown in purple and FeNi shown in blue (b) average metal NP size as calculated from the identified XRD peaks (c) TEM-EDX image showing the Co distribution on the MOR support and (d) TEM-EDX showing the Ni distribution on the MOR support.*

As with the MOR-supported system, the Ni/FAU catalyst exhibited regions of framework-encapsulated nickel, whereas such encapsulation was not observed for Co/FAU. This difference is attributed to structural collapse of the FAU framework in the Co- and Fe-containing catalysts, while the Ni-containing systems retained their zeolitic structure. This observation reinforces the known ability of $Ni^{2+}$ to anchor within zeolite channels and stabilise the porous framework [2].

Despite the presence of some larger Ni particles, the Ni/FAU catalyst exhibited a good distribution of spherical, mid-sized NPs below ~50 nm. In comparison, Co NPs were generally slightly larger, with several exceeding ~70 nm, though Co/FAU also showed a higher concentration of small NPs. Overall, the Co distribution on FAU was less favourable than on MOR, while the Ni/FAU system appeared to achieve better dispersion in certain regions relative to Ni/MOR. These findings suggest that the support's framework integrity and MSI influence NP formation, stability and dispersion.

## 5.2 Conversion and Quality

The conversion and quality of the carbon materials deposited on each of the catalysts was assessed. This allowed for comparation between metal-support pairing to be made to determine the most promising catalyst formulations.

### *5.2.1 KAO-supported*

The catalytic performance of KAO-supported transition metals was assessed based on CNM conversion and structural quality, with the conversions result from TPO and the defect density calculated from Raman shown in Figure 5.7. Among the KAO-supported catalyst, Co/KAO produced the highest carbon conversion at 20.0%, although also had the highest D/G ratio of 1.03, indicates efficient catalytic activity but fairly low quality of the resulting carbon. This outperformed its $Al_2O_3$ supported counterpart in terms of conversion, which showed a slightly lower conversion of 17.9%, but at the cost of a higher defect density compared to D/G ratio of 0.59 for alumina. Although, as discussed in the alumina section the defect density and carbon morphology are highly dependent, therefore this may not be a fair direct comparation. Notably, the Co/KAO catalyst, which had the smallest NPs post-reduction supporting the strong correlation between small, well-dispersed NPs and catalytic performance.

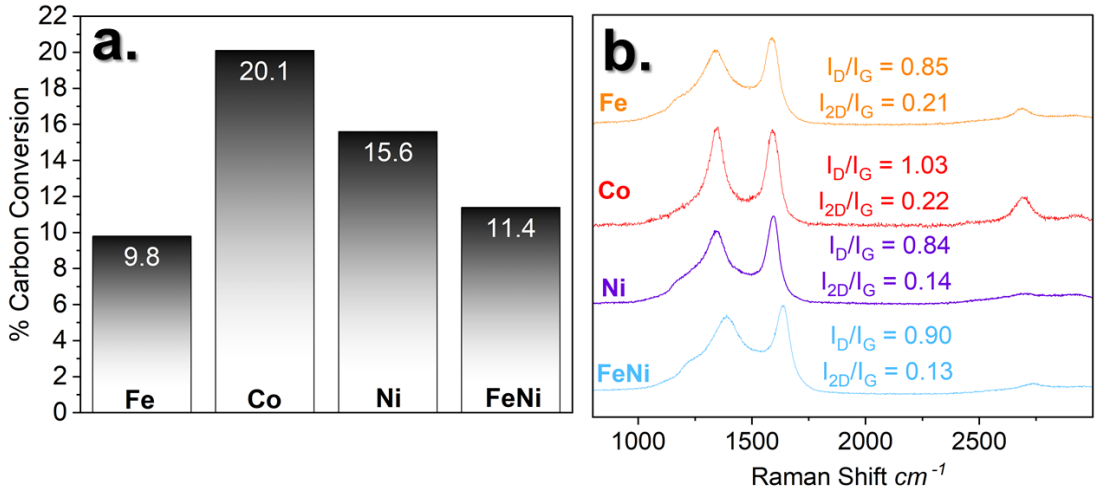


**Figure 5.7.** *The carbon conversion performance of the different KAO supported catalysts showing (a) the conversions as percentage conversion of the carbon in the PE feedstock and (b) the Raman spectra of Fe/KAO in orange, Co/KAO in red, Ni/KAO in purple and FeNi/KAO in blue.*

This Ni was found to be the second most effective metal with KAO, producing a conversion of 15.6%, with a D/G ratio of approximately 0.85, Ni/KAO outperforming Ni/$Al_2O_3$ in both these metrics, with a particularly improvement in graphitic quality. This suggests that KAO may help stabilise Ni particles or slow carbon precipitation rates, reducing disorder. The FeNi/KAO catalyst delivered a lower conversion of 11.4% with the highest D/G ratio (0.90) in this group, suggesting significant defect content. A marginal increase in conversion, with effectively the same defect density as FeNi/$Al_2O_3$. As with the alumina catalysts, Fe/KAO displayed the lowest conversion with just 9.8% carbon conversion, consistent with the excessive particle growth compared to the other metals, reducing active surface area and catalytic effectiveness. Although this was a reasonable improvement compared to Fe/$Al_2O_3$, which could be attributed to better Fe dispersion or reduced sintering on the KAO surface as seen by the reduction in $Fe^0$ NP size. Fe/$Al_2O_3$ also produced a higher quality carbon, although as with Co/$Al_2O_3$ the encapsulate core-shell Fe@CNO structure is likely less prone to defect formation compared to filamentous carbon.

### 5.2.2 MOR-supported

The analysis of catalytic performance of MOR-supported catalysts is shown in Figure 5.8.

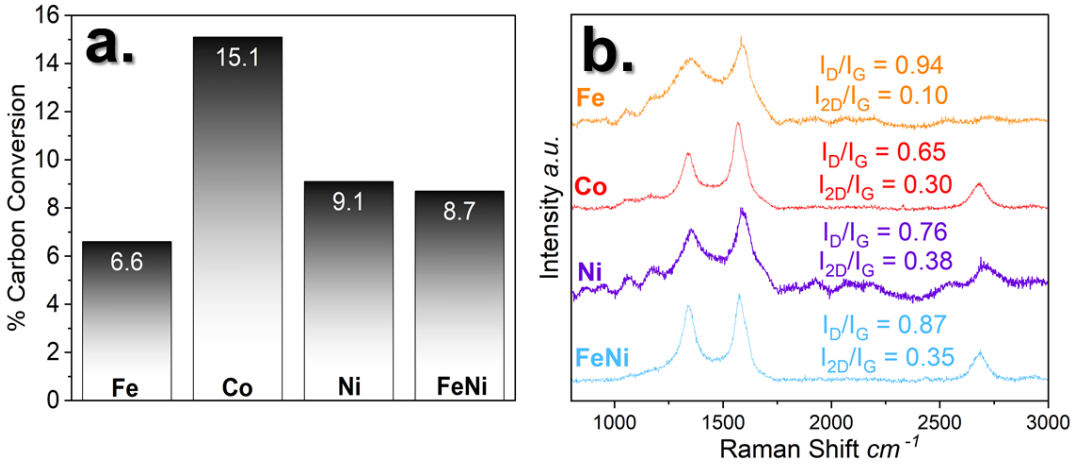


**Figure 5.8.** *The carbon conversion performance of the different MOR supported catalysts showing (a) the conversions as percentage conversion of the carbon in the PE feedstock and (b) the Raman spectra of Fe/MOR in orange, Co/MOR in red, Ni/MOR in purple and FeNi/MOR in blue.*

Fe/MOR was the least productive among the MOR-supported catalysts, generating just 6.6 percent carbon, with a moderate D/G ratio of 0.84, similarly to the other support materials. The Fe/MOR catalyst had lower conversion than Fe/KAO, but higher graphitic quality, and vice-versa for Fe/Al2O3, indicating intermediate performance. Ni/MOR offered a conversion improvement over Fe/MOR with a 9.1% carbon conversion. Although, this was significantly lower than Ni/KAO and Ni/$Al_2O_3$. However, its D/G ratio of 0.76 indicates that the carbon formed was of higher quality than that from both kaolin and alumina-supported nickel systems. This suggests that although mordenite may suppress disordered growth forms, which although decreases overall productivity offers higher selectivity towards high quality CNMs.

FeNi/MOR offered a slight improvement over Fe/MOR in terms of conversion with a value of 8.7% carbon conversion, although with a lower value for conversion than Ni/MOR. Additionally a decrease in graphitic quality compared to both these catalysts was observed, with a D/G ratio of 0.87. This again emphasised the lack of the expected synergistic effects of FeNi-based catalysts. Co/MOR demonstrated the highest CNM conversion among the MOR-supported systems, at 15.1%, along with a notably low D/G ratio of 0.65, indicating the formation of structurally ordered CNMs. This high performance aligns with the high NP dispersion and low diameter found for

Co/MOR. Although, compared to Co/KAO, Co/MOR resulted in a decrease in conversions but a large enhancement in graphic quality. Similarly, to Ni/MOR, this suggests a favourability of high-quality CNMs over less structured deposits, indicating a high potential for Co/MOR based catalysts.

### *5.2.3 FAU-supported*

Figure 5.9 shows the catalytic performance of the FAU supported catalysts.

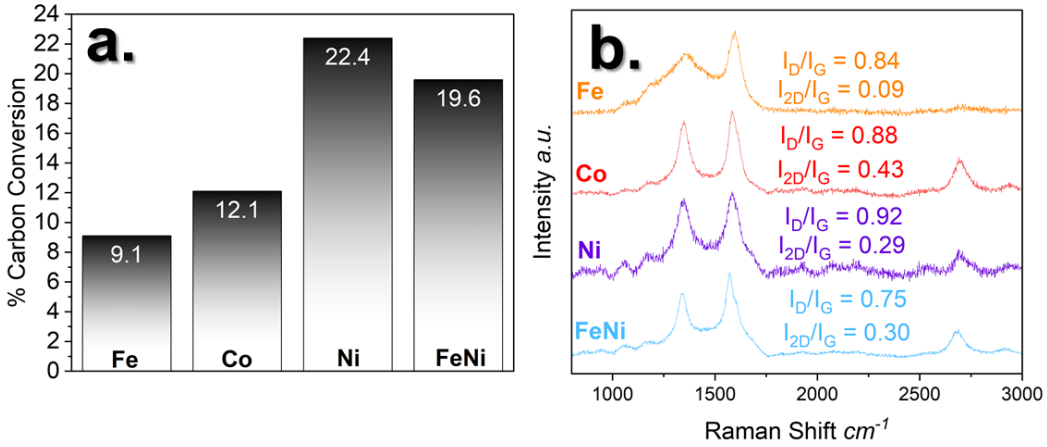


**Figure 5.9.** *The carbon conversion performance of the different FAU supported catalysts showing (a) the conversions as percentage conversion of the carbon in the PE feedstock and (b) the Raman spectra of Fe/FAU in orange, Co/FAU in red, Ni/FAU in purple and FeNi/FAU in blue.*

The Fe/FAU catalyst produced 9.1 percent carbon with a D/G ratio of 0.72. This places its conversion higher than Fe on alumina and mordenite, and close to Fe on kaolinite. The D/G ratio suggests a moderate level of disorder in the carbon material. These results are consistent with the other Fe-based catalysts, indicating the poor performance and tendency for deactivation. Conversely, Ni/FAU catalyst exhibited the highest CNM conversion of any of the metal support combination tested in this section, with a carbon conversion percentage of 22.4 percent. Although, the D/G ratio was found to be 0.92, suggesting only a moderate quality of graphitic lattice.

The FeNi/FAU catalyst generated 19.6 percent carbon, with a D/G ratio of 0.75. This represents a substantial improvement in conversion compared to the same bimetallic system on alumina, kaolinite, and mordenite. The D/G ratio indicates a moderate level of structural disorder, slightly higher than Ni/FAU, suggesting that the addition of Fe had a detrimental effect, again indicating the lack of synergistic effects found in this work. The Co/FAU catalyst produced 12.1 percent carbon with a D/G ratio of 0.88. While the conversion was moderate compared to Co on other supports, the D/G ratio

was the highest among the FAU-supported group, indicating a higher defect content in the carbon produced. This suggests that cobalt's catalytic behaviour may be less favourable on the FAU framework in terms of structural control, with MOR providing a more effective supporting material.

## 5.3 Carbon Morphology

The carbon morphology deposited on the metal-support combination was investigated by SEM and TEM.

### *5.3.1 KAO-supported*

The SEM images for the KAO supported catalysts are shown in Figure 5.10. The Fe/KAO catalyst was found to display minimal carbon deposition. The SEM image showed large, flat kaolinite-derived alumina platelets with very little surface coverage by carbon. There is an absence of extended carbon networks Spare and short carbon filaments can be seen, with a few small aggregates of spherical carbon. This morphology aligns with the low CNM conversion and indicates weak catalytic activity, likely due to poor Fe NP dispersion or sintering causing limited nucleation sites. The FeNi/KAO catalyst display a slightly higher density of carbon deposit, with some filamentous carbon found in patches, although additionally larger areas of catalyst surface without any carbon deposition.

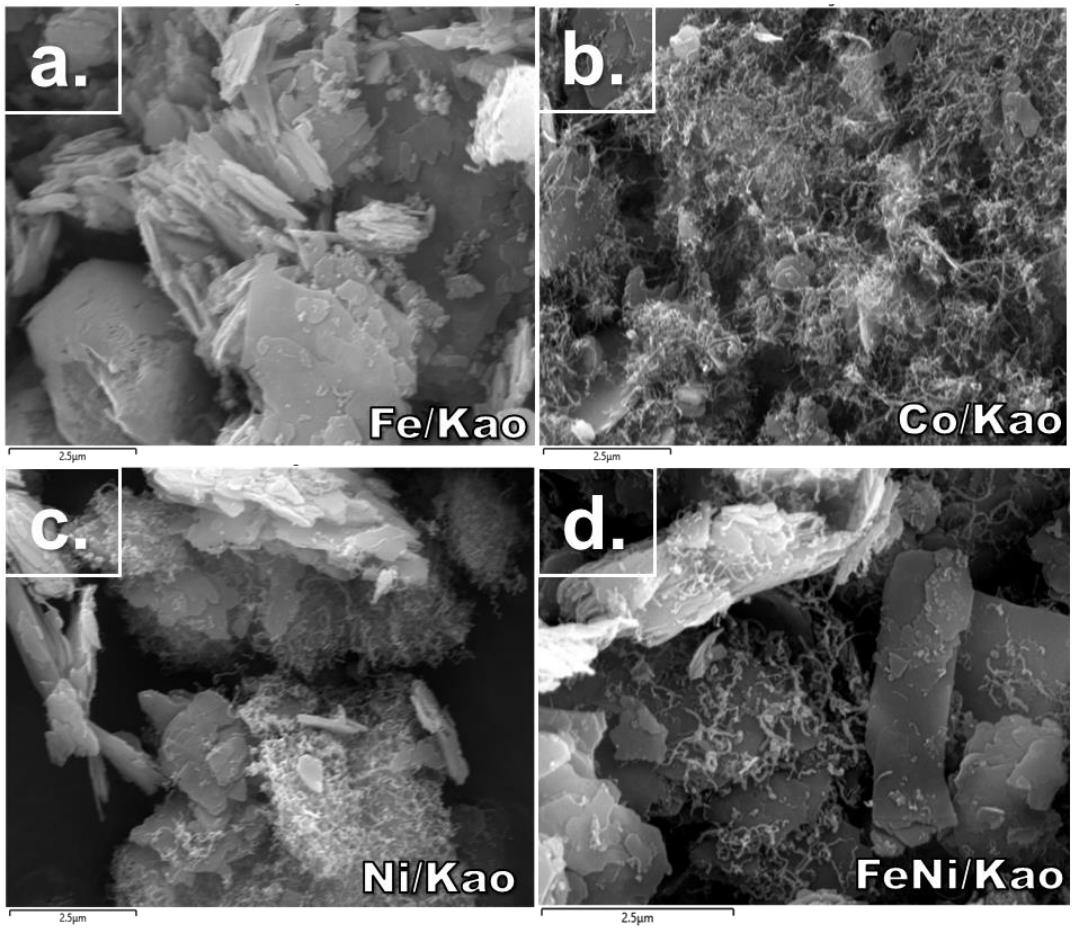


**Figure 5.10.** *SEM images showing the morphology of the carbon deposited on the KAO supported catalysts: (a) Fe/KAO (b) Co/KAO (c) Ni/KAO and (d) FeNi/KAO*

Co/KAO presented the most uniform and extensive carbon growth, and unlike $Co/Al_2O_3$, Co/KAO causes the formation of primarily filamentous carbon. SEM imaging revealed a dense, highly entangled surface-bound filamentous mats, with these carbon networks distributed fairly evenly over the KAO surface. The difference in carbon morphology could is a contributing factor to the difference in graphitic quality between Co/KAO and $Co/Al_2O_3$ catalysts. The consistent coverage of the filaments is indicative of improved cobalt NP dispersion and sustained catalytic activity, which lead to the improved conversions found for Co/KAO over the other catalysts. Figure 5.11 shows the TEM images for the Co/KAO catalyst. The dense tangled mat of CNTs can be seen coating the surface of the catalyst, there are of small dimeter. Co NPs can be seen as part of the entangled mat, indication a tip growth mode was followed for these.

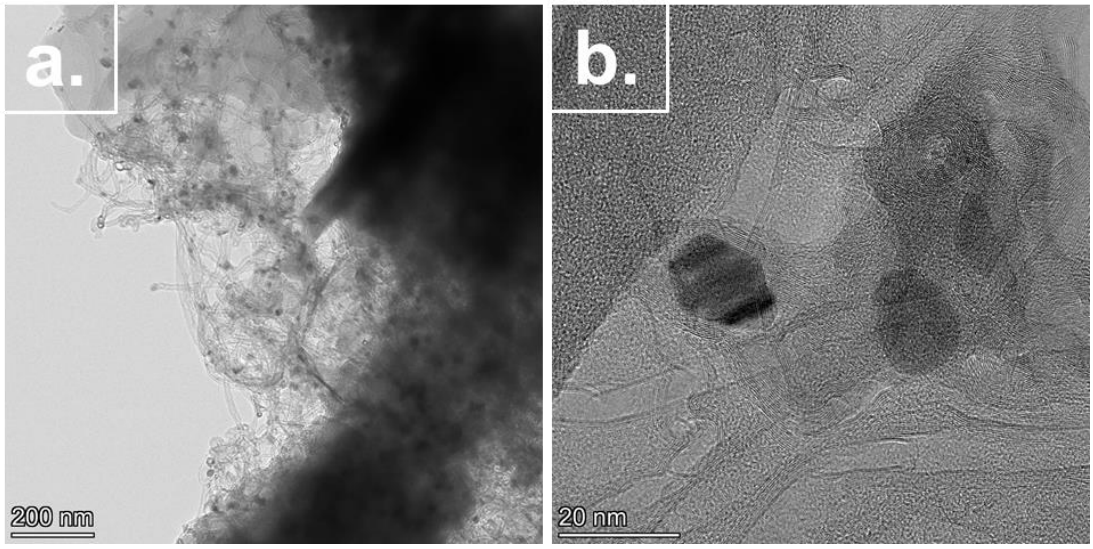


**Figure 5.11.** *TEM images of the Co/MOR catalyst showing (a) the overall bulk structure and (b) arrangement of graphitic walls.*

Ni/KAO exhibited clearly visible dense filamentous mats developing across the support surface, in a similar way to Co/KAO. Although, the Ni catalyst displayed a less uniform carbon network formation, with more KAO surface without filamentous deposits, indicating that Ni/KAO may be slightly more heterogeneous than Co/KAO. This would also explain the slightly lower conversion than Co/KAO found for the Ni/KAO catalyst. Nonetheless, both systems demonstrate that kaolin is an effective support for Ni and Co catalysts, with its layered silicate structure and moderate acidity facilitating NP dispersion and catalytic site exposure.

Figure 5.12 shows the TEM images of the Ni/KAO catalyst. It can be seen that CNTs are present, although they do not extend away from the surface. The tip of a CNT can be observed with Ni NP, indicating that base growth has occurred. Therefore, the strong interaction caused by the Ni/KAO support appears to cause limitation to CNT growth, therefore, the property of Ni/KAO responsible for the well dispersed NPs may also be a major limitation/drawback. This differs from Co/KAO which higher conversion and tip growth-mode prevalence indicates the weaker interaction allow for the higher conversions.

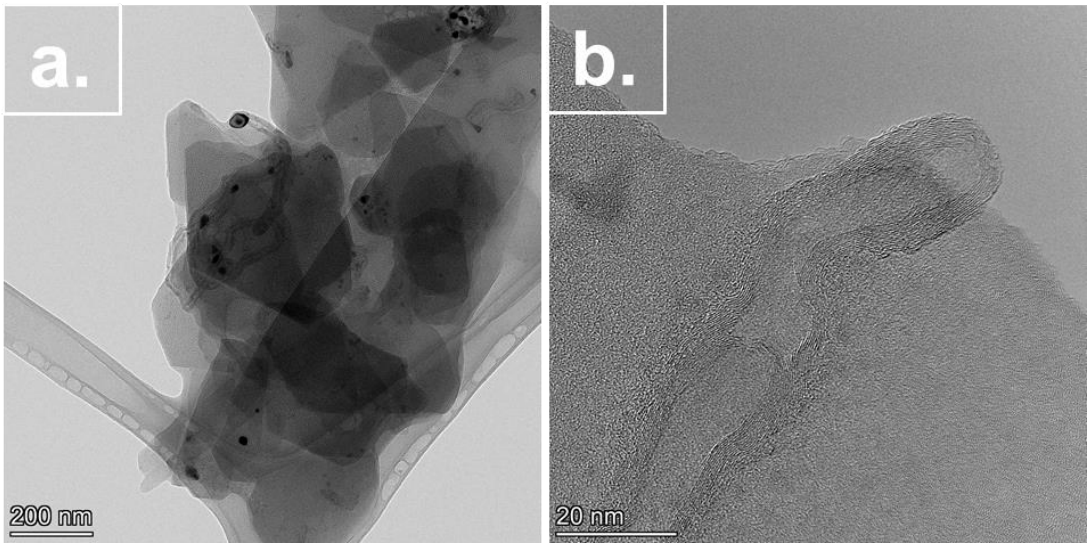


**Figure 5.12.** *TEM images of the Ni/KAO catalyst showing (a) the overall bulk structure and (b) arrangement of graphitic walls.*

### *5.3.2 MOR-supported*

The SEM images for the MOR supported catalysts are shown in Figure 5.13. The Fe/MOR catalyst showed minimal carbon deposition. The SEM image revealed that the surface was largely dominated by the MOR support structure with only isolated carbon patches and scattered. This confirms the low CNM conversion and supports the conclusion that Fe/MOR has poor catalytic activity, likely due to limited NP dispersion or rapid deactivation of Fe species, as observed for the other catalyst species.

The FeNi/MOR sample revealed sparse and uneven filament formation, which were primarily surface bound. While filamentous carbon was observed, much of it appeared isolated or incomplete, with significant portions of the mordenite support still visible. This morphology aligns with the low-to-moderate conversion and relatively high $I_D/I_G$ ratio observed for this catalyst, indicating disordered carbon formation and poor synergy between the bimetallic species. The diameters of these filaments were fairly large ranging broadly from 30 to 60 nm, with lengths generally below 300 nm. This suggests that a fairly high degree of NP agglomeration has occurred.

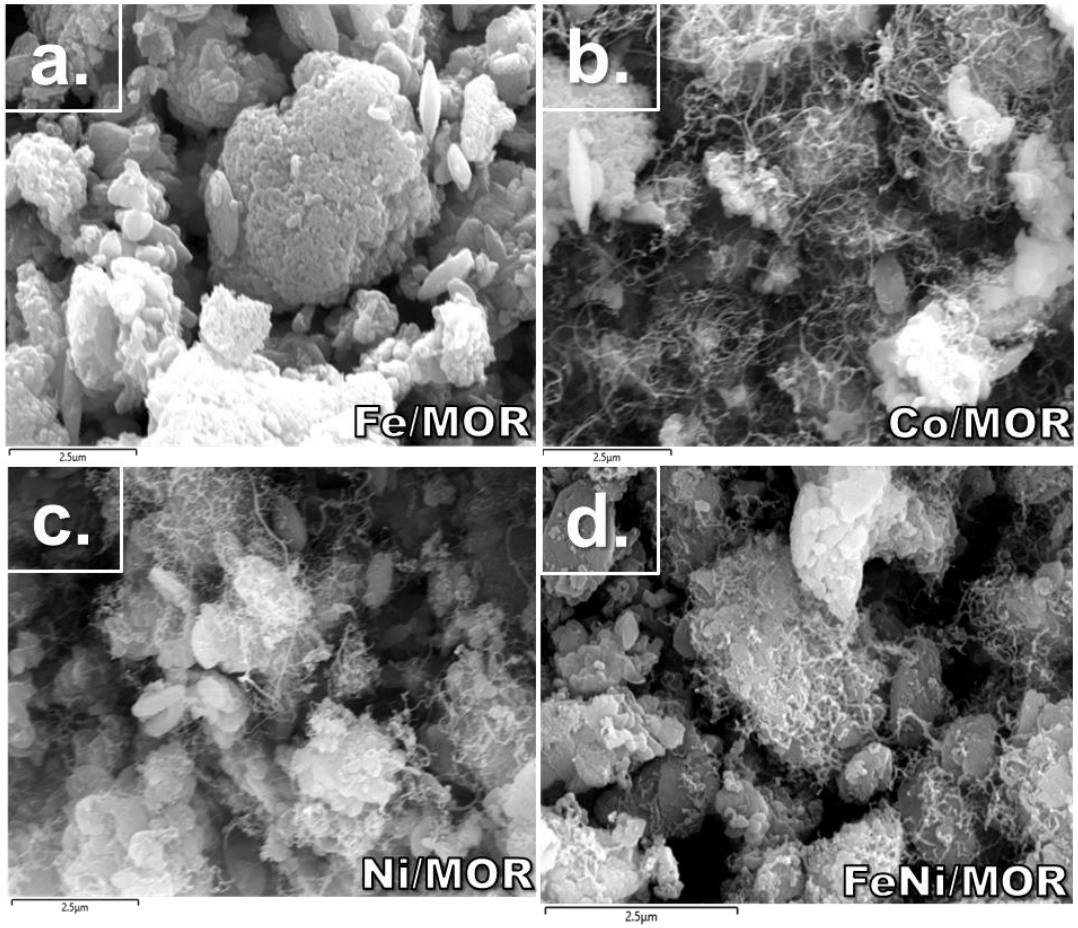


**Figure 5.13.** *SEM images showing the morphology of the carbon deposited on the MOR supported catalysts: showing (a) Fe/MOR (b) Co/MOR (c) Ni/MOR and (d) FeNi/MOR.*

Ni/MOR produced a moderately dense carbon filamentous carbon network, although some areas of the support were only partially covered. This morphology points to heterogeneous NP behaviour, with some regions catalytically active while others remained inactive or deactivated during growth. These were mostly surface bound, although the presence of some surface detached filamentous structures was observed. Although, the filaments appeared somewhat disjointed and irregular, consistent with moderate graphitisation degree. The filaments diameters varied between 25 and 50 nm, with lengths typically around 200 to 400 nm. The TEM results, shown in Figure 5.14 confirmed the formation of both helical and bamboo-like CNTs.

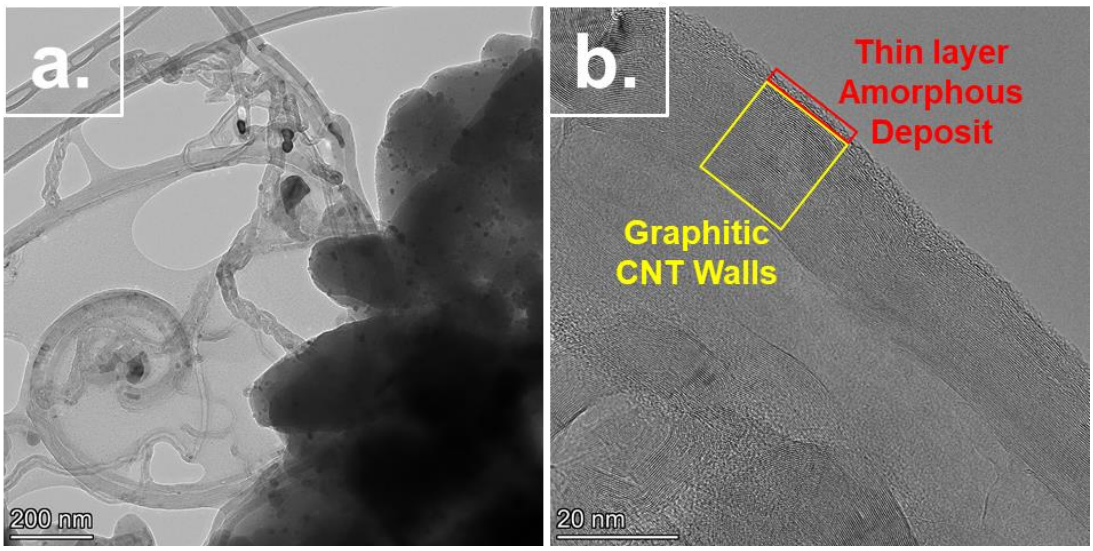


**Figure 5.14.** *TEM images of the Ni/MOR catalyst showing (a) the overall bulk structure and (b) arrangement of graphitic walls.*

In contrast, Co/MOR displayed the densest network of entangled filamentous carbon with the most uniform support coverage, in line with the highest carbon conversion. The filaments had a typical diameter of 20 to 35 nanometres, and were distributed well across the support surface. The high density and homogeneity of the filaments are consistent with a well-dispersed Co phase and strong catalytic activity. A significant proportion of longer filamentous structures in the range of several micrometres and growing isolated from the MOR surface, suggesting a more favourably carbon-support interaction strength than Co/MOR allowing for detachment and further growth of carbon filaments. TEM analysis shows well-formed, long, and thin CNTs with predominantly graphitic walls are abundant, as shown in Figure 5.15a. Although, some CNTs also display significant amorphous carbon deposition on their outer layers, as seen in Figure 5.15b. This may be attributed to the reduced catalytic activity of MOR in the Co/MOR catalyst system, potentially due to framework collapse and the formation of exsolved surface NPs. These structural and catalytic changes allow for the direct contact of CNTs with larger hydrocarbon precursor molecules, potentially allowing for disordered carbon deposition and therefore the formation of the observed outer amorphous carbon layers.

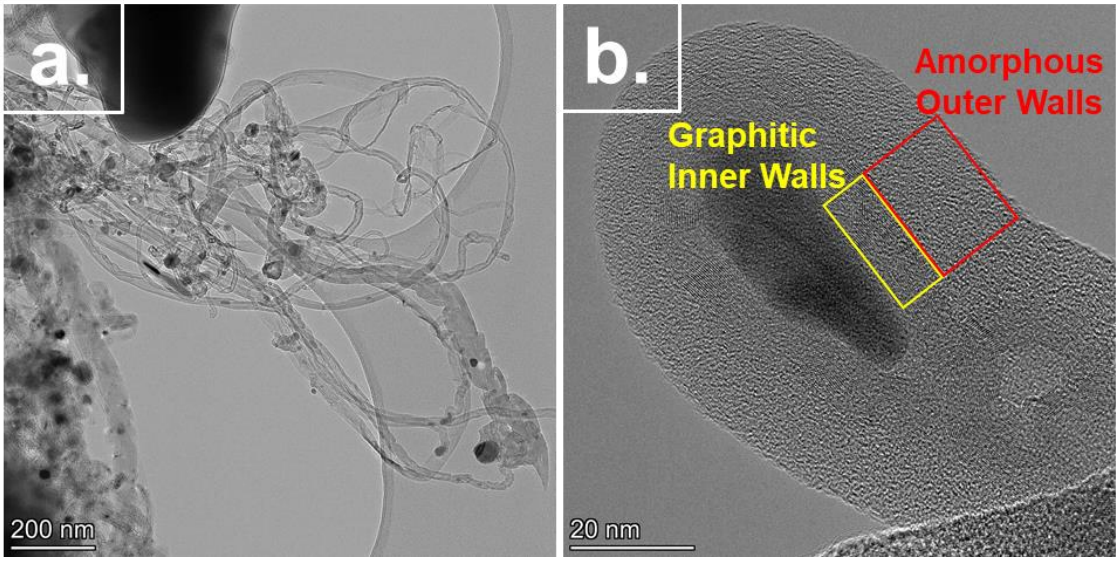


**Figure 5.15.** *TEM images of the Co/MOR catalyst showing (a) the overall bulk structure and (b) arrangement of graphitic walls.*

### *5.3.3 FAU-supported*

The SEM images for the FAU supported catalyst are shown in Figure 5.16. The Fe/FAU catalyst showed limited carbon growth, with sparse, stubby filaments present across the zeolite surface. Filaments were typically short, with lengths under 300 nanometres and with large diameters of 30-50 nm. The fragmented and uneven distribution of filaments corresponds with the modest conversion and moderate $I_D/I_G$ ratio, indicating insufficient Fe dispersion or early catalyst deactivation as with the other supports. FeNi/FAU also showed extensive filament coverage, with many filaments displaying curled or entangled morphologies. Diameters varied from 25 to 40 nanometres, with filament lengths commonly ranging from 400 nm to just over 1 micron. Although the filaments were slightly more disordered than those from Ni/FAU, the high density and continuity of carbon growth reinforce the strong catalytic performance and relatively low defect density observed.

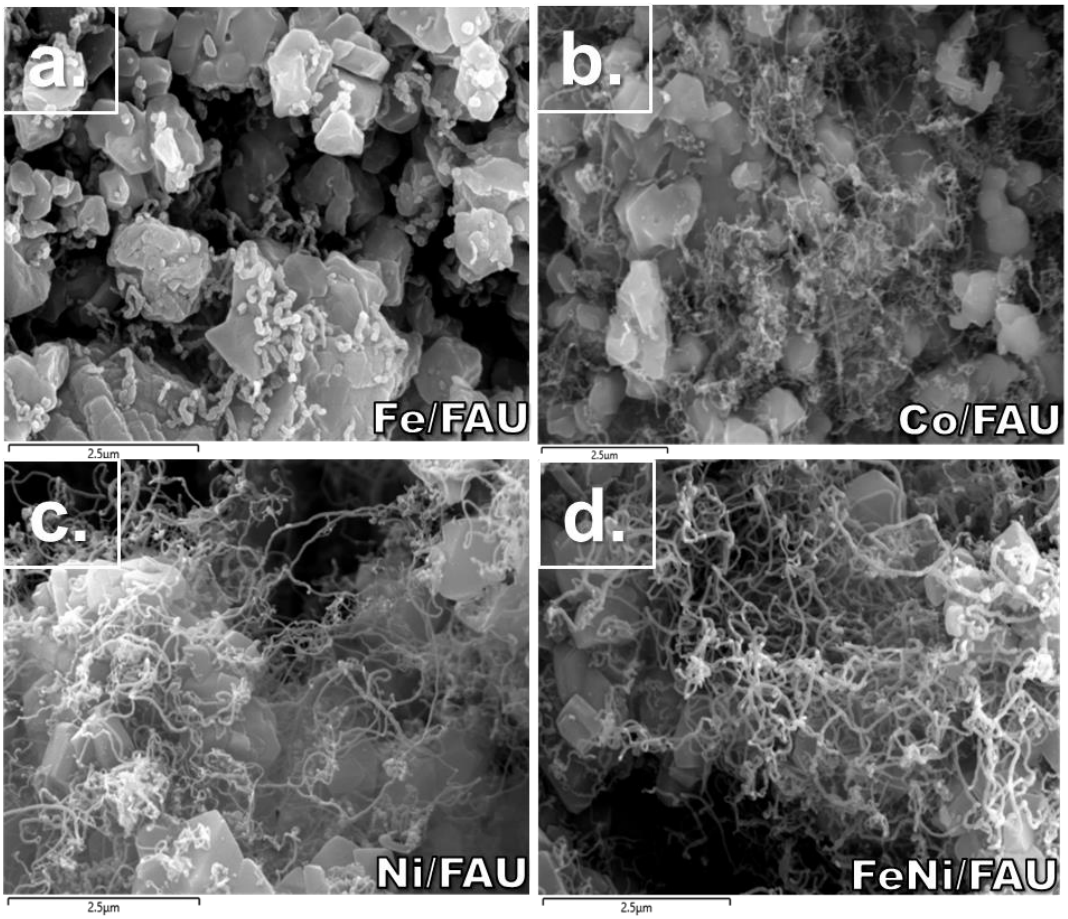


**Figure 5.16.** *SEM images showing the morphology of the carbon deposited on the FAU supported catalysts: showing (a) Fe/FAU (b) Co/FAU (c) Ni/FAU and (d) FeNi/FAU.*

Ni/FAU exhibited a highly developed, interconnected network of filamentous carbon. Filament diameters were generally consistent between 20 and 30 nanometres, with lengths extending up to several microns. Although, some shorter, higher diameter surface bound filaments could also be observed. These long, thin and well-aligned structures are indicative of effective NP dispersion and sustained catalytic activity, consistent with this sample's exceptional carbon conversion and low D/G ratio. The TEM analysis of the Ni/FAU catalysts shows a high quantity of with diameters around ~25nm or smaller, along with larger diameter filamentous structures at around 75 nm. The graphitic in some of the CNTs were found to display a fishbone morphology, with their alignment not parallel to the CNT axis.

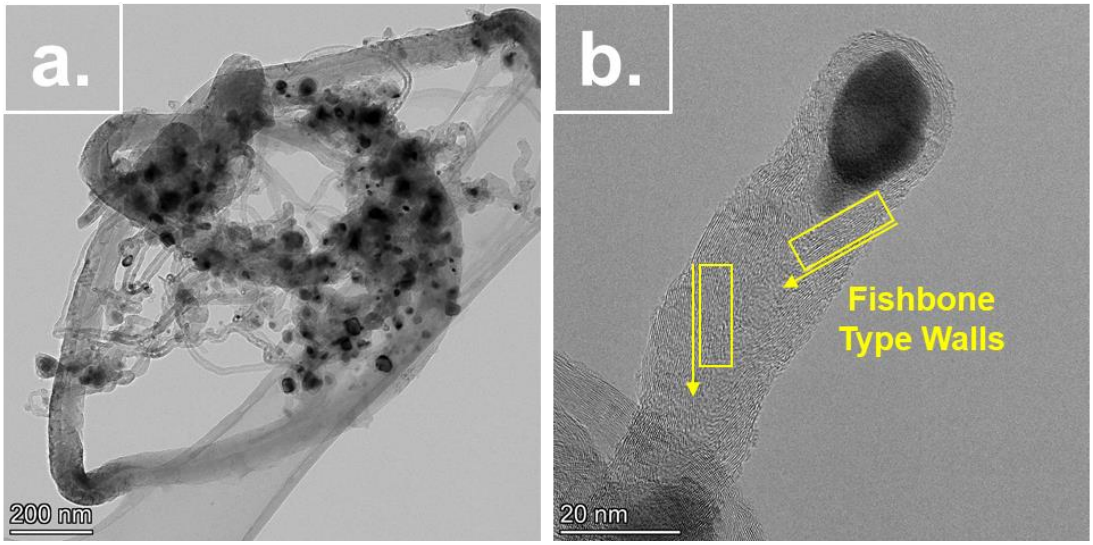


**Figure 5.17.** *TEM images of the Ni/FAU catalyst showing (a) the overall bulk structure and (b) arrangement of graphitic walls.*

In the case of Co/FAU, filament coverage was moderate, with carbon deposits less uniformly distributed across the surface. Some surface detached filaments exhibited diameters from 25 to 45 nanometres and lengths mostly between 300 and 600 nanometres. Whereas, shorter filaments made up tangled surface-bound mat formations, suggesting an inability to nucleate growth away from the catalyst, with the more disordered structure of these in line with Co/FAU having the highest D/G ratio among the FAU-supported catalysts. The visible areas of bare support and relatively short filaments suggest uneven catalytic activity with inactive regions, which aligns well with the lower conversion compared to the Ni-based FAU catalysts.

The TEM analysis for the Co/FAU catalyst is show in Figure 5.18 shows a tangled mass of carbon structures, with some CNTs formed. Additionally, the walls of these CNTs also displayed a fishbone morphology, suggesting that the uneven growth. Although, the amorphous carbon layers observed in the MOR-based catalysts were notably absent in the FAU samples. This difference can likely be attributed to the higher porosity and superior hydrocarbon cracking ability of the FAU support These properties facilitate the generation of lower molecular weight carbon precursors, thereby modulating the carbon supply and preventing the secondary amorphous phase formation seen in the MOR catalysts.

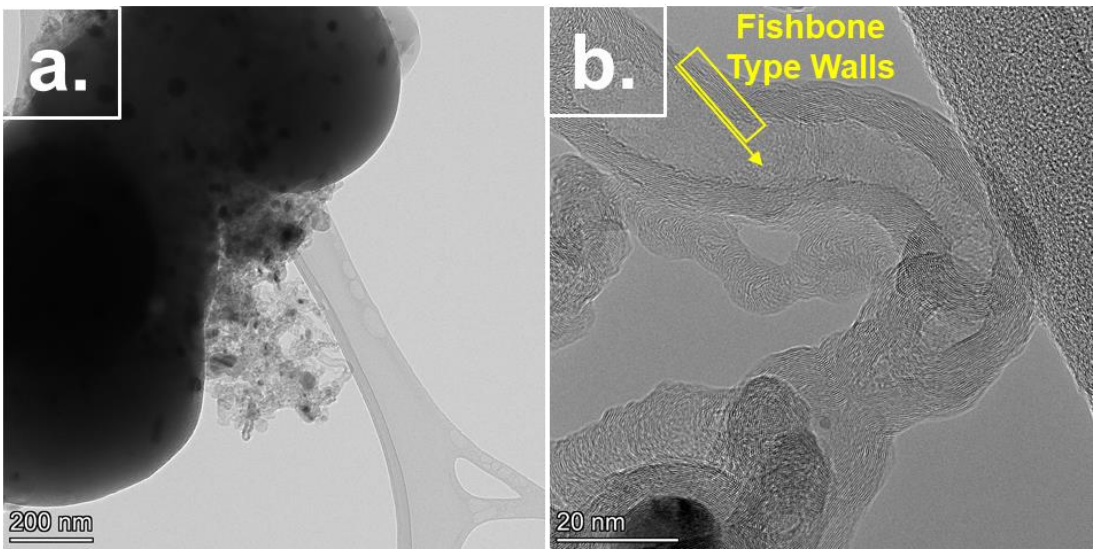


**Figure 5.18.** *TEM images of the Co/FAU catalyst showing (a) the overall bulk structure and (b) arrangement of graphitic walls.*

## 5.4 Conclusion

The catalytic performance of transition metal catalysts in CNM synthesis is governed by a complex interplay between the active metal species and the support material. Across the catalyst systems tested, substantial variation was observed in carbon conversion, defect density and morphology. These variations underscore the critical role of metal–support interactions in determining catalytic activity, stability, and product quality. KAO generally displayed the lowest performance. despite facilitating well dispersed NPs, the strong MSI and carbon-support interactions hindered CNT nucleation especially away from the catalyst resulting in surface bound, sort base grown CNTs.

FAU facilitated high conversions and extensive filament growth, particularly for Ni and FeNi systems. The Ni/FAU and FeNi/FAU framework remained structurally sound, whereas Fe/FAU and Co/FAU experienced framework collapse, indicating that Nis ability to stabilise the zeolite framework improves the performance of FAU. Indeed, the large surface area, three-dimensional porous framework, and high hydrocarbon cracking capacity of FAU together supported the formation of well-dispersed NPs and low-molecular-weight carbon precursors. Although, FAU also induced fishbone-type CNT structures, characterised by graphitic walls misaligned with the tube axis, likely due to localised carbon flux gradients and uneven growth rates at the NP surface.

MOR demonstrated a strong synergistic effect with cobalt, promoting the formation of dense filamentous networks. As the Co/MOR catalysts underwent unlike the other it

can be assumed that MOR surface-based growth is preferred, with the one-dimensional pore structure not allowing the same levels of carbon diffusion as FAU. Although, this restrictive framework allows Co NPs being shaped by the MOR, leading to well dispersed NP and thus high quality CNMs.

Overall, the findings emphasise that favourable combination of the metal and the support is required for designing high-performance catalysts for CNM synthesis. Among the combinations studied, Co/KAO, Co/MOR, Ni/FAU emerged as the most promising for high conversions and Ni/KAO, Co/MOR and FeNi/FAU for high quality. FeNi/FAU whist demonstrating high performance and small NP size, still did not exhibit the degree of bimetallic synergistic effects over monometallic seen in literature, suggesting there is still issues with achieving these effects in a one-stage system.

Co/MOR is selected for further development in the next chapter, due to displaying high performance in conversion, quality and morphology, and displaying a good balance between all of these traits. Although Ni/FAU displayed the highest conversion, the higher graphic quality and good structural uniformity of the Co/MOR was considered to indicate a more balanced catalyst. The selection of Ni/FAU or FeNi/FAU for further testing could also be justified, with both displaying high enough potential to be considered for further catalytic improvement work.

# References

[1] E. Paterson, “The Iron Oxides. Structure, Properties, Reactions, Occurrences and Uses,” *Clay Miner.*, vol. 34, no. 1, 1999, doi: 10.1180/claymin.1999.034.1.20.

[2] Y. L. H. S. L. Z. Y. W. Y. H. L. M. J. H. A. T. N. M. D. J. Z. L. Z. W. & F. P.-G. Junyan Zhang, “Tuning metal-support interactions in nickel–zeolite catalysts leads to enhanced stability during dry reforming of methane,” *Nat. Commun.*, Oct. 2024.

# Chapter 6

# Evaluation of Catalyst Development Approaches

In this chapter, the effect of different catalyst development strategies will be investigated. The effect of calcination temperature, preparation method and additionally supporting metal species are evaluated. Their role in determining the dispersion of metal sites within the zeolite framework, and the stability of the zeolite framework itself, are investigated. These factors influence catalytic properties such as nanoparticle stability, dispersion and the relative distribution of metal on the external surface compared with within the zeolite pores. As a result, preparation strongly impacts both the conversion and quality of the carbon nanomaterials (CNMs) produced. The development of Co/MOR based catalysts is the focus of this chapter, with several modification strategies evaluated. These include varying the calcination temperature, the use of chelating agents, hydrothermal synthesis of the zeolite and the incorporation of secondary metals.

## 6.1 Effect of Calcination temperature

### *6.1.1 Fresh and Used Catalyst Characterisation*

Figure 6.1 shows the fresh catalysts treated at the high calcination temperature used in the previous chapters, alongside those prepared at a lower calcination temperature. The more pronounced difference between the XRD patterns is in the range of below ~35°. The peaks in this range, which are associated with the zeolite framework, can be observed for the used catalyst prepared at 550 °C calcination temperature, indicating the preservation of the zeolite framework. Whereas, as covered in the previous results chapter, a framework collapse effect is observed with the used Co/MOR catalyst prepared at 800 °C calcination temperature. Since the CNM growth conditions are identical, this difference in behaviour can be attributed to framework damage and instability caused during calcination.

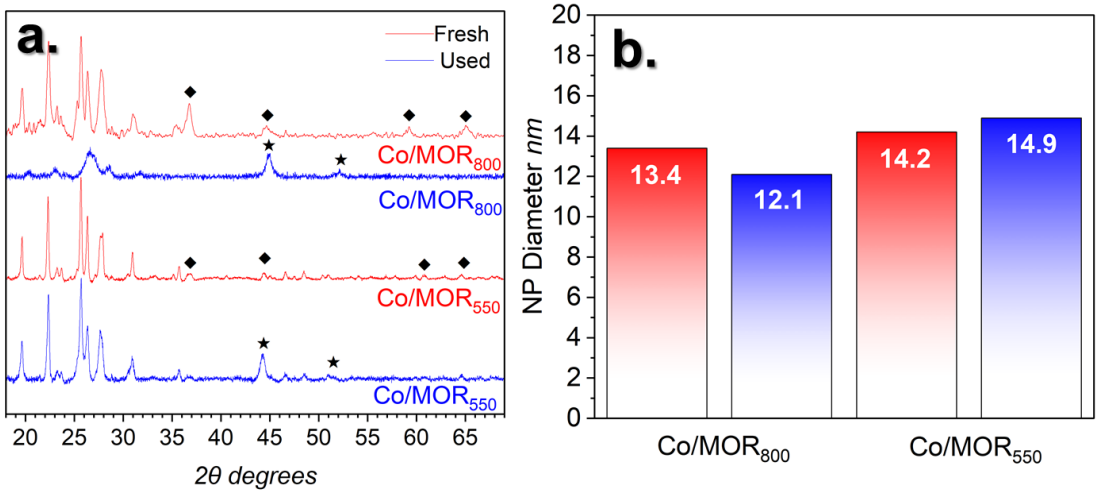


**Figure 6.1.** *Fresh and used catalyst characterisation prepared using different calcination temperatures of 800 °C and 550 °C, (a) showing the NP diameters and (b) showing the XRD patterns, with fresh catalysts shown in red and used catalysts shown in blue.*

In general, it is the case that higher calcination temperatures can lead to framework collapse through oxidative damage due to the air environment used during calcination[1] [2]. This causes the $AlO_4$ sites in the zeolite to become thermally unstable, which can lead to the hydrolysis of Al-O-Si bridges. The presence of metal in the system can further these damaging effects, with excessive Co uptake particularly known to cause zeolite damage [2]. Therefore, it is proposed that these effects were enough to cause sufficient framework damage during high temperature calcination, that framework collapse occurs during the reducing conditions experienced during CNM growth. In general, the reduction of a zeolite after calcination

can further the damage caused during calcination. Reduction can lead to further dealumination, with the hydrogen gas forming water and heat, which can result in hydrolysis. Furthermore, the reduction of metal sites incorporated within the zeolite framework can cause instability, with these sites more prevalent with high calcination temperature preparation. The reduction of metal oxide NP causes changes in the diameter and distribution. Shrinkage of encapsulated oxide NPs can cause void space, and sintering of metal NPs can cause framework stress, both resulting in destabilisation of the zeolite framework. Additionally, lower calcination temperatures lead to a slight increase in NP diameter, which may arise from the higher concentration of metal in the oxide phase during calcination, reshaping of the NPs by the exsolution process during framework collapse.

### *6.1.2 Characterisation of Carbon Deposits*

Figure 6.2 shows the performance of the Co/MOR catalyst calcinated at 800 °C and 550 °C, in terms of conversion, quality and morphology, with distinct differences visible between the CNM formed on the different catalysts. When calcined at 800 °C, the catalyst produced a carbon conversion of 15.1 percent with a D/G ratio of 0.65. Lowering the calcination temperature to 550 °C significantly increased the conversion to 19.9 percent, though the D/G ratio increased to 0.87, indicating a reduction in structural order. However, the increase in D/G ratio at 550 °C implies more structural defects in the carbon. The 2D/G ratios were similar at 0.30 and 0.28 for calcination temperatures of 800 °C and 550 °C, respectively, indicating a similar organized and few-layered graphitic structure.

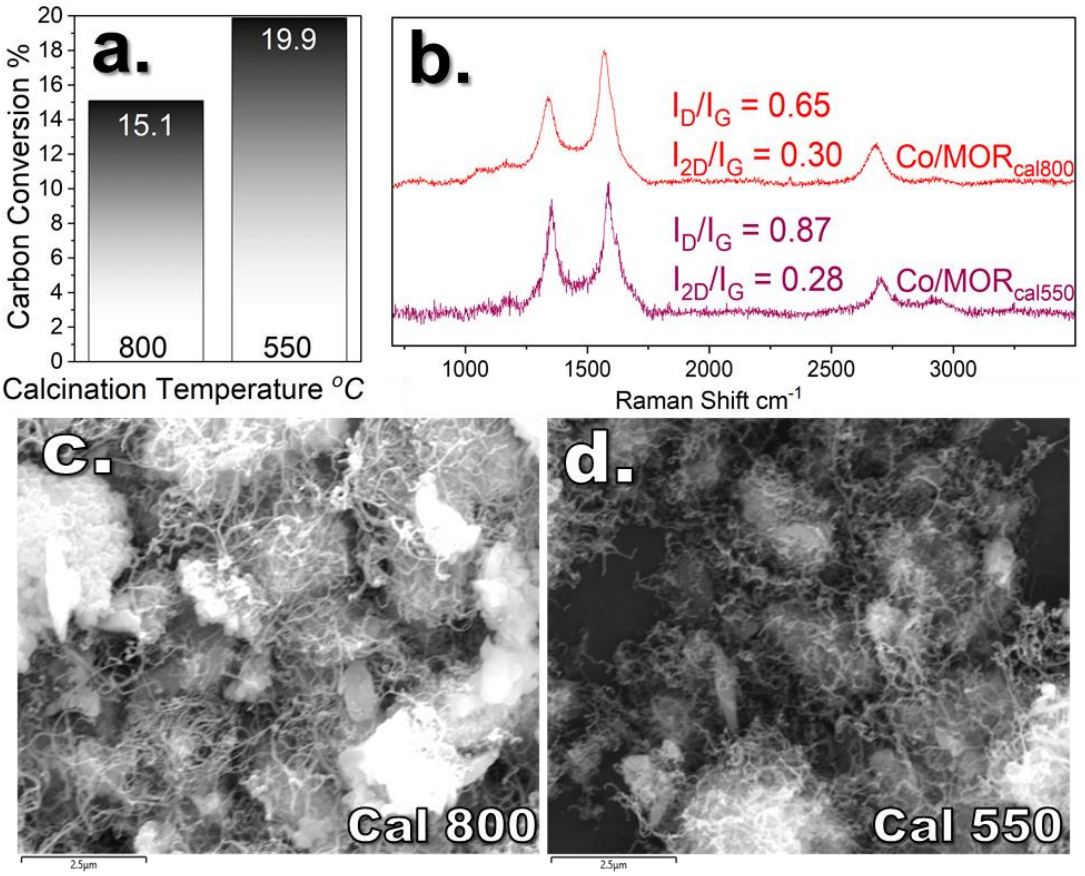


**Figure 6.2.** *Characterisation of the used catalyst prepared with different calcination temperatures with (a) showing the carbon conversion (b) Raman spectra (c) SEM image of Co/MOR$_{800}$, and (d) SEM image of Co/MOR$_{550}$.*

At 800 °C calcination temperature, the filaments appeared moderately dense and entangled, with estimated diameters in the range of 25-40 nm and lengths often exceeding several microns. Conversely, the lower temperature resulted in denser filamentous structures with a greater catalyst coverage. Although these were more chaotic networks of surface bound filaments, with a broader diameter range of 20 to 50 nm and with fewer long filaments straighter filaments extending away from the catalyst surface. This high filament density aligns well with the increased conversion found at the lower calcination temperature, with the lower graphitic quality and less order filamentous deposits also agreeing with each other.

This conversion enhancement is likely due to better preservation of the mordenite zeolite matrix at 550 °C. The lower thermal treatment helps maintain the high surface area and porosity of the support, which enhances hydrocarbon cracking and provides more active sites for carbon nucleation. However, this benefit comes at the cost framework stability during CNM growth. Since the catalyst has not been pre-annealed

at high temperatures, weaker MSI is likely, and therefore structural changes during carbon deposition are also more likely. These transformations can disturb NP geometry or surface interactions, introducing defects into the growing carbon structure and contributing to the higher D/G ratio. Conversely, the 800 °C calcined catalyst, though lower in conversion, exhibits more graphitic carbon. Its prior exposure to high temperature likely stabilises the NP-support interface, limiting further structural change during the high-temperature CNT growth process. This stability helps maintain particle symmetry and size distribution, reducing carbon defect formation and favouring improved ordering. Although, this will damage the zeolite structural integrity, and thus reduce the precursor cracking efficiency of the catalyst.

## 6.2 Preparation Method

### *6.2.1 Fresh and Used Catalyst Characterisation*

Figure 6.3 shows fresh and used characterisation of Co/MOR catalysts prepared by two alternative approaches, wet impregnation with ethylenediamine (EDA) named ($Co/MOR_{EDA}$) and hydrothermal metal incorporation (Co@MOR), each calcined at 550°C. In both cases, the large number of peaks below ~35° indicate that the MOR framework is maintained, further indicating calcination temperature is responsible for the framework collapse effect. The fresh $Co/MOR_{EDA}$ shows smaller NP diameters than the $Co/MOR_{550}$ catalyst, with NP diameters of 12.8 nm and 14.2 nm, respectively. This suggests that agglomeration of the oxide NPs is reduced by the inclusion of the chelating agent, with the metal complexes formed improving dispersion and stability of the metal ions during calcination [3] [4]. A similar degree of size increase is observed between the fresh and used catalyst NPs with and without the chelating agent, which will be degraded during calcination and thus no longer provides a function during CNM growth. The Co@MOR fresh catalyst does not show district peaks for the oxide phase, suggesting single metal ions bonded or incorporated into the framework rather than oxide NPs. The NP diameter of the used Co@MOR was the smallest of the tested catalyst at 11.4 nm, indicating that the direct formation from dispersed ions can form smaller metal NPs than reduction of pre-existing oxide NPs. This is due to the entrapment of NPs within the zeolite framework, limiting the size of NPs [5] [6] [7] [8].

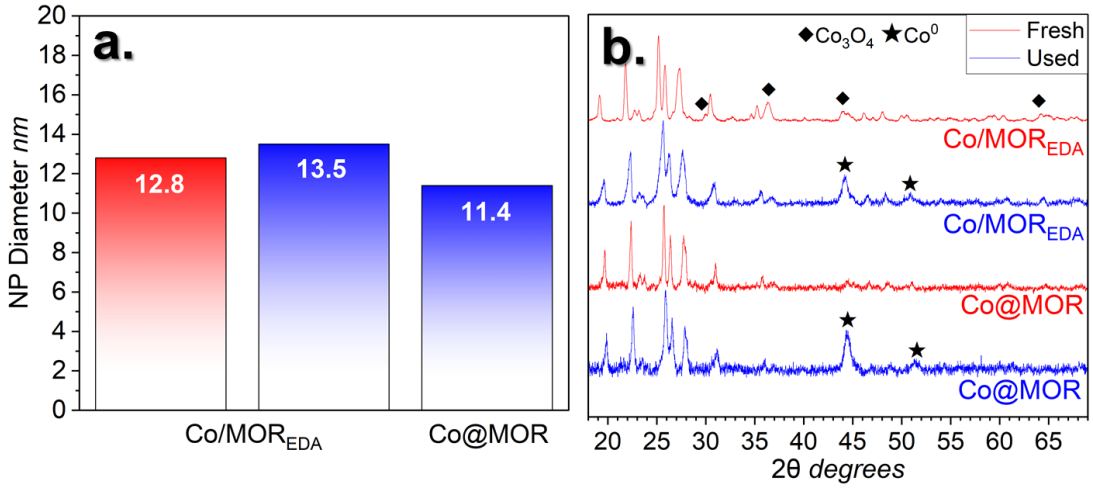


**Figure 6.3.** *Fresh and used catalyst characterisation using different preparation methods, (a) showing the NP diameters and (b) showing the XRD patterns, with fresh catalysts shown in red and used catalysts shown in blue.*

### 6.2.2 Characterisation of Carbon Deposits

Figure 6.4 shows the performance of the catalysts synthesised by the different preparation methods.

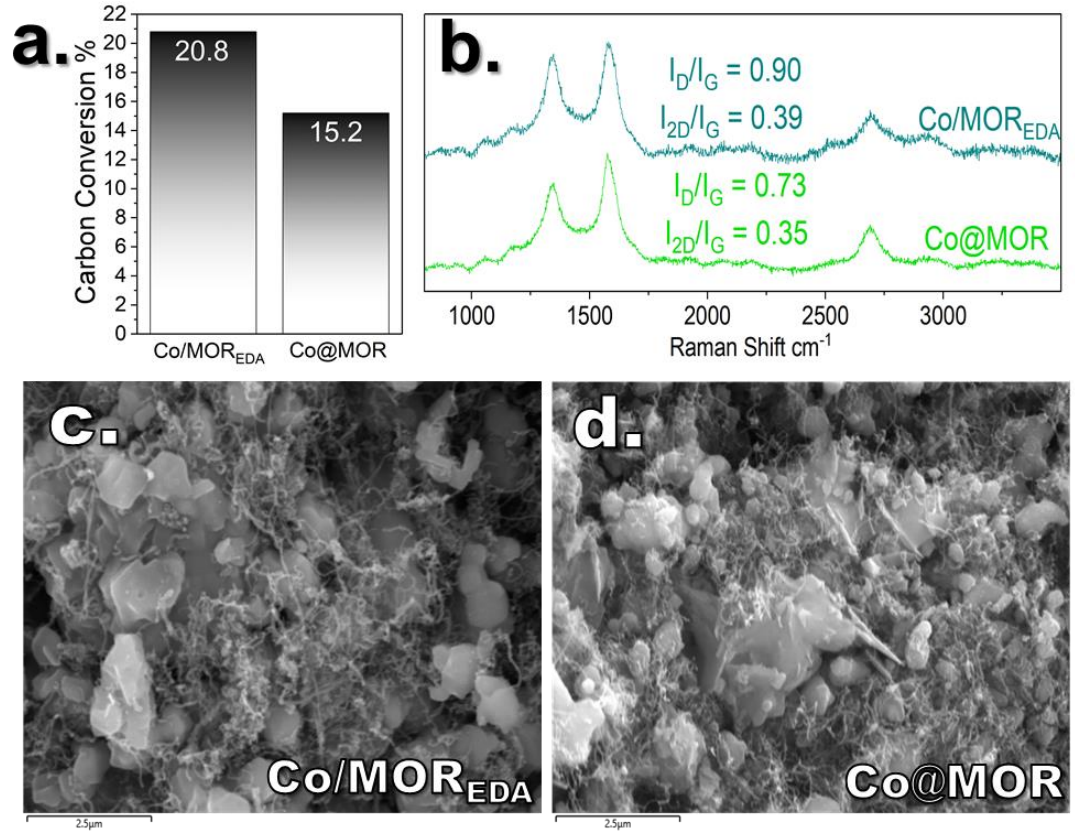


**Figure 6.4.** *Characterisation of the used catalyst prepared with different preparation methods, with (a) showing the carbon conversion (b) Raman spectra (c) SEM image of Co/MOR$_{EDA}$, and d) SEM image of Co@MOR.*

It can be seen that Co/$MOR_{EDA}$ achieved a carbon conversion at 20.8 percent, a slight increase over Co/$MOR_{550}$. The enhanced conversion observed for Co/$MOR_{EDA}$ is attributed to the role of ethylenediamine, which likely improves cobalt dispersion and enhances MSI during impregnation. The SEM image for Co/$MOR_{EDA}$ shows a dense network of entangled carbon filaments with some spherical carbon agglomerates. The filaments are short to moderate lengths of around 1 to 2 micrometres and a diameter range of approximately 20 to 60 nanometres. This dense morphology is consistent with abundant nucleation sites and a high surface coverage. The Raman analysis supports this, showing an $I_D/I_G$ ratio of 0.90 indicating a relatively high level of structural disorder. Overall, the addition of EDA shows desirable smaller NP diameters, the performance effect difference compared to Co/$MOR_{550}$ without the addition of EDA chelating agent is limited.

In contrast, the Co@MOR sample displayed a lower conversion of only 15.2%, but improved structural quality with a lower $I_D/I_G$ ratio of 0.73, reflecting enhanced graphitic quality. The SEM images for Co@MOR shows more open, less densely packed CNTs with longer lengths exceeding several micrometres and with a narrower diameter distribution between 15 and 30 nm. These filaments are more linear and uniformly distributed, indicating better nanoparticle dispersion and more controlled carbon growth. The lower conversion in Co@MOR may result from a reduced number of catalytically active surface sites. During hydrothermal synthesis, cobalt may become too deeply encapsulated within the zeolite framework to effectively participate in surface reactions. In addition, the extensive washing required post-synthesis may remove loosely bound cobalt ions, further reducing the accessible metal content. These effects likely contribute to the lower carbon conversion observed. Despite these limitations, the higher carbon quality produced by Co@MOR demonstrates the potential of hydrothermal synthesis to enhance CNT structural order. With methodological improvements aimed at increasing metal accessibility and refining zeolite crystallinity, the hydrothermal approach could provide a highly effective route for producing high-quality CNMs.

## 6.3 Additional Metal Species

### *6.3.1 Fresh and Used Catalyst Characterisation*

Figure 6.5 shows the characterisation of fresh and used Co/MOR catalysts each with the addition of a secondary modifier metal species, namely Mo and Mn. CoMo/MOR had large metal NPs with average diameter of 18.5 nm, whereas CoMn/MOR

displayed average NP diameters similar to that of the traditional Co/MOR catalysts. The peaks observed in the fresh catalyst are potentially due to mixed metal oxides, as well as Co oxides. Additionally, some peak that are associated with oxide phases can still be seen in the used catalysts, likely indicating Mo or Mn oxide phases. The larger NP sizes observed for CoMo/MOR, can be due to the formation mixed metal oxide NPs, with high overall metal loading and stability of these responsible for large CoMo oxide NPs. Although, CoMo/MOR showed the greatest reduction in NP diameter, with CoMo/MOR metal NPs displaying an average diameter of 15.1 nm. This indicates the resistance to sintering which the inclusion of Mo can provide during the CNM growth process [9].

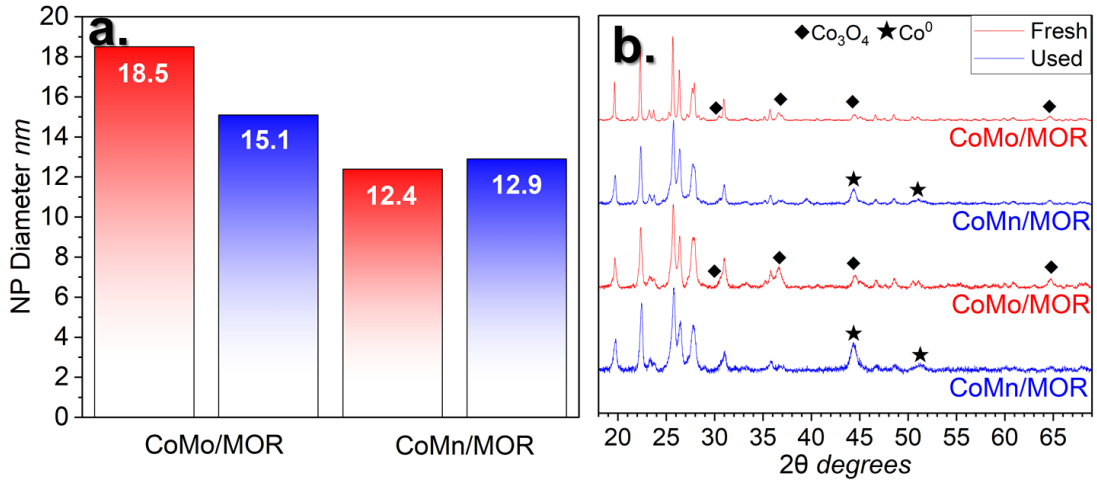


**Figure 6.5.** *Fresh and used catalyst characterisation of CoMo/MOR and CoMn/MOR, (a) showing the NP diameters and (b) showing the XRD patterns, with fresh catalysts shown in red and used catalysts shown in blue.*

### *6.3.2 Characterisation of Carbon Deposits*

The conversion, quality and morphology of the carbon grown by the CoMo/MOR and CoMn/MOR catalysts are shown in Figure 6.6.

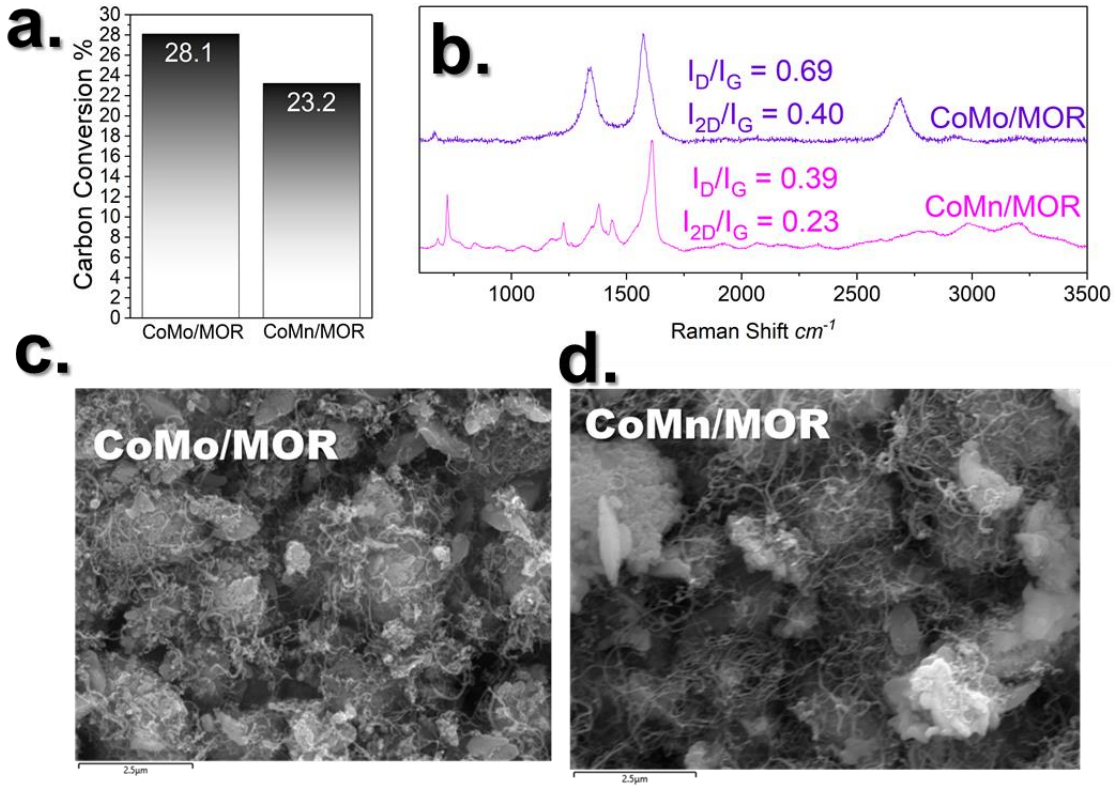


**Figure 6.6.** *Characterisation of the used catalyst prepared with different additional supporting metals with (a) showing the carbon conversion (b) Raman spectra (c) SEM image of CoMo/MOR, and (d) SEM image of CoMn/MOR.*

CoMo/MOR achieved the highest carbon conversion of 28.1 % among any of the tested catalysts. This performance enhancement is attributed to the promoting effect of Mo, which enhances hydrocarbon cracking and thermal stability of the Co NPs. Raman analysis showed a moderate $I_D/I_G$ ratio of 0.69, suggesting a balance between carbon conversion and graphitic structure. The SEM image reveals a dense mat of entangled CNTs with lengths predominantly ranging with diameters between 30 and 60 nm.

CoMn/MOR exhibited a lower carbon conversion of 23.2%, although still higher than traditional Co/MOR catalysts, and additionally displayed the highest graphic quality of the catalysts tested. The $I_D/I_G$ ratio was found to be 0.4, indicating a very high-quality graphic lattice is present. The sharp peak at around 700 $cm^{-1}$ can be attributed to Mn oxide phases. Several additional peaks in the range of approximately 1200 $cm^{-1}$ and 1500 $cm^{-1}$ can be observed, with the G-band shifted to around 1610 $cm^{-1}$. This can be attributed to carbon-oxygen bonding, indicating the formation of oxygen functional groups within or attached to the CNM. This indicates that Mn oxides interaction with the growing CNM can promote the inclusion of these oxygen functional groups. These

functional groups can modify the performance of the CNMs grown, offering new application and a higher value product.

The SEM image of the used CoMn/MOR catalyst shows a less tangled, more open CNT network. These filaments are generally thinner, with diameters between 15 and 40 nm, and longer, frequently exceeding several microns. he increased length and reduced entanglement indicate improved catalyst control over filament growth and fewer structural defects. This implies that Mn acts to stabilise the active sites in a way that favours ordered graphitic structures.

Overall, these results highlight the contrasting benefits of Mo and Mn as promoters. Mo is optimal for enhancing carbon conversion through improved catalytic activity, while Mn favours the formation of high-quality, structurally ordered CNTs. This suggests that catalyst selection should be guided by the desired trade-off between conversion and material quality depending on the application.

### *6.3.3 Conclusion*

The performance of Co-based MOR catalysts in CNT synthesis is significantly influenced by calcination conditions, synthesis methods, and the incorporation of secondary metal promoters. Each of these factors governs the balance between carbon conversion and structural quality of the produced CNTs.

Lower calcination temperatures preserve the zeolite framework and enhance catalytic activity, leading to higher carbon conversions. However, this comes with a trade-off, as the resulting CNTs exhibit less structural order. In contrast, higher calcination temperatures promote better graphitisation due to enhanced catalyst stability, though at the expense of overall carbon conversion.

Synthesis approach also affects catalyst performance. Wet impregnation with organic additives like EDA improves conversion by strengthening metal–support interaction. Meanwhile, hydrothermal synthesis enhances CNT quality through better nanoparticle dispersion and size control. Nevertheless, this method may limit active metal availability due to encapsulation and post-synthesis washing steps, potentially reducing catalytic efficiency.

Introducing secondary metals into the Co/MOR system provides the most effective method to improving catalytic performance. Although both metals enhance conversion and quality, the inclusion of Mo is best for improving carbon conversion, while Mn promotes the formation of higher-quality, more graphitic CNMs.

The importance of tuning catalyst preparation parameters to meet specific performance goals is highlighted. Strategies that favour high-quality CNTs may compromise conversion and vice versa. However, through appropriate combinations of synthesis route, calcination, and metal promotion, a tailored balance can be achieved for targeted applications in carbon nanomaterial synthesis.

# References


[1] Z. Zhu, Q. Chen, and W. Chen, “12-P-05 - Study of relationship between mordenite acidity and structure with calcination temperature,” 2001. doi: 10.1016/s0167-2991(01)81436-1.

[2] D. M. El-Mekkawi and M. M. Selim, “Effect of metal loading processes on the stability and thermal transformation of Co 2 +- and Cu 2 +-zeolite y prepared from Egyptian kaolin,” *Mater. Charact.*, vol. 69, 2012, doi: 10.1016/j.matchar.2012.04.001.

[3] M. O. Kazakov *et al.*, “Comparative study of MWCNT and alumina supported CoMo hydrotreating catalysts prepared with citric acid as chelating agent,” *Catal. Today*, vol. 357, 2020, doi: 10.1016/j.cattod.2019.03.051.

[4] F. M. M. R. A. R. Shahla Karimi, “Development of a novel method to synthesize Ni/SiO2.MgO catalysts using EDTA as a chelating agent for the methane decomposition proces,” *Powder Technol.*, vol. 443, Jul. 2024.

[5] C. S. Cundy and P. A. Cox, “The hydrothermal synthesis of zeolites: Precursors, intermediates and reaction mechanism,” 2005. doi: 10.1016/j.micromeso.2005.02.016.

[6] M. Shamzhy, M. Opanasenko, P. Concepción, and A. Martínez, “New trends in tailoring active sites in zeolite-based catalysts,” 2019. doi: 10.1039/c8cs00887f.

[7] Y. L. H. S. L. Z. Y. W. Y. H. L. M. J. H. A. T. N. M. D. J. Z. L. Z. W. & F. P.-G. Junyan Zhang, “Tuning metal-support interactions in nickel–zeolite catalysts leads to enhanced stability during dry reforming of methane,” *Nat. Commun.*, Oct. 2024.

[8] B. C. Gates, A. Katz, and J. Liu, “Nested Metal Catalysts: Metal Atoms and Clusters Stabilized by Confinement with Accessibility on Supports,” 2023. doi: 10.1021/prechem.2c00011.

[9] A. M. Haggar, A. E. Awadallah, A. A. Aboul-Enein, and G. H. Sayed, “Non-oxidative conversion of real low density polyethylene waste into hydrogen and carbon nanomaterials over MgO supported bimetallic Co-Mo catalysts with different total Co-Mo contents,” *Chem. Eng. Sci.*, vol. 247, 2022, doi: 10.1016/j.ces.2021.117092.

# Chapter 7

## Conclusions and Future Work

## 7.1 Conclusions

In this thesis the synthesis of carbon nanomaterials (CNMs) using transition metal-based catalysts has been investigated, revealing the complex interplay between metal species, support materials, and catalyst preparation strategies. These factors influence key catalytic features including metal-support interaction strength, nanoparticle stability, dispersion and size, which in turn govern the overall catalytic performance.

Comparison of the metal species showed distinct differences in performance. Cobalt-based systems demonstrated superior nanoparticle dispersion and structural stability, leading to high conversions and the formation of primarily spherical carbon nano-onions (CNOs) alongside some carbon nanotubes (CNTs). Nickel-based catalysts gave intermediate conversions but favoured the formation of filamentous carbon, producing the highest proportion of CNTs. Iron-based catalysts were limited by sintering, phase instability, and early formation of catalytically inactive carbide species. These deactivated phases hindered performance and suppressed the expected synergistic effects in bimetallic systems, with Fe-based monometallics producing the lowest overall conversion.

The influence of the support material was found to be influenced by the intrinsic support properties and the specific metal-support pairing. KAO showed strong interactions with both metal and carbon, producing well-dispersed small spherical nanoparticles, but this strong binding inhibited CNT nucleation and limited growth beyond surface-bound structures. MOR was most effective with cobalt, where its one-dimensional pore channels restricted diffusion but promoted the formation of surface-based nanoparticles following framework collapse. This environment facilitated high-quality CNTs with dense filament networks. FAU showed the highest compatibility with nickel, maintaining structural integrity and enabling extensive filamentous growth. In contrast, cobalt-based systems often caused FAU framework collapse. This divergence was attributed to nickel's ability to stabilise the zeolite framework. The open three-dimensional network and strong hydrocarbon cracking capacity of FAU supported well-dispersed nanoparticles and carbon precursor diffusion, allowing high conversion and quality of the Ni-FAU and FeNi-FAU catalysts, respectively. Overall, Co/MOR was determined to give a desirable balance between conversion and quality, and also display desirable underlying properties of good metal dispersion, and therefore was selected for further testing.

Calcination temperature, synthesis approach and secondary metal addition played a significant role in determining the structure and performance of the Co/MOR catalyst. Lower calcination temperatures preserved zeolite integrity and promoted conversion, while higher temperatures improved structural quality through better graphitisation. Wet impregnation with organic additives enhanced conversion via strengthened metal-support interactions, whereas hydrothermal synthesis offered superior nanoparticle control but risked reduced metal accessibility. Additional secondary metals Mo and Mn both displayed increases in conversion and quality over monometallic Co, with Mo favouring high conversions and Mn high quality, with signs that oxygen functional group incorporation had also occurred.

Overall, zeolite supported catalysts display great promise for the conversion of plastics in to high value CNMs. In a one stage system, the high carbon solubility of iron-based catalysts leads to reduced performance, whereas Co- and Ni-based catalysts are more resilient. The selection of metal can influence whether the zeolite framework is preserved or collapse during growth, which can both be beneficial or detrimental depending on how the specific zeolite pore morphology influences to precursor decomposition and CNM growth reactions.

## 7.2 Future Work

Due to time limitations, many of the results in this thesis were only repeated one time, although the variability between runs were estimated with three repetitions for some selected samples. These constraints were largely attributable to COVID-related restrictions during the first two years of the PhD. Laboratory access was unavailable during the first year and significantly limited in the second, with equipment time prioritised for later-stage doctoral researchers thereby reducing experimental throughput even after the lab reopening. In future work, runs for each if the catalysts would be carried out at least three times.

Ni-based FAU catalysts, particularly Ni/FAU and FeNi/FAU, showed strong baseline performance and are promising candidates for further improvement. The development strategies used for Co/MOR in this work should be applied to these systems. This includes adjusting calcination temperature, modifying synthesis conditions, and exploring secondary metal additions to improve both conversion and structural quality.

For Co/MOR catalysts, refining the hydrothermal synthesis route remains important for achieving full catalytic performance. Although hydrothermal methods offer good

control over nanoparticle size and distribution, they often suffer from reduced activity due to poor surface accessibility of metal sites. This issue could be addressed by using higher calcination temperatures to induce framework collapse during growth. This will allow for NPs formed within the zeolite frame to be exsolved and thus become active growth sites. This allows for the well-dispersed metal in the M@zeolite structure to translated into enhanced catalyst performance. Therefore, potentially retaining the benefits of hydrothermal synthesis while overcoming its limitations.

Separately, the addition of secondary metal promoters such as Mo and Mn has demonstrated distinct advantages. Molybdenum enhances catalytic activity and conversion by improving hydrocarbon cracking and stabilising the active metal phase. In contrast, manganese favours structural quality by promoting more ordered, graphitic carbon growth. The choice and ratio of promoter can thus be used to fine-tune the balance between productivity and material performance. Future work should explore varying metal ratios and total metal loadings to better understand how these parameters affect nanoparticle behaviour, catalyst stability, and CNT morphology.

Combining hydrothermal synthesis with Mo or Mn promotion presents a promising strategy for achieving both high conversion and high carbon quality. While hydrothermal processing improves nanoparticle control and graphitisation, Mo and Mn can address its current limitations by either boosting catalytic activity or enhancing structural order. Future studies should examine how these promoters interact with the hydrothermally incorporated cobalt, and whether synthesis conditions can be adjusted to maximise their synergistic effects. This combined approach may lead to the development of Co-based zeolite catalysts that deliver both efficient precursor conversion and structurally refined carbon nanomaterials. The highest performing one-stage materials and growth strategies can be applied to two-stage systems, which are likely to further increase overall performance. Building on the insights gained from one-stage catalyst testing, two-stage systems offer a broader and more flexible platform for catalyst design. They will allow for the inclusion of iron or iron-based bimetallic catalysts, which provide high carbon solubility and are less toxic and more cost-effective than cobalt or nickel.

Finally, the recyclability of the catalyst should be evaluated. Complexing agents can be used to extract metals, and our work using a Co-EDA metal source has shown their effectiveness as reagents. The support material can also be recycled. Zeolites can be degraded using alkaline solutions, which have the potential to cause less

damage to CNMs than traditionally used acids. Furthermore, the resulting material could serve as a precursor for further hydrothermal synthesis. A combined solvent wash that removes metal using EDA or similar complexing agents, while also dissolving the zeolite framework, would produce a solution similar in composition to that used in the original hydrothermal synthesis of the Co@MOR catalyst. This indicates the potential for both the metal and support to be recovered and reused, supporting the overall recyclability of the system.

Overall, the production of high value CNMs using the zeolite-supported transition metal catalysts tested in this thesis provide a highly promising technology for the valorisation of waste polyolefin plastics.